

INNOVATIVE USE OF GLOBAL NAVIGATION
SATELLITE SYSTEMS FOR FLIGHT INSPECTION

A DISSERTATION

SUBMITTED TO THE DEPARTMENT OF AERONAUTICS AND

ASTRONAUTICS

AND THE COMMITTEE ON GRADUATE STUDIES

OF STANFORD UNIVERSITY

IN PARTIAL FULFILLMENT OF THE REQUIREMENTS

FOR THE DEGREE OF

DOCTOR OF PHILSOPHY

Euiho Kim

December 2007

UMI Number: 3292381

INFORMATION TO USERS

The quality of this reproduction is dependent upon the quality of the copy submitted. Broken or indistinct print, colored or poor quality illustrations and photographs, print bleed-through, substandard margins, and improper alignment can adversely affect reproduction.

In the unlikely event that the author did not send a complete manuscript and there are missing pages, these will be noted. Also, if unauthorized copyright material had to be removed, a note will indicate the deletion.

UMI[®]

UMI Microform 3292381

Copyright 2008 by ProQuest Information and Learning Company.

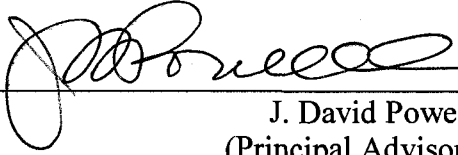
All rights reserved. This microform edition is protected against unauthorized copying under Title 17, United States Code.

ProQuest Information and Learning Company
300 North Zeeb Road
P.O. Box 1346
Ann Arbor, MI 48106-1346

© Copyright 2008 Euiho Kim

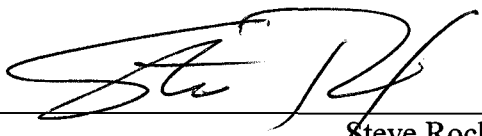
All Rights Reserved

I certify that I have read this dissertation and that in my opinion it is fully adequate, in scope and quality, as dissertation for the degree of Doctor of Philosophy.



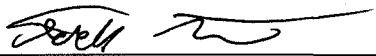
J. David Powell
(Principal Advisor)

I certify that I have read this dissertation and that in my opinion it is fully adequate, in scope and quality, as dissertation for the degree of Doctor of Philosophy.



Steve Rock

I certify that I have read this dissertation and that in my opinion it is fully adequate, in scope and quality, as dissertation for the degree of Doctor of Philosophy.



Todd Walter

Approved for the University Committee on Graduate Studies:

Abstract

The International Civil Aviation Organization (ICAO) mandates flight inspection in every country to provide safety during flight operations. Among many criteria of flight inspection, airborne inspection of Instrument Landing Systems (ILS) is very important because the ILS is the primary landing guidance system worldwide. During flight inspection of the ILS, accuracy in ILS landing guidance is checked by using a Flight Inspection System (FIS). Therefore, a flight inspection system must have high accuracy in its positioning capability to detect any deviation so that accurate guidance of the ILS can be maintained. Currently, there are two Automated Flight Inspection Systems (AFIS). One is called Inertial-based AFIS, and the other one is called Differential GPS-based (DGPS-based) AFIS. The Inertial-based AFIS enables efficient flight inspection procedures, but its drawback is high cost because it requires a navigation-grade Inertial Navigation System (INS). On the other hand, the DGPS-based AFIS has relatively low cost, but flight inspection procedures require landing and setting up a reference receiver. Most countries use either one of the systems based on their own preferences.

There are around 1200 ILS in the U.S., and each ILS must be inspected every 6 to 9 months. Therefore, it is important to manage the airborne inspection of the ILS in a very efficient manner. For this reason, the Federal Aviation Administration (FAA)

mainly uses the Inertial-based AFIS, which has better efficiency than the DGPS-based AFIS in spite of its high cost. Obviously, the FAA spends tremendous resources on flight inspection.

This thesis investigates the value of GPS and the FAA's augmentation to GPS for civil aviation called the Wide Area Augmentation System (or WAAS) for flight inspection. Because standard GPS or WAAS position outputs cannot meet the required accuracy for flight inspection, in this thesis, various algorithms are developed to improve the positioning ability of Flight Inspection Systems (FIS) by using GPS and WAAS in novel manners. The algorithms include Adaptive Carrier Smoothing (ACS), optimizing WAAS accuracy and stability, and reference point-based precise relative positioning for real-time and near-real-time applications. The developed systems are WAAS-aided FIS, WAAS-based FIS, and stand-alone GPS-based FIS. These systems offer both high efficiency and low cost, and they have different advantages over one another in terms of accuracy, integrity, and worldwide availability. The performance of each system is tested with experimental flight test data and shown to have accuracy that is sufficient for flight inspection and superior to the current Inertial-based AFIS.

Acknowledgments

First, I'd like to thank God for leading me to come this far. I would like to thank my advisor, Professor J. David Powell for giving me the opportunity to pursue this research. I really appreciate his guidance, support and, more importantly, encouragement. I have also enjoyed every minute of our meetings and trips to Oklahoma City, Toulouse, and Geneva. I will always remember and will be grateful for this great experience at Stanford.

I would also like to thank Dr. Todd Walter for guiding me through the research. His complete knowledge in GPS and WAAS always gave me the right direction to go. I would like to thank Dr. Uri Peled for his great work and help at the beginning of this research. Without him, I would have suffered a lot in analyzing the flight test data. I would like to express my gratitude to the defense and reading committee members including Professor Per Enge, Professor Stephen Rock, and Professor Paul Segall for their valuable comments and criticism.

I would like to thank the Federal Aviation Administration Flight Inspection department (AVN) for their support in this research. I especially thank flight inspection crews who arranged and participated in gathering flight test data. I gratefully acknowledge the Department of Aeronautics and Astronautics and our office staff, Sherann Ellsworth, Dana Parga, and Douglas A. Archdeacon for their help.

I would like to thank all our group members in the GPS laboratory. I will always remember and will be grateful for their kindness. I would like to thank many Korean friends in my department and my church. Without them, there would have been no fun in my life at Stanford.

Lastly, I would like to thank my parents for supporting me for the many years in the U.S. I also appreciate their belief in me. I dedicate this thesis to them. I would like to thank my wife, Heesun, for her sacrifice and encouragement for me. She has been going through every moment with me from the qualifying exam to the defense at Stanford. She also deserves this thesis. I would like to thank my two sons, David and Timothy, for always providing me energy and big laughs.

Table of Contents

ABSTRACT	IV
ACKNOWLEDGMENTS.....	VI
TABLE OF CONTENTS	VIII
LIST OF FIGURES.....	XI
LIST OF TABLES.....	XVI
CHAPTER 1 INTRODUCTION TO GNSS AND FLIGHT INSPECTION.....	1
1.1 INTRODUCTION	1
1.2 OVERVIEW OF GLOBAL NAVIGATION SATELLITE SYSTEMS (GNSS)	2
1.3 INSTRUMENT LANDING SYSTEM AND FLIGHT INSPECTION.....	10
1.4 MOTIVATION.....	17
1.5 THESIS SYNOPSIS AND CONTRIBUTIONS.....	17
<i>PART I ALGORITHM DEVELOPMENTS TO IMPROVING POSITION STABILITY.....</i>	22
CHAPTER 2 ADAPTIVE CARRIER SMOOTHING USING CODE AND CARRIER DIVERGENCE FOR A SINGLE FREQUENCY RECEIVER.....	23
2.1 INTRODUCTION	23
2.2 REVIEW OF LINEAR REGRESSION	25
2.3 ESTIMATION OF THE SLANT IONOSPHERIC DELAY GRADIENT AND MULTIPATH CHARACTERISTICS USING CODE MINUS CARRIER PHASE MEASUREMENTS.....	27
2.4 ADAPTIVE CARRIER SMOOTHING (ACS).....	36

2.5 RESULTS	49
2.6 DISCUSSION	54
2.7 CONCLUSION.....	55
CHAPTER 3 OPTIMIZING WAAS ACCURACY/STABILITY FOR A SINGLE FREQUENCY RECEIVER.....	57
3.1 INTRODUCTION	57
3.2 MODIFICATION OF WAAS WEIGHTING MATRIX.....	59
3.3 NULLIFYING RANGE RATE CORRECTION	65
3.4 RESULTS	66
3.5 CONCLUSION.....	71
CHAPTER 4 REFERENCE POINT-BASED RELATIVE POSITIONING METHODS WITH A SINGLE FREQUENCY RECEIVER.....	72
4.1 INTRODUCTION	72
4.2 IONO-FREE PRECISE RELATIVE POSITIONING (I-F PRP).....	74
4.3 TIME-DIFFERENCED PRECISE RELATIVE POSITIONING (T-D PRP).....	83
4.4 CONCLUSION.....	88
<i>PART II FLIGHT INSPECTION SYSTEM DESIGNS AND PERFORMANCE</i>	90
CHAPTER 5 WAAS-AIDED FLIGHT INSPECTION SYSTEM.....	91
5.1 INTRODUCTION	91
5.2 WAAS AIRBORNE ERROR CHARACTERISTICS	92
5.3 WAAS-AIDED FIS SYSTEM ARCHITECTURE.....	95
5.4 FLIGHT TEST RESULTS.....	107
5.5 CONCLUSION.....	116
CHAPTER 6 WAAS-BASED FLIGHT INSPECTION SYSTEM.....	117
6.1 INTRODUCTION	117
6.2 WAAS-BASED FIS SYSTEM ARCHITECTURE	118
6.3 FLIGHT TEST RESULTS.....	124
6.4 CONCLUSION.....	127
CHAPTER 7 STAND-ALONE GPS-BASED FLIGHT INSPECTION SYSTEM.....	129
7.1 INTRODUCTION	129
7.2 STAND-ALONE GPS-BASED FIS SYSTEM ARCHITECTURE.....	130
7.3 RESULTS	137
7.4 CONCLUSION.....	140

CHAPTER 8 CONCLUSIONS 141

8.1 SUMMARY OF THESIS 141

8.2 FLIGHT INSPECTION SYSTEMS WITH FUTURE SIGNALS..... 145

BIBLIOGRAPHY..... 147

List of Figures

Figure 1.1: A baseline constellation of 24 GPS satellites (Courtesy of FAA).....	4
Figure 1.2: Worldwide location of GPS Control Segment elements (Courtesy of FAA)...	4
Figure 1.3: Various GPS measurement errors sources	6
Figure 1.4: Conceptual illustration of Wide Area Augmentation System (Courtesy of FAA).....	8
Figure 1.5: Frequency allocation of the current and new GPS signals (Courtesy of Aerospace Corp.).....	10
Figure 1.6: An airplane approaches a runway using ILS guidance	11
Figure 1.7: Localizer and glideslope radiation patterns and their guidance.....	12
Figure 1.8: Vertical flight inspection system accuracy requirements for ILS calibration.	14
Figure 1.9: The two surveyors on the ground measure the aircraft's deviation.....	16
Figure 1.10: Modern computerized FIS (courtesy of NXT, Inc) [NXTFIS].....	17
Figure 2.1: Tradeoff in using a Hatch filter.....	24
Figure 2.2: Unbiased code minus carrier over 600 seconds with a regressed line for airborne measurements.....	30
Figure 2.3: Power spectral density of airborne multipath in code minus carrier phase measurements	30

Figure 2.4: Unbiased code minus carrier over 600 seconds with a regressed line for static ground measurements	31
Figure 2.5: Power spectral density of static ground noise in code minus carrier measurements	32
Figure 2.6: Histogram of the difference of the estimated ionospheric delay rates from using OLS and FGLS	33
Figure 2.7: Comparison of the estimated ionospheric delay gradients from a dual frequency receiver and from using the linear model during a nominal ionospheric day ..	35
Figure 2.8: Histogram of the difference between smoothed $\Delta I_{t,dual}$ and $\hat{\beta}_{t,1}$ for all satellites in view during 19 hours on Oct 26, 2006 at Atlantic City	36
Figure 2.9: Optimal k 's with white noise multipath assumption with respect to the standard deviations of multipath and ionospheric delay gradients.....	40
Figure 2.10: Induced bias from using optimal k 's from Figure 2.9 with respect to standard deviations of multipath and ionospheric delay gradients.....	40
Figure 2.11: Variance of filtered multipath from using optimal k from Figure 2.9 with respect to standard deviations of multipath and ionospheric delay gradients	41
Figure 2.12: True multipath and a modeled sine wave from static ground measurements	43
Figure 2.13: Filtered multipath of true and modeled multipath from a Hatch filter	45
Figure 2.14: Optimal k with sinusoidal multipath with respect to the amplitudes of a cosine wave and the ionospheric delay gradients.....	46
Figure 2.15: Induced biases from using the optimal k from Figure 2.13 with respect to the amplitudes of a cosine wave and the ionospheric delay gradients	47
Figure 2.16: Amplitudes of a filtered cosine wave from using the optimal k from Figure 2.13 with respect to the amplitudes of a cosine wave and the ionospheric delay gradients	47
Figure 2.17: Adaptive carrier smoothing (ACS) procedures.....	48
Figure 2.18: $\hat{\sigma}_{multipath}$ and \hat{a} from airborne measurements for one satellite.....	49
Figure 2.19: Optimal k for airborne measurements corresponding to the estimated parameters in Figure 2.18.....	50

Figure 2.20: Position errors from using the 100 s Hatch filter and the ACS with white noise multipath assumption on airborne measurements.....	51
Figure 2.21: Elevation angles in degrees of the satellites in the test for airborne measurements	51
Figure 2.22: \hat{A} , $\hat{\omega}$, and \hat{a} for one satellite from ground measurements.....	52
Figure 2.23: Optimal k corresponding to the estimated parameters in Figure 2.22.....	53
Figure 2.24: The position errors from using a 100 s hatch filter and the ACS with a sinusoidal multipath assumption on static ground measurements.....	54
Figure 3.1: Fast clock correction with and without the RRC.....	66
Figure 3.2: Comparison of the position errors in East from the standard WAAS and the WAAS with a new weighting matrix	68
Figure 3.3: Comparison of the position errors in Up from the standard WAAS and the WAAS with a new weighting matrix	68
Figure 3.4: Total variances of the observed satellites in the above tests from the standard WAAS.....	69
Figure 3.5: Total variances of the observed satellites in the above tests from the optimized WAAS	69
Figure 3.6: Comparison of the horizontal errors from the standard WAAS and the optimized WAAS	70
Figure 3.7: Comparison of the vertical errors from the standard WAAS and the optimized WAAS	71
Figure 4.1: Geometry of a receiver and a reference point with a short baseline.....	76
Figure 4.2: Horizontal Error in 11 data sets for 1 hour of operation.....	80
Figure 4.3: Vertical Error in 11 data sets for one hour of operation	81
Figure 4.4: The number of satellites in 11 data sets for one hour of operation.....	82
Figure 4.5: RMS of I-F PRP in 11 data sets for one hour of operation.....	82
Figure 4.6: RMS of stand-alone GPS in 11 data sets for one hour of operation.....	83
Figure 4.7: T-D PRP errors in East with and without the differential ionospheric corrections	86

Figure 4.8: T-D PRP errors in North with and without the differential ionospheric corrections	87
Figure 4.9: T-D PRP errors in Up with and without the differential ionospheric corrections	87
Figure 4.10: RMS comparison of the T-D PRP with and without the differential ionospheric delay correction at 900 seconds	88
Figure 5.1: Example of WAAS airborne position errors	93
Figure 5.2: Power spectral density of WAAS airborne noise shown in Figure 5.1	94
Figure 5.3: Example of WAAS fast clock correction.....	94
Figure 5.4: WAAS-aided FIS system architecture	96
Figure 5.5: Impulse response of the designed low pass filter.....	99
Figure 5.6: High pass filtering block for cyclic noise	102
Figure 5.7: Impulse response of the designed high pass filter	102
Figure 5.8: Frequency response of the designed high pass filter	103
Figure 5.9: Comparison of WAAS noise and estimated WAAS noise	104
Figure 5.10: The residual errors of the estimated WAAS noise.....	104
Figure 5.11: Examples of flight path during flight tests at Oklahoma City	108
Figure 5.12: WAAS-aided FIS vertical position error without radar altimeter error	109
Figure 5.13: WAAS-aided FIS cross-track position error without TVPS error	109
Figure 5.14: Simulated horizontal error for a tactical grade INS	111
Figure 5.15: Simulated horizontal error for an automotive grade INS.....	111
Figure 5.16: WAAS-aided FIS vertical position error without a radar altimeter error using a simulated tactical grade INS	112
Figure 5.17: WAAS-aided FIS cross-track position error without a TVPS error using a simulated tactical grade INS.....	113
Figure 5.18: WAAS-aided FIS vertical position error using a simulated automotive grade INS without radar altimeter error	114
Figure 5.19: WAAS-aided FIS cross-track position error using a simulated automotive grade INS without TVPS error	114
Figure 6.1: WAAS-Based FIS system architecture.....	118

Figure 6.2: Chart of items for satellite exclusion criteria.....	120
Figure 6.3: Example of fast-clock correction filtering using a non-causal filter.....	121
Figure 6.4: Schematics of the characteristics of three position measurements (R.A., WAAS, TD-PRP) with true position.....	122
Figure 6.5: WAAS-based FIS cross-track position errors without a TVPS error	125
Figure 6.6: WAAS-based FIS vertical position errors without a radar altimeter error ...	125
Figure 7.1: Stand-alone GPS-based FIS system architecture.....	131
Figure 7.2: Positioning failures of the T-D PRP with simulated a 4 cm/s ramp satellite clock error during approach.....	132
Figure 7.3: Positioning failures due to 1 meter amplitude sinusoidal clock dithering during approach.....	133
Figure 7.4: Observed maximum separated solutions in vertical during approaches without satellite failures	134
Figure 7.5: Observed maximum separated solutions in vertical during approaches with 4 cm/s ramp satellite clock error	134
Figure 7.6: Observed maximum separated vertical solutions during approaches with 1 m amplitude satellite clock dithering	135
Figure 7.7: 30 examples of maximum separated solutions in vertical without satellite failures and the proposed threshold slope	136
Figure 7.8: The corresponding residuals from the fitted line of the separated solutions in Figure 7.7.....	137
Figure 7.9: Stand-alone GPS-based FIS cross-track errors without TVPS errors.....	138
Figure 7.10: Stand-alone GPS-based FIS vertical errors without radar altimeter errors.	138
Figure 8.1: Comparison of flight trajectory using the WAAS-based FIS and the Inertial-based FIS	144

List of Tables

Table 3.1: New evaluation of UDREI based on actual performance values observed during Probability of Hazardously Misleading Information (PHMI) analysis.....	61
Table 3.2: New evaluation of GIVEI based on actual performance values observed during Probability of Hazardously Misleading Information (PHMI) analysis.....	63
Table 5.1: Biases and Power Spectra of Accelerometer and Gyro.....	110
Table 5.2: Statistics of the WAAS-aided FIS position errors without radar altimeter and TVPS errors in the critical range	115
Table 6.1: Statistics of the T-D PRP errors at critical regions	126
Table 7.1: Statistics of the T-D PRP Errors at Critical Regions	139
Table 8.1: Comparison of flight inspection system performance.....	145

CERTIFICATE OF FINAL READING OF DISSERTATION

One member of the Reading Committee must certify that he or she has reviewed the final draft of the dissertation as submitted to the Records Office (the form below may be removed or copied from this booklet to be used for this purpose). The final reading of the dissertation should include a review of the following:

Content

All suggested changes have been taken into account and incorporated into the manuscript where appropriate. If the manuscript includes joint group research, the student's contribution is clearly explained in an introduction.

Format

Margin size of 1.5 inches on the binding edge (left edge if single-sided; right edge for even-numbered pages, and left edge for odd-numbered pages if double-sided) and one inch on all other sides; 10 point or larger type size; clearly formed characters; correct divisions of words and text; continuous pagination; 1.5 or double-spaced text (main body); bibliography and footnotes are consistently formatted; all tables and illustrations are in order and appropriately annotated.

Published Materials

If previously published materials are included in the dissertation, publication sources are indicated, written permission has been obtained for copyrighted materials, and all of the dissertation format requirements have been met.

Appearance

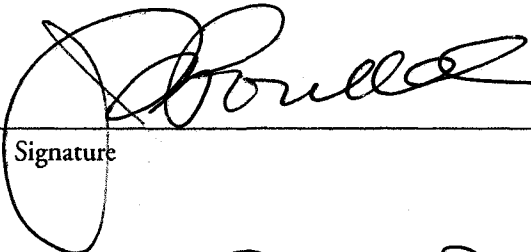
The dissertation is ready-for-publication in appearance and ready for microfilming and binding.

Photocopy

This page may be photocopied, completed, and signed for submission.

To the University Committee on Graduate Studies:

I certify that I have read the dissertation of Eui-Ho Kim
in its final form for submission and have found it to be satisfactory.


Signature 12/5/07
Date

J. David Powell

(Printed Name of Reader)

Aeronautics & Astronautics

(Printed Name of Your Department)

Chapter 1

Introduction to GNSS and Flight Inspection

1.1 Introduction

Global Navigation Satellite Systems (GNSS) are rapidly evolving day by day and becoming an important part of life in a modern society. There are more and more applications in satellite navigation systems, such as the Global Positioning System (GPS) and Wide Area Augmentation System (WAAS), that play a key role in everyday life. These applications include ship and airplane guidance, automatic machine control in agriculture, precise positioning in construction, and even finding friends in crowded urban buildings. This thesis adds one more to the list of innovative applications offered by GNSS: Flight Inspection. This chapter provides the overall background of this thesis.

This chapter is organized as follows. Section 1.2 introduces the overview of the GNSS, where GPS and WAAS are discussed in more detail. Section 1.3 introduces the Instrument Landing System (ILS) and flight inspection. In this section, the previous

and current flight inspection systems are also introduced. Section 1.4 presents the motivation of this thesis. Section 1.5 summarizes thesis contributions.

1.2 Overview of Global Navigation Satellite Systems (GNSS)

Global Navigation Satellite Systems (GNSS) is the generic name given to satellite navigation systems and their augmentation systems. The first generation of the GNSS is the Global Positioning System (GPS) that was developed under the U.S. Department of Defense (DoD) and declared fully operational in 1995 [EngeMisra]. When GPS was being developed, the Soviet Union started developing a similar system, GLONASS. As of 2007, Russia maintains responsibility for GLONASS, but GLONASS is not fully operational and needs to launch several new satellites. The European satellite navigation system is called Galileo. The European Union (EU) sanctioned the development of Galileo in 2002. Unlike GLONASS, Galileo is designed to be fully compatible with GPS. Currently, it is expected that Galileo will become operational after 2010 [EngeMisra]. GPS, GLONASS, and Galileo provide signals for military as well as civil uses.

There are several Satellite Based Augmentation Systems (SBAS). As of 2007, the only fully operational augmentation system supporting vertical guidance is the Wide Area Augmentation System (WAAS) in the U.S.. The Federal Aviation Administration was the key player in developing WAAS whose main purpose is to serve various phases of civilian flight in North America. A similar system to WAAS in Europe is called the European Geostationary Navigation Overlay Service (EGNOS). The EGNOS system is developed and deployed under the European Space Agency (ESA). As of 2007, EGNOS is in its initial operation phase [Lyon]. Another similar system to the WAAS in Japan is the Multi-functional Satellite Augmentation System (MSAS) developed by the Japan Civil Aviation Bureau (JCAB). MSAS is fully compatible and interoperational with WAAS and EGNOS and is now certified for horizontal guidance [Sakai]. More recently, India is working on an Indian space-based augmentation system known as GPS and GEO Augmented Navigation (GAGAN)

[Sisodia]. Japan is undertaking another regional system known as the Quasi-Zenith Satellite System (QZSS) to transmit ranging signals and differential correction signals especially to users in Japan as well as East Asia and the Oceania region [Kogure].

Among the systems described above, current GPS and WAAS are discussed in more detail in the following subsections. After that, modernization of GPS and WAAS are discussed.

1.2.1 Global Positioning System (GPS)

The Global Positioning System (GPS) consists of three segments: the Space Segment, the Control Segment, and the User Segment. The Space Segment consists of a baseline of 24 satellites that are distributed in six orbital planes inclined at 55° relative to the equatorial plane. This constellation is designed such that a user can view at least four satellites at any time and any place on Earth. Figure 1.1 shows the baseline constellation of 24 GPS satellites. The Control Segment comprises monitor stations, ground antennas, and the Master Control Station. Monitor stations are spread over the world and track satellite signals. The information gathered at the monitor stations are transferred to the Master Control Station where ephemeris and satellite clock parameters are computed. Also, the Master Control Station determines satellite health, maintains GPS time, and generates satellite navigation messages. The navigation message is sent to the GPS satellites from the ground antennas via S-band radio link. The Space Segment and the Control Segment are maintained by the DoD [EngeMisra]. Figure 1.2 shows the locations of Control Segment elements over the world. Recently, the DoD has added several new monitor stations to the stations shown in Figure 1.2.

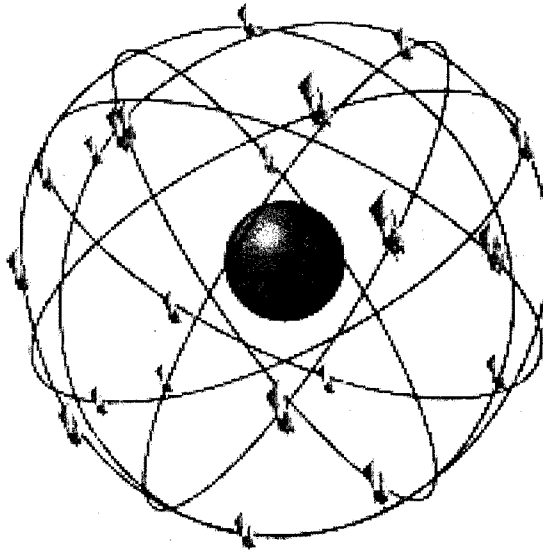


Figure 1.1: A baseline constellation of 24 GPS satellites (Courtesy of FAA)

The User Segment includes military and civil equipment. The User Segment, especially in civil use, is no longer a passive player in satellite navigation systems. Business commerce related to satellite navigation systems grows rapidly and life for civilians more and more heavily depends on GPS or GNSS. As a result, the future of GPS cannot be determined without considering the needs of the User Segment.

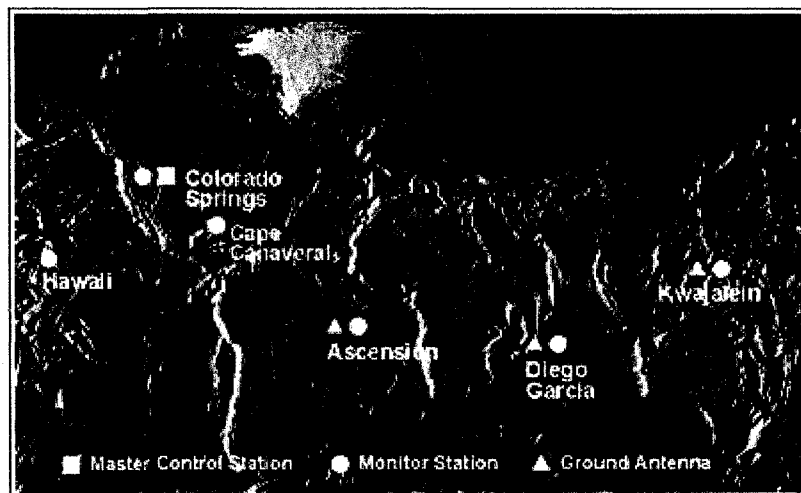


Figure 1.2: Worldwide location of GPS Control Segment elements (Courtesy of FAA)

Currently, the GPS satellites transmit two signals using two radio frequencies in the L-Band L1 and L2. The center frequencies of L1 and L2 are 1575.42 MHz and 1227.60 MHz, respectively. The signal for L1 is available to civil users, but the signal for L2 was originally intended for DoD-authorized users. Each signal has three components [ISGPS]: carrier, ranging code, and navigation data.

The carrier is an RF sinusoidal signal having frequency of L1 or L2. The navigation data is a binary-coded message conveying satellite health status, ephemeris and satellite clock parameters, and almanac. GPS ranging codes are based on pseudo-random noise (PRN) sequences. The special property of the PRN codes is that each GPS satellite can transmit its own unique code at the same frequency without interfering with the codes from other GPS satellites. The PRN codes on the L1 frequency are called coarse/acquisition codes (C/A-codes) and their chipping rate is 1.023 MHz. The PRN codes on the L2 frequency are called precision codes (P(Y)-codes) and their chipping rate is 10.23 MHz. The chipping rate of P(Y)-codes makes the chip length 10 times smaller than the C/A-codes, which means that ranging precision is also much greater. The P(Y)-code is only available for military purposes.

A GPS receiver captures the RF signal and measures the signal transit time for each captured satellite signal. It also decodes the navigation message to determine satellite position and clock parameters. Using the above information, it is possible to compute the user's position, velocity, and time.

The performance in estimating user position, velocity, and time also depends on measurement errors. The GPS measurement errors and their error size are listed in the following bullets [EngeMisra] and illustrated in Figure 1.3.

- Satellite clock modeling error: 2 m (rms)
- Satellite ephemeris prediction: 2 m (rms) along the line of sight vector
- Ionospheric delay error: 2 - 10 m in zenith direction

- Tropospheric delay error: 2.3 - 2.5 m in zenith direction
- Multipath: 0.5 - 1 m in code measurement and 0.5 - 1 cm in carrier measurement in a clean environment
- Receiver noise: 0.25 - 0.5 m (rms) in code measurement and 1 - 2 mm (rms) in carrier measurement

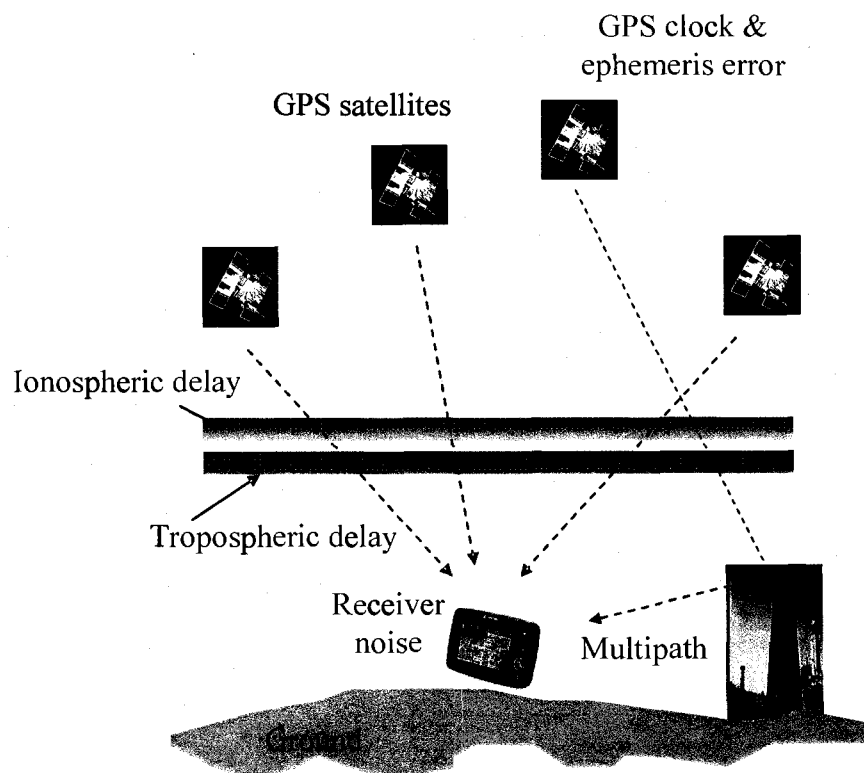


Figure 1.3: Various GPS measurement errors sources

The code and carrier measurements have the same amount of errors from the satellite clock modeling error, satellite ephemeris prediction error, and tropospheric

delay errors. The ionospheric delay is the largest of the errors, but its effect in the code and carrier measurements is equal and opposite, thus enabling an estimation of the error.

1.2.2 Wide Area Augmentation System (WAAS)

The FAA commissioned the Wide Area Augmentation System (WAAS) in 2003 to aid GPS by broadcasting 250 bps messages over the U.S. using two geostationary satellites. With WAAS, the augmented GPS will meet near CAT I precision landing requirements in terms of accuracy, integrity, continuity and availability [Walter06]. Note that the requirements are listed on page 14 in this chapter. Therefore, WAAS greatly helps aircraft operations over the U.S. by providing guidance for oceanic, en route, non-precision, and vertically guided approach phases. If GPS or WAAS were to broadcast hazardous information to a user, WAAS would detect this and issue a flag within six seconds with a confidence level of 99.99999%. WAAS also provides greater than 99.9% availability for vertically guided approach. Availability is defined as the probability that the service meets all requirements for the full duration of the approach. WAAS accuracy (95%) over the U.S. is better than 0.9 meters in the horizontal and 1.3 meters in the vertical [WAASpan]. The conceptual illustration of WAAS is shown in Figure 1.4.



Figure 1.4: Conceptual illustration of Wide Area Augmentation System (Courtesy of FAA)

The broadcast WAAS messages, generated at the WAAS Master Station using the observation from the WAAS reference stations, include [WAASMOPS]:

- Differential corrections: Fast and long-term satellite clock-ephemeris error corrections and ionospheric delay error correction;
- Accuracy of the differential corrections: User Differential Range Error Indicator (UDREI) and Grid Ionospheric Vertical Error Indicator (GIVEI);
- Masks: A mask is used to designate which slot is assigned to a specific satellite for a correction message;
- Geostationary navigation messages: This message updates the location of WAAS geostationary satellites; and
- Parity: The parity provides a secure tool to detect a bit error.

The WAAS geostationary satellites also transmit ranging signals. Therefore, a better satellite geometry can be obtained with WAAS than with stand-alone GPS.

1.2.3 Modernization of GPS and WAAS

To better serve civil and military needs, the modernization plan of GPS and WAAS has been started [Enge03][Walter042]. The modernization of GPS is planned for both military and civil uses by adding new signals. The new civil signals are L2C and L5. The L2C signal is collocated at the L2 frequency with the P(Y)-code and has similar code structure to the L1 C/A code. Some satellites that transmit the L2C signal, Block IIR, have already been launched. However, the full constellation with the L2C signal will not be complete until 2013. The L5 signal will be allocated at the center frequency of 1176.45 MHz and has longer and faster codes than L1 C/A and L2C codes. The satellites that transmit the L5 signal are scheduled to launch in 2008. The full constellation of L5 signals will be completed around 2018. The new military code, called M code, will be allocated at L1 and L2 frequencies. Figure 1.5 summarizes the frequency allocation of current and new signals. These new signals add better correlation properties, multipath mitigation, and better resistance to interference when compared to current GPS.

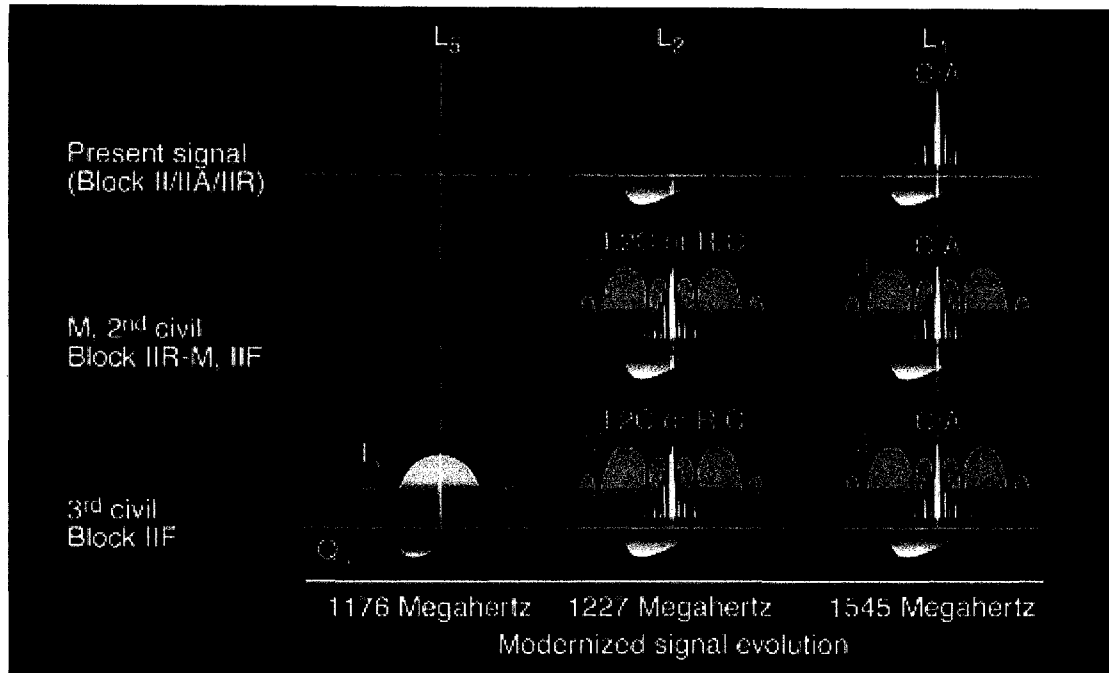


Figure 1.5: Frequency allocation of current and new GPS signals (Courtesy of Aerospace Corp.)

The modernization of WAAS plans to utilize L5 and Galileo [Walter042]. The use of L5 enables a user to simply remove ionospheric delay effects which are the biggest error source in WAAS. The additional ranging sources from Galileo will give the WAAS better accuracy, continuity, and availability. Overall, the modernized WAAS will be expected to provide CAT I level performance throughout the U.S..

1.3 Instrument Landing System and Flight Inspection

1.3.1 Instrument Landing System (ILS)

The Instrument Landing System (ILS) has been a primary landing guidance system worldwide since the 1940s and is expected to serve an additional 30 or more years beyond 2007. The ILS consists of a localizer, a glide-slope, and marker beacons.

The localizer and the glideslope provide horizontal and vertical guidance, respectively, to an approaching airplane for a given runway. Marker beacons provide an indication to pilots of their progress along the glide path. The ILS guidance during approach is illustrated in Figure 1.6: .

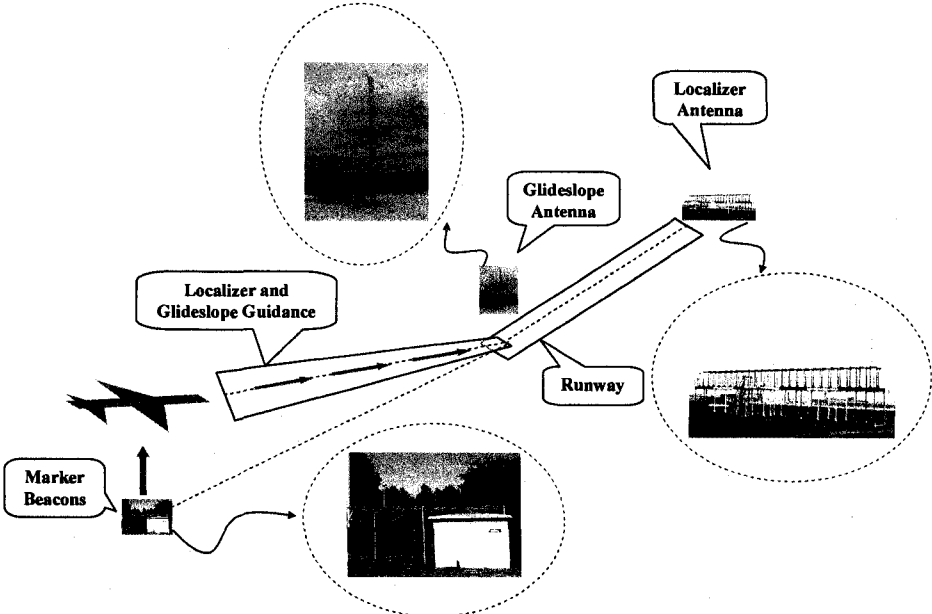


Figure 1.6: An airplane approaches a runway using ILS guidance

The localizer establishes a radiation pattern in space to provide a signal that indicates lateral deviation from the runway centerline [Kayton]. To form this radiation pattern, called Carrier-with-SideBands (CSB), an RF carrier around 110 MHz is modulated with discrete 90 Hz and 150 Hz bands above and below the frequency. The glideslope forms its radiation pattern, CSB, in space in the same way, but its carrier frequency is around 330 MHz. The glideslope provides vertical guidance by indicating vertical deviation from a 3° slope vertical landing course. Figure 1.7 shows the radiation patterns of the localizer and the glideslope and their guidance. The marker beacons simply transmit an audible Morse-code identification signal at 75 MHz.

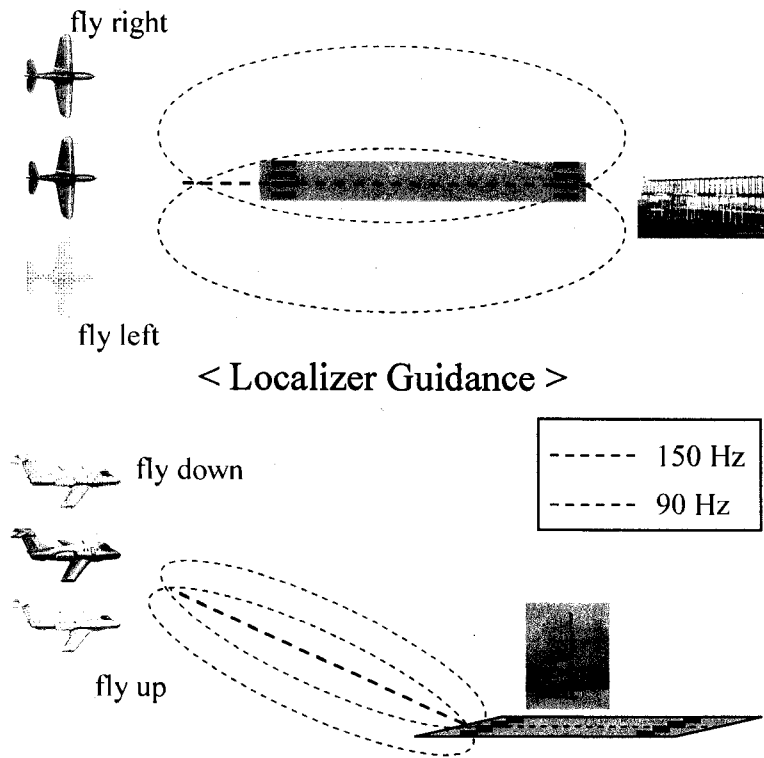


Figure 1.7: Localizer and glideslope radiation patterns and their guidance

Depending on the quality of the ILS, ILS can be categorized into three kinds. Each category is associated with precision approach categories that are distinguished from each other by decision height (DH) and runway visual range (RVR) [Enge96]. The decision height is an altitude at which a pilot must decide to either complete or abort the landing. If the aircraft is performing the approach coupled to an autopilot with guidance from an ILS or WAAS receiver, the pilot must take over and fly the aircraft by hand to land or execute the missed approach procedure at this point. To complete the landing, RVR, a measure of visibility, must be also met. The DH and the RVR for each category are listed in the following bullets.

- CAT I: The DH is at least 200 ft. The RVR is at least 2400 ft.

- CAT II: The DH is between 100 and 200 ft. The RVR is at least 1200 ft.
- CAT III: The DH is less than 100 ft or the RVR is less than 1200 ft.

An ILS may not always provide accurate guidance. In order to ensure the guidance from an ILS within specifications, the ILS must be periodically inspected and calibrated via flight inspection. The next section discusses flight inspection of the ILS.

1.3.2 Flight Inspection for ILS Calibration

The main drawback of the ILS is its sensitivity to multipath. Any changes of surrounding environment from its initial commission or the last calibration can cause a significant accuracy degradation of the ILS. There can also be some drift in the electrical components of the system. For these reasons, the Federal Aviation Administration (FAA) regularly checks and calibrates the ILS to maintain its accuracy.

The accuracy in the guidance of an ILS is checked via flight inspection. During a flight inspection, an aircraft approaches a runway following the ILS guidance. The actual flight path during approach is estimated independently from a Flight Inspection System (FIS). This estimated flight path is compared to the ILS signal to determine the errors in the ILS guidance. If there is a deviation in the ILS guidance, a calibration is required and the ILS electronics are adjusted by ground crews.

Since the duration of the approach usually takes less than a few minutes, an FIS only uses a short set of measurements to estimate the flight path. The aircraft's flight path can be estimated in near-real-time but must be estimated within an accuracy requirement. The accuracy required for a FIS is not rectilinear. Since the ILS is an angular guidance system, the accuracy requirements of a FIS are also angular. The FAA uses the following guidelines. For CAT I ILS, the estimation error (95%) should be less than 0.05 deg from glideslope and localizer antennas down to 30 cm in vertical and 60 cm in cross-track. For CAT II•III ILS, the estimation error (95%) should be

less than 0.015 deg from glideslope and localizer antennas down to 30 cm in vertical and 60 cm in cross-track. In other words, the accuracy requirements become looser as the distance from those antennas increases if XYZ Cartesian coordinates are used. The vertical FIS accuracy requirement for ILS calibration is shown in Figure 1.8 as an example.

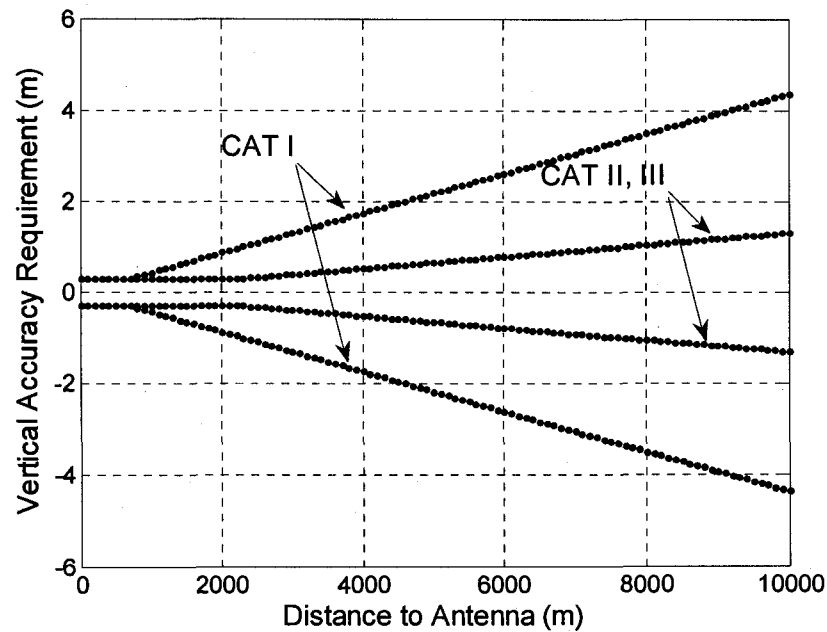


Figure 1.8: Vertical flight inspection system accuracy requirements for ILS calibration

Various sensors and systems have been used in flight inspection for ILS. The next section introduces the previous and current FIS.

1.3.3 History of Flight Inspection Systems

The first instrument used for the ILS calibration was a theodolite, an instrument that measures horizontal and vertical angles [FIH]. Figure 1.9 shows the old fashioned

ILS calibration procedure with a theodolite. This procedure required very skilled people and was time consuming. Then, an automatic light or laser tracker replaced the manual theodolites (around the 1970s-1980s). A light tracker followed a light source installed on the airplane, and a laser tracker followed the reflected laser from the airplane. Flight paths were still estimated on the ground, and the overall ILS calibration procedure still took a significant amount of time. During the 1980s, the Inertial-based Automatic (or Automated) Flight Inspection System (AFIS) was developed [FIH][Scherzinger]. This system uses a navigation grade INS (Inertial Navigation System) as a primary sensor with a barometric altimeter, a radar altimeter, a camera system (TVPS), and a pilot event button. A Kalman filter was used to estimate a flight trajectory by fusing the measurements from those sensors. This system is an automated self-contained system that made the ILS calibration procedure more efficient and convenient than the previous instruments. However, the drawbacks of the Inertial-based AFIS are high cost and degrading accuracy further from a runway. Also, an airplane needs to fly level over the whole runway to calibrate various biases in the INS. Regardless of the drawbacks, this kind of AFIS has continuously evolved and is being used in the U.S. and worldwide. GPS was also added to the sensor suite when it became available in the 1990s.

After precise positioning techniques using differential GPS were developed and commercialized around the 1990s [FIH], the techniques were adapted to a flight inspection system for the ILS calibration problem. This kind of FIS is called the Differential GPS-based Automatic Flight Inspection System (DGPS-based AFIS) [Feit]. This system usually provides a centimeter level of accuracy in real-time without any drifts. However, it requires the time-consuming procedure of setting up a local reference station in each airport, which is the main drawback of the DGPS-based AFIS.

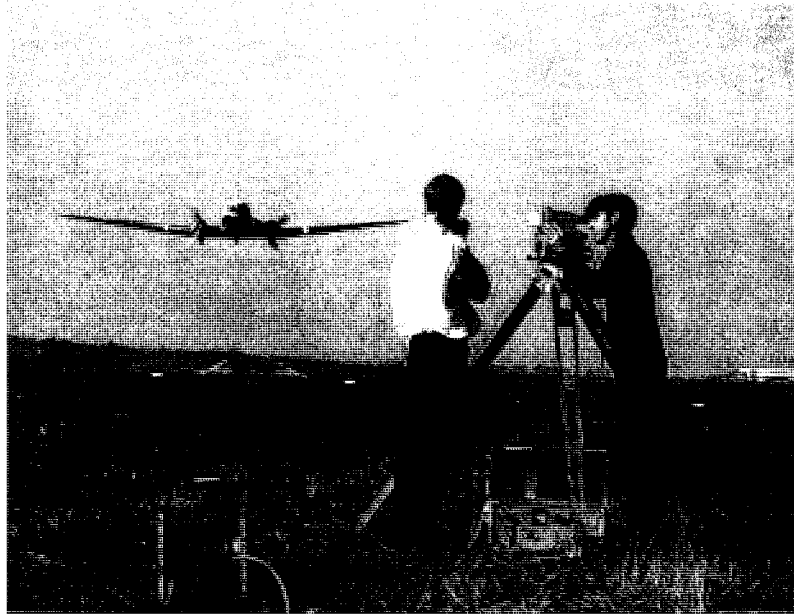


Figure 1.9: The two surveyors on the ground measure the aircraft's deviation from the desired flight path using a theodolite (courtesy of CAHS collection) [DC3]

Current automated FIS are Inertial-based AFIS and DGPS-based AFIS. Figure 1.10 shows an example of a modern computerized FIS. The characteristics of the two current FIS are quite different in terms of cost, accuracy and efficiency. In the U.S., the FAA prefers to use the Inertial-based AFIS mainly due to its efficiency in spite of the higher cost. To inspect numerous ILS across the U.S., efficiency becomes the most important factor.

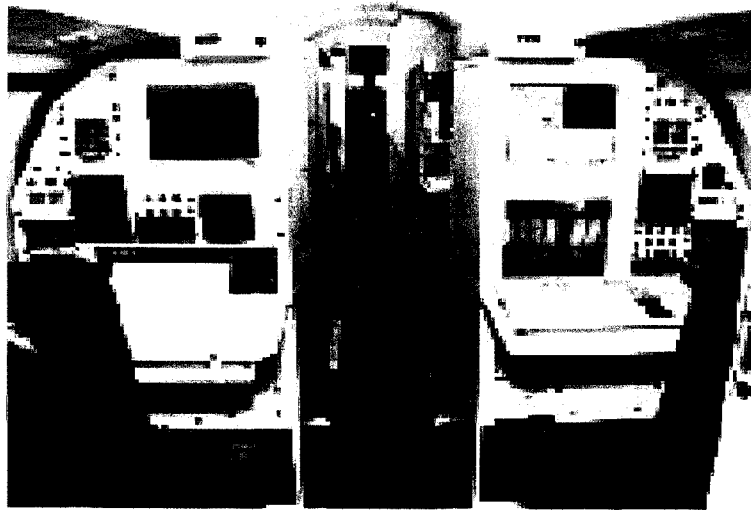


Figure 1.10: Modern computerized FIS (courtesy of NXT, Inc) [NXTFIS]

1.4 Motivation

The flight inspection operation in the U.S. is quite extensive because of the large numbers of ILS. There are around 1200 ILS in the U.S. [Enge96]. The ILS must be inspected every 6 to 9 months and calibrated if necessary. Therefore, it is important to manage the airborne inspection of the ILS in a very efficient way such that no ILS is behind in its scheduled inspection. That is why the FAA mainly uses the Inertial-based AFIS. Unfortunately, the Inertial-based AFIS is expensive because it requires a navigation-grade INS. Obviously, the FAA spends tremendous resources on flight inspection. The motivation of this thesis is to develop a flight inspection system that can achieve high efficiency and low cost at the same time. The expected benefit is that the overall flight inspection procedure can be more manageable in terms of time and costs.

1.5 Thesis Synopsis and Contributions

This thesis is divided into two parts. Part I covers the algorithm developments for improving position accuracy and stability of GPS and WAAS. The developed

algorithms in Part I play a key role later in Part II which covers the developed flight inspection systems and their experimental performance evaluation. Part I consists of Chapters 2, 3, and 4 and Part II consists of Chapters 5, 6, 7, and 8. The synopsis of each chapter is described below, and specific contributions made in each chapter are listed with bullets.

Chapter 2 presents an Adaptive Carrier Smoothing (ACS) technique that selects an optimal carrier smoothing time of a Hatch filter by observing ionospheric delay gradients and multipath with a single frequency receiver. The ACS balances the tradeoffs of using a Hatch filter with a single frequency receiver, which are multipath reduction and induced ionospheric delays. The specific contributions made in this chapter are:

- Investigation of the performance in estimating ionospheric delay gradients by using Ordinary Least-Squares (OLS) and Feasible Generalized Least-Squares (FGLS) on the time series of code minus carrier measurements with a single frequency receiver; and
- Formation of cost functions based on tradeoffs caused when using carrier smoothing for white noise multipath and highly correlated multipath

Chapter 3 presents methods that better optimize WAAS accuracy and stability for a single frequency receiver. In this thesis, the stability in a position solution is defined as the tendency of the position error to remain close to a bias with low noise. This chapter discusses the suboptimal aspect of WAAS in terms of accuracy and how to modify WAAS algorithms to improve its accuracy and stability for accuracy-oriented users. However, the proposed methods lose the firm integrity that WAAS provides. The specific contributions made in this chapter are:

- Termination of WAAS range rate correction to reduce 12 s periodic noise;

- Modification of WAAS suboptimal weighting matrix to optimal weighting matrix for accuracy; and
- Use of Adaptive Carrier Smoothing introduced in Chapter 2 instead of a 100 s Hatch filter.

Chapter 4 presents the reference point-based precise relative positioning methods for real-time and near real-time applications, assuming that an accurate position of a receiver is given at least one time during navigation. The proposed methods are Iono-Free Precise Relative Positioning (I-F PRP) and Time-Differenced Precise Relative Positioning (T-D PRP). The specific contributions made in this chapter are:

- Development of a relative positioning algorithm that uses the sum of code and carrier phase measurements as ranging sources; and
- Further development of carrier-based relative positioning with a single frequency receiver by removing differential ionospheric delay gradients for near-real-time applications.

Chapter 5 introduces the WAAS-aided Flight Inspection System (WAAS-aided FIS). The WAAS-aided FIS is not only designed to have low cost and high efficiency, but it is also designed to use the certified Commercial off-the-shelf (COTS) WAAS receivers that are part of the current FAA flight inspection system such that no significant hardware change is required. Its accuracy is marginal for the FAA flight inspection system accuracy requirements. The WAAS-based FIS can only be used where WAAS (or any SBAS) is available. The specific contributions made in this chapter are:

- Development of the WAAS-based FIS system architecture;
- Development of a fusion algorithm of WAAS and INS to remove WAAS 12 s periodic noise;
- Design of a robust high pass filter that enables use of a low cost INS in the fusion of WAAS and INS; and

- Experimental test of the WAAS-aided FIS using flight test data.

Chapter 6 introduces the WAAS-based Flight Inspection System (WAAS-based FIS). The WAAS-based FIS uses the T-D PRP algorithms described in Chapter 4 and utilizes WAAS correction and integrity messages. Not only does the WAAS-based FIS offer low cost and high efficiency, but it also adequately meets the FAA flight inspection accuracy requirements. This system requires raw GPS and WAAS data, therefore, modification of a certified WAAS receiver is required. The WAAS-based FIS, also, can only be used where WAAS (or any SBAS) is available. The specific contributions made in this chapter are:

- Development of WAAS-based FIS system architecture;
- Optimized T-D PRP with WAAS;
- Flight inspection system integrity methodology with WAAS; and
- Experimental test of the WAAS-based FIS using flight test data.

Chapter 7 introduces the stand-alone GPS-based Flight Inspection System (GPS-based FIS). The stand-alone GPS-based FIS is similar to the WAAS-based FIS, but does not utilize the WAAS data. This system also offers low cost, high efficiency, and accuracy that meets the FAA flight inspection system accuracy requirements. Since the WAAS integrity message is not available, the stand-alone GPS-based FIS is equipped with an integrity monitor called FIS-RAIM. More importantly, this system is operational worldwide. The specific contributions made in this chapter are:

- Development of the stand-alone GPS-based FIS system architecture;
- Flight inspection system integrity methodology with GPS;
- Development of Flight Inspection System (FIS) RAIM to protect against minor satellite failures; and
- Experimental test of the stand-alone GPS-based FIS using flight test data.

Chapter 8 has concluding remarks. The performance of the current flight inspection systems and the developed flight inspection systems are compared. This chapter also discusses future flight inspection systems with modernized or new signals available in GNSS.

PART I

***Algorithm Developments to Improving
Position Stability***

Chapter 2

Adaptive Carrier Smoothing Using Code and Carrier Divergence for a Single Frequency Receiver

2.1 Introduction

The Hatch filter [Hatch] has been widely used in the GPS community as a tool that uses precise but ambiguous carrier phase measurements to smooth noisy pseudorange measurements primarily due to multipath. However, this filter introduces a bias in the filtered range due to ionospheric delay gradients. The magnitude of the bias is a function of carrier smoothing time and ionospheric delay gradients. When a user increases the smoothing time, the user obtains smoother measurements, but suffers a bigger bias. Therefore, there is a trade off between multipath reduction and an induced bias from using a Hatch filter as illustrated in Figure 2.1. To avoid the disadvantage of using a Hatch filter, various methods have been proposed to mitigate multipath: a Kalman filter with modeled platform dynamics [Hwang], a

complementary Kalman filter with GPS velocity [Leppäkoski], and an optimal hatch filter using a multipath model parameterized by an elevation angle and Klobuchar ionosphere model [Park].

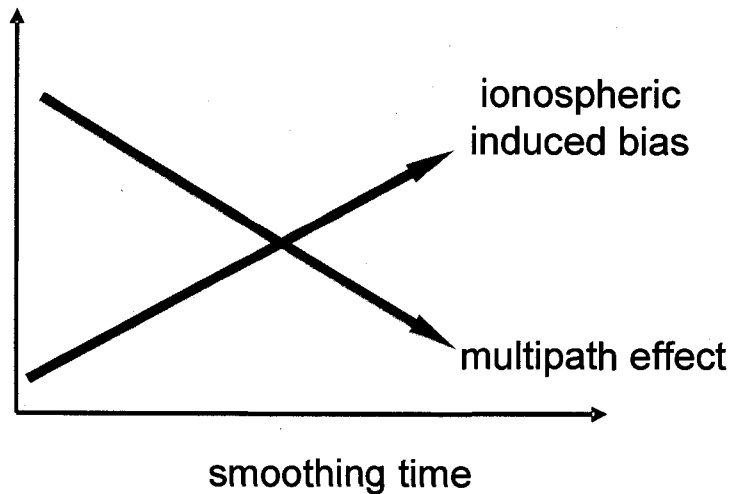


Figure 2.1: Tradeoff in using a Hatch filter

This chapter introduces novel Adaptive Carrier Smoothing (ACS) which gives the user an optimal Hatch filter smoothing window under current ionosphere condition and multipath. Unlike the previous approaches, this method directly estimates the time-varying slant ionospheric delay gradient and multipath in code phase measurements using time series of code minus carrier phase measurements. Using these estimates, two cost functions are constructed for white noise multipath and highly correlated multipath. From the cost functions, an optimal Hatch filter time that balances an induced bias and multipath effect is found. The entire procedure is repeated at a certain rate to adapt to the time-varying condition of ionosphere and multipath.

This chapter is organized as follows. Section 2.2 briefly reviews linear regression theory because it is extensively used to estimate time-varying slant ionospheric delay gradients. Section 2.3 introduces the estimation scheme of the slant

ionospheric delay gradients and multipath characteristics using code minus carrier phase measurements. Section 2.4 presents the details of the ACS algorithms. Section 2.5 presents the test results of the ACS using static and airborne GPS measurements. Lastly, the conclusion is presented in Section 2.6.

2.2 Review of Linear Regression

2.2.1 Linear Regression with White Noise

When the relationship between an observation, y , and a regressor, x , is linear, y can be modeled as

$$y = \beta_0 + \beta_1 x + \varepsilon \quad (2.1)$$

where β_0 is the intercept, β_1 is the slope, and $\varepsilon \sim \text{WN}(0, \sigma^2)$ is white noise.

When the time series of the observation, Y , is available, the linear model can be described in a matrix form as

$$Y = X\beta + \varepsilon \quad (2.2)$$

where Y is an $n \times 1$ vector, X is an $n \times 2$ matrix, β is a 2×1 vector, and ε is an $n \times 1$ vector.

If we can assume that the linear model is reasonable, the unbiased and the most efficient estimate of β can be obtained from ordinary least-squares (OLS) [Montgomery], which is

$$\hat{\beta}_{OLS} = (X^T X)^{-1} X^T Y \quad (2.3)$$

The variance of $\hat{\beta}_{OLS}$ is

$$\text{Var}(\hat{\beta}_{OLS}) = \sigma^2 (X^T X)^{-1} \quad (2.4)$$

2.2.2 Linear Regression with Autocorrelated Noise

When noise is autocorrelated, ordinary least-squares still gives an unbiased solution, but the variance is no longer minimized. In this case, generalized least-squares gives the best solution [Montgomery].

The linear model with autocorrelated noise is

$$\begin{aligned} Y &= X\beta + \varepsilon \\ E(\varepsilon) &= 0, \text{Var}(\varepsilon) = \sigma^2 V \end{aligned} \quad (2.5)$$

where V is a nonsingular and positive definite matrix.

The unbiased and most efficient solution for Equation (2.5) is

$$\hat{\beta}_{GLS} = (X^T V^{-1} X)^{-1} X^T V^{-1} Y \quad (2.6)$$

The variance is

$$\text{Var}(\hat{\beta}_{GLS}) = \sigma^2 (X^T V^{-1} X)^{-1} \quad (2.7)$$

Generalized least-squares (GLS) requires a covariance matrix, V , of the noise to estimate the coefficients β . However, the covariance matrix is usually also unknown. Therefore, it is necessary to estimate the covariance matrix and the coefficients at the same time. This is a well-known problem in econometrics and can be solved by using a two step process, called feasible generalized least-squares (FGLS) [Brockwell].

The FGLS algorithm is:

- 1) Find β_{OLS} from OLS and compute residuals, $e = Y - X\beta_{OLS}$
- 2) Fit an autoregressive and moving average (ARMA) model to e
- 3) Find β_{GLS} using V computed from the ARMA model
- 4) Compute $e = Y - X\beta_{GLS}$
- 5) Return to 1) until β_{GLS} stabilizes

The FGLS includes Auto Regressive-Moving Average (ARMA) modeling for the residual errors. Discussion about ARMA modeling can also be found in [Brockwell].

2.3 Estimation of the Slant Ionospheric Delay Gradient and Multipath Characteristics Using Code Minus Carrier Phase Measurements

The estimation of slant ionospheric delay gradients with a single frequency receiver has been introduced in the past [Batchelor][Xie]. These techniques used the difference of code and carrier phase measurements as estimation sources with a Kalman filter and a CUSUM method, respectively. This difference is also used as estimation sources in this section, however, the OLS and the FGLS with a sliding window are investigated as estimators.

2.3.1 Linear Model of Code minus Carrier Phase Measurements

The range measurements in a GPS receiver are code and carrier phase measurements. The code phase measurements, ρ , and the carrier phase measurements, Φ , can be written as [EngeMisra]

$$\begin{aligned}
\rho &= r + c[\delta t_u - \delta t_s] + I + T + \varepsilon_\rho \\
\Phi &= r + c[\delta t_u - \delta t_s] - I + T + \lambda N + \varepsilon_\Phi
\end{aligned}
\tag{2.8}$$

where r is the true range between a receiver and a satellite, c is the speed of light, δt_u and δt_s are receiver and satellite clock errors, respectively, I is ionospheric delay, T is tropospheric delay, λ is the carrier wavelength, and N is an integer ambiguity. ε_ρ and ε_Φ include multipath, thermal noises, and modeling errors in the code and carrier phase measurements, respectively. Since multipath is usually bigger than other receiver related noise, ε_ρ and ε_Φ will be considered as multipath in code and carrier phase measurements.

The difference, y , between ρ and Φ at time t is

$$\begin{aligned}
y_t &= \rho_t - \Phi_t \\
&= 2I_t - \lambda N + \varepsilon_{t,\rho} - \varepsilon_{t,\Phi}
\end{aligned}
\tag{2.9}$$

This difference includes ionospheric delays multiplied by two, an integer ambiguity, and multipath. Our interest here is twofold: to estimate a slant ionospheric delay gradient because it is directly related to an induced ionospheric delay from using carrier smoothing, and to separate the multipath from the other terms. Before jumping into this problem, it should be noted that the ionospheric delays slowly change with respect to time during nominal ionospheric days. Therefore, the gradient can be seen as a constant during a short time window (tens of minutes). Modeling $I_t = t \cdot \beta_1 + \text{const}$, Equation (2.9) can be rewritten as

$$\begin{aligned}
y_t &= \beta_0 + 2t \cdot \beta_1 + \varepsilon_{t,\rho} - \varepsilon_{t,\Phi} \\
&\approx \beta_0 + 2t \cdot \beta_1 + \varepsilon_{t,\rho}
\end{aligned}
\tag{2.10}$$

where $\beta_0 = 2 \cdot \text{const} - \lambda N$.

In Equation (2.10), $\varepsilon_{t,\phi}$ is ignored because it is much smaller than $\varepsilon_{t,\rho}$.

Expressing the time series of Equation (2.10) in a matrix form yields

$$\begin{bmatrix} y_{t_1} \\ y_{t_2} \\ \vdots \\ y_{t_n} \end{bmatrix} = \begin{bmatrix} 1 & 2 \cdot t_1 \\ 1 & 2 \cdot t_2 \\ \vdots & \vdots \\ 1 & 2 \cdot t_n \end{bmatrix} \underbrace{\begin{bmatrix} \beta_0 \\ \beta_1 \end{bmatrix}}_{\beta} + \begin{bmatrix} \varepsilon_{t_1,\rho} \\ \varepsilon_{t_2,\rho} \\ \vdots \\ \varepsilon_{t_n,\rho} \end{bmatrix} \underbrace{\varepsilon_{\rho}}_{\bar{\varepsilon}_{\rho}}$$

$$Y = X\beta + \bar{\varepsilon}_{\rho} \quad (2.11)$$

Now, the problem becomes finding β_1 in the presence of $\bar{\varepsilon}_{\rho}$. If $\bar{\varepsilon}_{\rho}$ is close to white noise, ordinary least-squares (OLS) is the best estimator. However, if $\bar{\varepsilon}_{\rho}$ is highly correlated, feasible generalized least-squares (FGLS) should be used instead of OLS.

2.3.2 Multipath Characteristics from Dynamic and Static GPS Receiver Measurements

Assuming that we have a good estimate of $\hat{\beta}$ from Equation (2.11), the multipath can be separated as follows.

$$\hat{\bar{\varepsilon}}_{\rho} = Y - X\hat{\beta} \quad (2.12)$$

In general, multipath characteristics are closely related to the motion of the platform where a GPS antenna is installed. In this subsection, the general characteristics of airborne and static ground multipath will be discussed.

Figure 2.2 shows a time series of mean subtracted airborne code minus carrier phase measurements and its fitted line using first order linear regression.

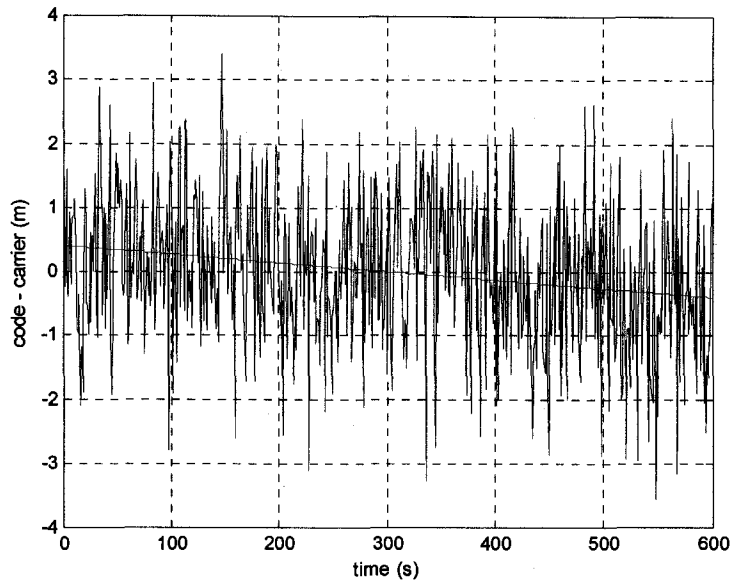


Figure 2.2: Unbiased code minus carrier over 600 seconds with a regressed line for airborne measurements

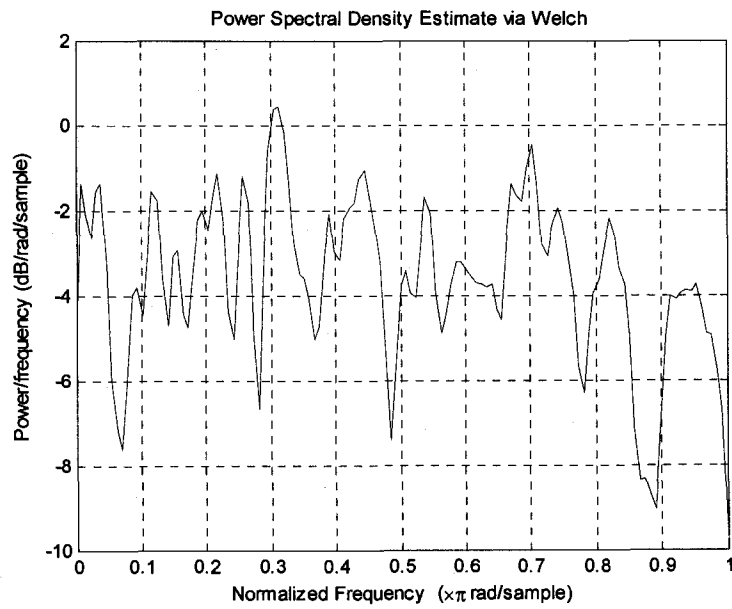


Figure 2.3: Power spectral density of airborne multipath in code minus carrier phase measurements

The power spectral density of the residuals in Figure 2.2 is shown in Figure 2.3 which indicates that the multipath can be treated as white noise. Therefore, it should be reasonable to use OLS to estimate the ionospheric delay gradients for airborne measurements.

Figure 2.4 shows a time series of mean subtracted static ground code minus carrier phase measurements and its fitted line using first order linear regression.

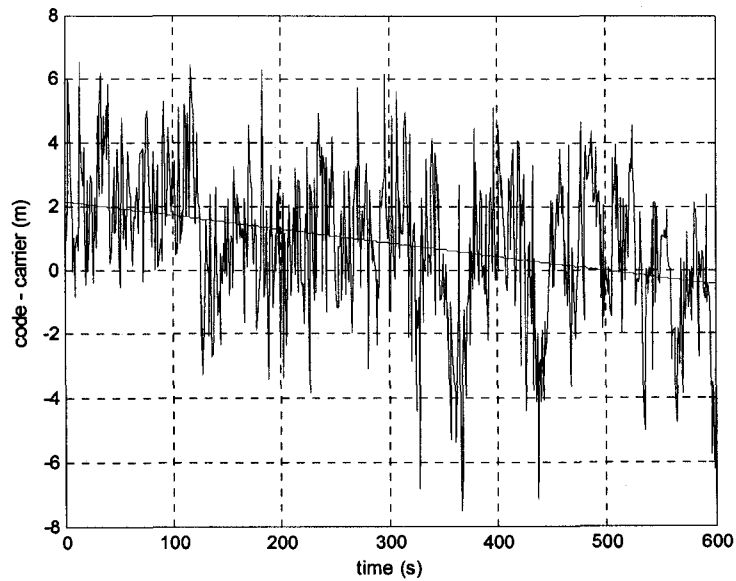


Figure 2.4: Unbiased code minus carrier over 600 seconds with a regressed line for static ground measurements

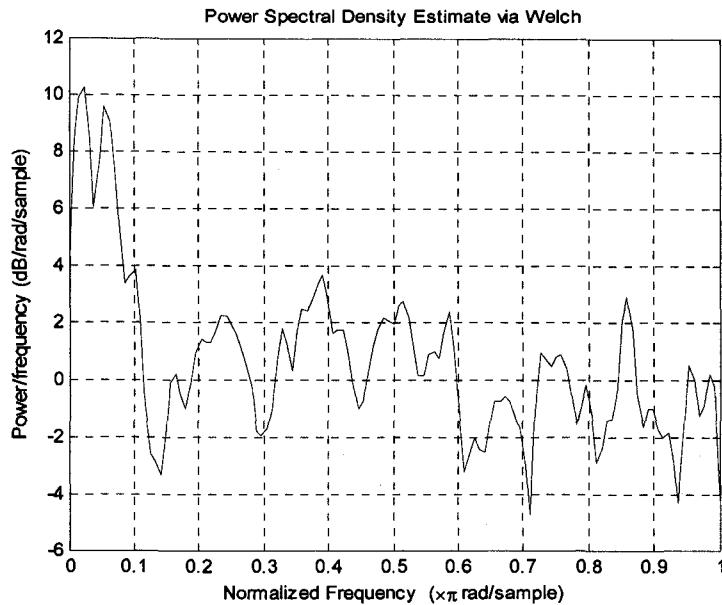


Figure 2.5: Power spectral density of static ground noise in code minus carrier measurements

Figure 2.5 shows the power spectral density of the residuals in Figure 2.4. It shows that the residuals have significant low frequency noise, from which we can conclude that the noise is highly autocorrelated. Therefore, FGLS is desirable for this case.

In this subsection, it is shown that OLS is appropriate for use in airborne measurements while FGLS is appropriate for static ground measurements. However, OLS is much easier to implement than the FGLS and is preferable in practice. In the next subsection, the feasibility of using OLS on the measurements with correlated noise will be discussed.

2.3.3 Comparison of the Estimated Slant Ionospheric Delay Gradient Using OLS and FGLS on Measurements with Autocorrelated Noise

Feasible generalized least-squares (FGLS) is an asymptotically optimal estimator when noise is correlated. Even though it is desirable to use FGLS, it is

computationally intensive for use in real-time. Therefore, we should make sure that it is worth while to pursue FGLS with the burden of the heavy computation for our applications.

FGLS and OLS are implemented on the 800 second window of static ground measurements whose multipath has a strong correlation. Figure 2.6 shows the difference of the results from FGLS and OLS.

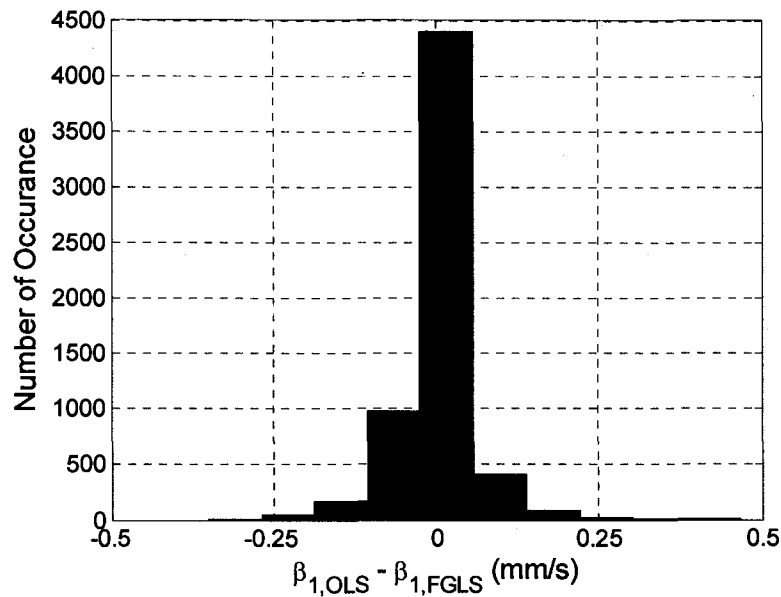


Figure 2.6: Histogram of the difference of the estimated ionospheric delay rates from using OLS and FGLS

The mean of the difference in the histogram is -0.0004 mm/s, and the standard deviation is 0.06 mm/s. These statistics are insignificant for most applications since a slant ionospheric delay gradient of tens of mm/s is of concern in practice. Thus, OLS can be used instead of FGLS on the code minus carrier phase measurements having autocorrelated noise.

2.3.4 Evaluation of the Estimated Slant Ionospheric Delay Gradient with Dual Frequency Measurements

In the previous subsection, it is shown that OLS can be used instead of FGLS without much sacrifice. Now, the estimated ionospheric delay gradients from OLS are compared to the gradients measured from a dual frequency receiver in order to check the adequacy of our linear model.

The reference ionospheric delay gradients from a dual frequency receiver are computed as follows [EngeMisra];

$$S_{L1,t} = \frac{f_{L2}^2}{f_{L1}^2 - f_{L2}^2} [(\Phi_{L1} - \lambda_{L1}N_{L1}) - (\Phi_{L2} - \lambda_{L2}N_{L2})], \quad (2.13)$$

$$\Delta I_{t,dual} = S_{L1,t} - S_{L1,t-1}$$

where f_{L1} and f_{L2} are the center frequencies of the L1 and L2 bands, and λ_{L1} and λ_{L2} are the carrier wavelengths on the L1 and L2 frequencies. It should be noted that $\Delta I_{t,dual}$ from a dual frequency receiver is a direct estimate of an ionospheric delay and includes some noise.

Figure 2.7 shows $\Delta I_{t,dual}$ and $\hat{\beta}_{t,1}$ for one satellite computed from implementing OLS on static ground measurements on a nominal ionospheric day. These estimates are computed every 15 seconds, and an 800 second sliding window is used to estimate $\hat{\beta}_{t,1}$. Since raw $\Delta I_{t,dual}$ is quite noisy, it is smoothed by a non-causal moving average filter and shown as circles. The $\hat{\beta}_{t,1}$ is also filtered by using a causal moving average filter because estimates using a sliding window are likely to have some noise. Unlike $\Delta I_{t,dual}$, $\hat{\beta}_{t,1}$ is filtered because smoothing is impossible in real time. The smoothing and filtering process uses the past 30 minutes of estimates. From Figure 2.7, we can see that the filtered slant ionospheric delay gradient, shown as dots, using the

linear model closely follows the measured slant ionospheric delay gradient from a dual frequency receiver.

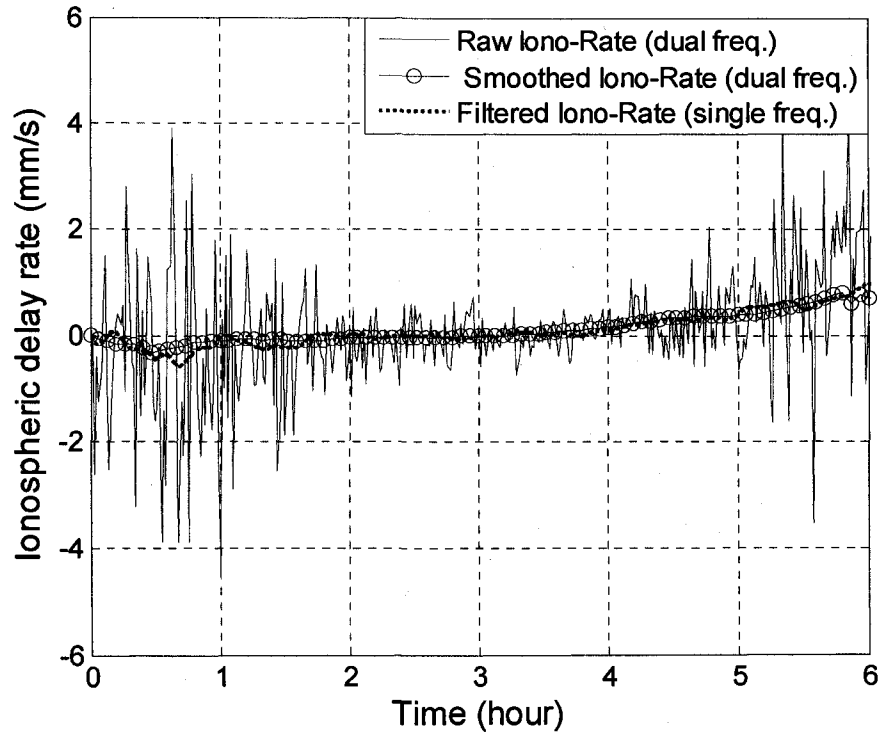


Figure 2.7: Comparison of the estimated ionospheric delay gradients from a dual frequency receiver and from using the linear model during a nominal ionospheric day

Figure 2.8 shows the histogram of the difference between $\Delta I_{t,dual}$ and $\hat{\beta}_{t,1}$ for all satellites in view during 19 hours on Oct 26, 2006 at Atlantic City. The mean of the difference is -0.047 mm/s, and the standard deviation is 0.15 mm/s. These results indicate that the linear model is quite satisfactory for many applications.

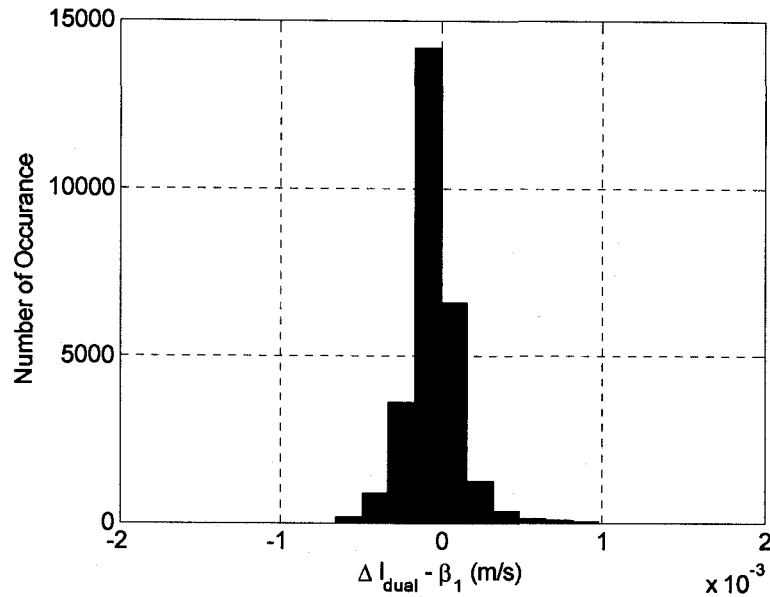


Figure 2.8: Histogram of the difference between smoothed $\Delta I_{t,dual}$ and $\hat{\beta}_{t,1}$ for all satellites in view during 19 hours on Oct 26, 2006 at Atlantic City

2.4 Adaptive Carrier Smoothing (ACS)

In the previous section, it is shown that slant ionospheric delay gradients and multipath in code phase measurements can be estimated with a single frequency receiver. It is also shown that the estimated gradients match the measured gradients from a dual frequency receiver with sufficient accuracy for most applications. This section introduces the optimal adaptive carrier smoothing technique based on the estimated ionospheric delay gradients and multipath. This section includes the error propagation caused by a Hatch filter and cost function formulations with respect to white noise multipath and sinusoidal multipath.

2.4.1 Error Propagation in Carrier Smoothed Range from Using a Hatch Filter

Using a Hatch filter, the carrier-smoothed pseudorange at time t , $\bar{\rho}_t$, is given by [EngeMisra]

$$\bar{\rho}_t = \frac{1}{k} \rho_t + \frac{k-1}{k} (\bar{\rho}_{t-1} + \Phi_t - \Phi_{t-1}) \quad (2.14)$$

where ρ_t is a code phase measurement, Φ_t is a carrier phase measurement, and k is a carrier smoothing time.

We can define the error, e , in the smoothed pseudorange as [Walter041]

$$e_t = \bar{\rho}_t - r_t - c[\delta t_u - \delta t_s] - T_t - I_t \quad (2.15)$$

From Equation (2.14) and (2.15), we can find the error dynamics as follows.

$$e_t = \frac{k-1}{k} e_{t-1} - 2 \frac{k-1}{k} (I_t - I_{t-1}) + \frac{1}{k} \varepsilon_{t,\rho} \quad (2.16)$$

If we consider the initial error, e_0 , to be zero and a constant ionospheric delay gradient such as $(I_t - I_{t-1}) = a$, then the solution of the error is given by

$$e_t = -2 \sum_{i=0}^{t-1} \phi^{i+1} a + \frac{1}{k} \sum_{i=0}^{t-1} \phi^i \varepsilon_{t-i,\rho} \quad (2.17)$$

where $\phi = \frac{k-1}{k}$. The assumption on the constant ionospheric delay gradient is valid for tens of minutes on nominal ionospheric days.

Furthermore, when t is large, the steady state error, e_{ss} , becomes

$$\begin{aligned}
e_{ss} &= -2\left(\frac{\phi}{1-\phi}\right)a + \frac{1}{k} \sum_{i=0}^{t-1} \phi^i \varepsilon_{t-i,\rho} \\
&= -2(k-1)a + \frac{1}{k} \sum_{i=0}^{t-1} \phi^i \varepsilon_{t-i,\rho}
\end{aligned} \tag{2.18}$$

From Equation (2.18), it should be noted that the steady state error, e_{ss} , of the carrier smoothing filter is a function of an ionospheric delay gradient, multipath in the code phase measurements, and a carrier smoothing time. The trade off of using a Hatch filter is that with a longer carrier smoothing time, there is a bigger bias and lesser multipath effects in ε_{ss} .

2.4.2 Cost Function Formulation with White Noise Multipath

Based on e_{ss} , a cost function, which is only a function of k , can be constructed. From the cost function, an optimal k minimizing the cost function can be found. This subsection shows the derivation of a cost function with white noise multipath and the corresponding spaces of optimal k and costs.

The error contributed from white noise multipath in Equation (2.18) is

$$e_{Mw} = \frac{1}{k} \sum_{i=0}^{t-1} \phi^i \varepsilon_{t-i,\rho} \tag{2.19}$$

When the multipath is assumed to be white, i.e $\{\varepsilon_{n,\rho}\} \sim WN(0, \sigma^2)$, the variance of e_{Mw} can be computed as follows.

$$\begin{aligned}
E(e_{Mw})^2 &= E\left(\frac{1}{k} \sum_{i=0}^{t-1} \phi^i \varepsilon_{t-i,\rho}\right)^2 \\
&= \frac{1}{k^2} E\left(\sum_{i=0}^{t-1} \phi^i \varepsilon_{t-i,\rho} \sum_{j=0}^{t-1} \phi^j \varepsilon_{t-j,\rho}\right) \\
&= \frac{1}{k^2} E\left(\sum_{i=0}^{t-1} \phi^{2i} \varepsilon_{t-i,\rho}^2\right) \\
&= \frac{\sigma^2}{k^2} \left(\frac{1}{1-\phi^2}\right) \\
&= \frac{\sigma^2}{k^2} \left(\frac{1}{1-\left(\frac{k-1}{k}\right)^2}\right) \\
&= \frac{\sigma^2}{2k-1}
\end{aligned} \tag{2.20}$$

Therefore, a cost function for white noise multipath can be defined as follows.

$$\begin{aligned}
J_w(k) &= \mu J_I + J_{Mw} \\
&= 4\mu(k-1)^2 a^2 + \frac{\sigma^2}{2k-1}
\end{aligned} \tag{2.21}$$

where a and σ are assumed to be given, J_I is the square of the induced bias, and J_{Mw} is the variance of filtered multipath. μ is a weighting factor that can adjust the trade off space of J_I and J_{Mw} , and it can be determined by studying the generated trade off spaces with various values of μ .

Figure 2.9 shows the optimal k chosen with respect to given ionospheric gradients and standard deviations of multipath when μ is set to 0.05.

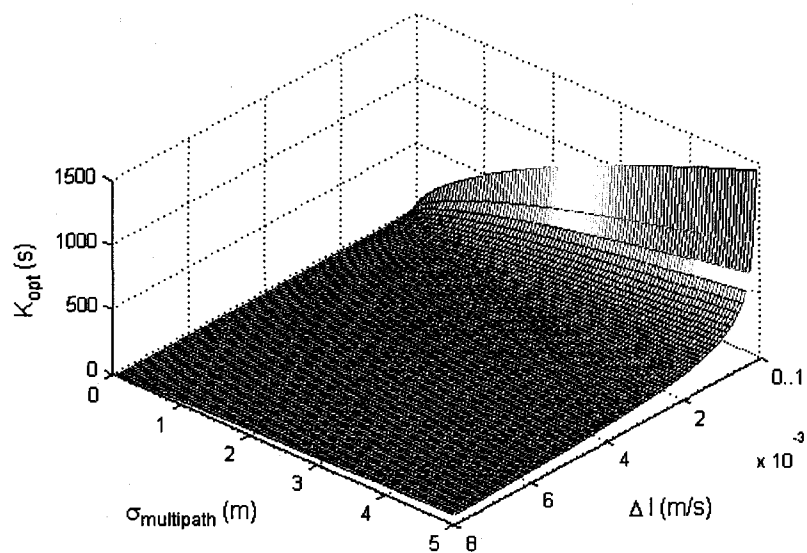


Figure 2.9: Optimal k 's with white noise multipath assumption with respect to the standard deviations of multipath and ionospheric delay gradients

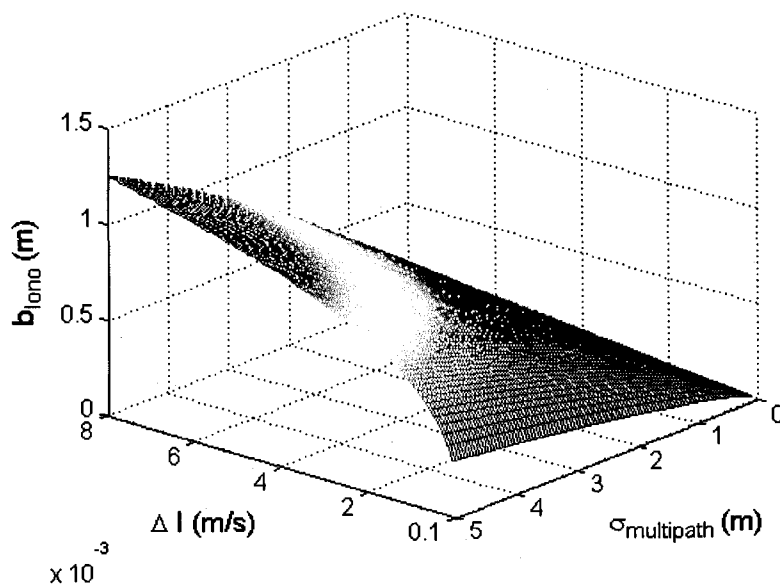


Figure 2.10: Induced bias from using optimal k 's from Figure 2.9 with respect to standard deviations of multipath and ionospheric delay gradients

Figure 2.10 and Figure 2.11 show the induced bias and variance of filtered multipath with respect to the optimal k in Figure 2.9.

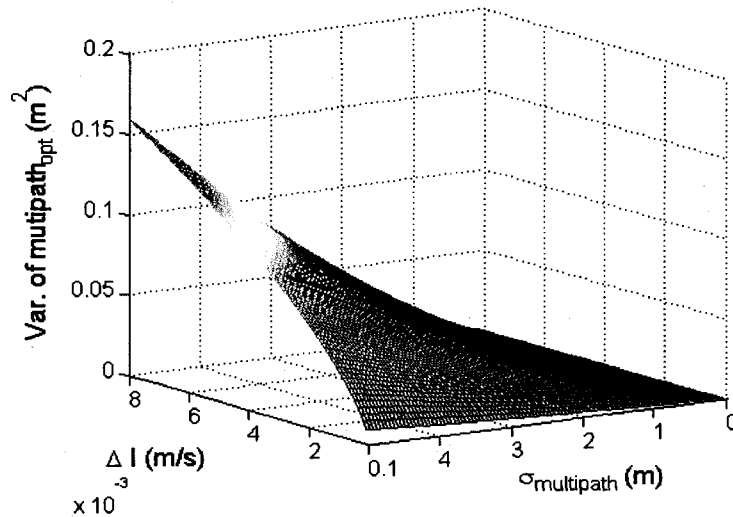


Figure 2.11: Variance of filtered multipath from using optimal k from Figure 2.9 with respect to standard deviations of multipath and ionospheric delay gradients

The assumption on the white noise multipath is not valid for static ground users but is reasonable for airborne users as shown in Subsection 2.3.2. Therefore, the optimal k obtained from white noise multipath is recommended for airborne users.

2.4.3 Cost Function Formulation with Autocorrelated Multipath

Highly correlated multipath on the ground can be seen as a quasi-sinusoidal wave. This quasi-sinusoidal wave also can be seen as the weighted sum of infinitely many sine and cosine waves. Among the many waves, low frequency noise is difficult

to filter in general, which is the same case as when using a Hatch filter for multipath reduction. This fact leads to how to treat the quasi-sinusoidal wave in the formulation of the cost function.

Let us model quasi-sinusoidal multipath as one cosine wave

$$M_s = A \cos(\omega \cdot t + \alpha) \quad (2.22)$$

where A is an amplitude, ω is the most distinct low frequency and α is an unknown phase.

A reasonable guideline to determine A and ω from the estimated multipath is as follows.

- 1) Compute Fast Fourier Transform (FFT) of multipath
- 2) Find the frequency which has the most distinct magnitude in low frequency, and designate it as ω
- 3) Compute the sampled σ and designate A as 2σ

Figure 2.12 shows true multipath and a modeled cosine wave. The true multipath is separated from code minus carrier phase measurements measured from a static ground antenna using OLS.

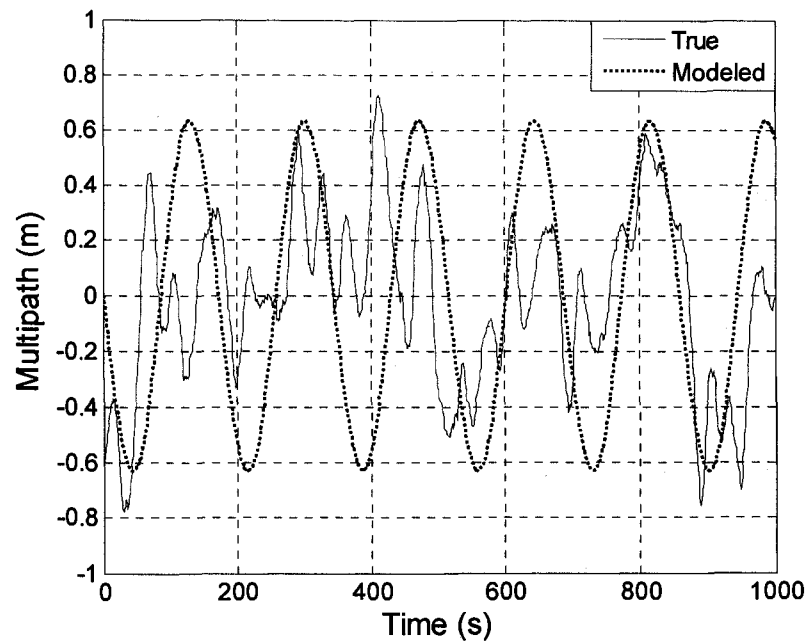


Figure 2.12: True multipath and a modeled sine wave from static ground measurements

When the modeled cosine wave is put into a Hatch filter, the output, e_{Ms} , has the following expression with a large t .

$$\begin{aligned}
e_{Ms} &= \frac{A}{k} \sum_{i=0}^{t-1} \phi^i \cos(\omega i + \alpha) \\
&= \frac{A}{k} \sum_{i=0}^{t-1} \frac{\phi^i}{2} (e^{j(\omega i + \alpha)} + e^{-j(\omega i + \alpha)}) \\
&= \frac{A}{2k} \sum_{i=0}^{t-1} [(\phi e^{j\omega})^i e^{j\alpha} + (\phi e^{-j\omega})^i e^{-j\alpha}] \\
&= \frac{A}{2k} \left[\frac{e^{j\alpha}}{1 - \phi e^{j\omega}} + \frac{e^{-j\alpha}}{1 - \phi e^{-j\omega}} \right] \\
&= \frac{A}{2k} \frac{e^{j\alpha} + e^{-j\alpha} - \phi(e^{j(\omega - \alpha)} + e^{-j(\omega - \alpha)})}{1 - \phi e^{j\omega} - \phi e^{-j\omega} + \phi^2} \\
&= \frac{A \cos(\alpha) - \phi \cos(\alpha - \omega)}{k (1 - 2\phi \cos(\omega) + \phi^2)} \\
&= \frac{A \cos(\alpha - \omega)}{k \sqrt{1 - 2\phi \cos(\omega) + \phi^2}}
\end{aligned} \tag{2.23}$$

Equation (2.23) uses Euler's formula that states [Boyce]

$$e^{ix} = \cos(x) + i \sin(x) \tag{2.24}$$

where e is the base of the natural logarithm and i is the imaginary unit.

Then, the amplitude of the filtered cosine wave, A_F , is

$$A_F = \frac{A}{k \sqrt{1 - 2\phi \cos(\omega) + \phi^2}} \tag{2.25}$$

Figure 2.13 shows the outputs of the true and the modeled multipath from a Hatch filter when $k = 100$. In this simulation, an ionospheric delay gradient is set to 0. The bound of the filtered cosine wave in steady state is $\pm A_F$. From Figure 2.13, we can see that this bound very closely indicates the maximum and minimum of the filtered true multipath, which is the main motivation of modeling the autocorrelated or quasi-sinusoidal multipath to a cosine wave.

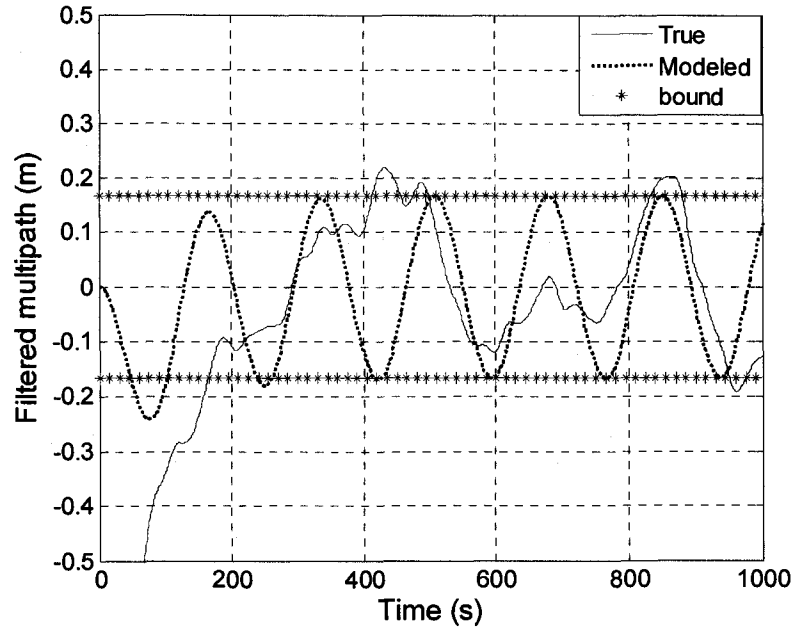


Figure 2.13: Filtered multipath of true and modeled multipath from a Hatch filter

Then a cost function with a sinusoidal multipath, J_s , can be constructed as the sum of the cost due to an induced bias and the cost due to A_F .

$$\begin{aligned}
 J_s &= \mu J_I + J_{Ms} \\
 &= 4\mu(k-1)^2 a^2 + \frac{A^2}{k^2(1-2\phi \cos(\omega) + \phi^2)}
 \end{aligned} \tag{2.26}$$

Figure 2.14 shows the optimal k chosen with respect to given ionospheric gradients and amplitudes. μ is set to 1 and ω is set to 0.04 rad/s which has a 157 second period and is commonly observed from static ground measurements.

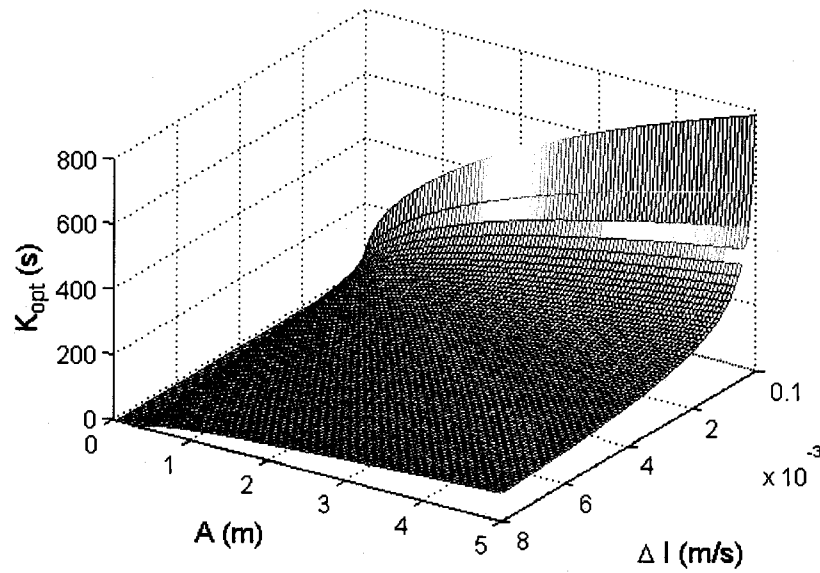


Figure 2.14: Optimal k with sinusoidal multipath with respect to the amplitudes of a cosine wave and the ionospheric delay gradients

Figure 2.15 and Figure 2.16 show the induced bias and the amplitude, respectively, of a filtered cosine wave using the optimal k in Figure 2.14.

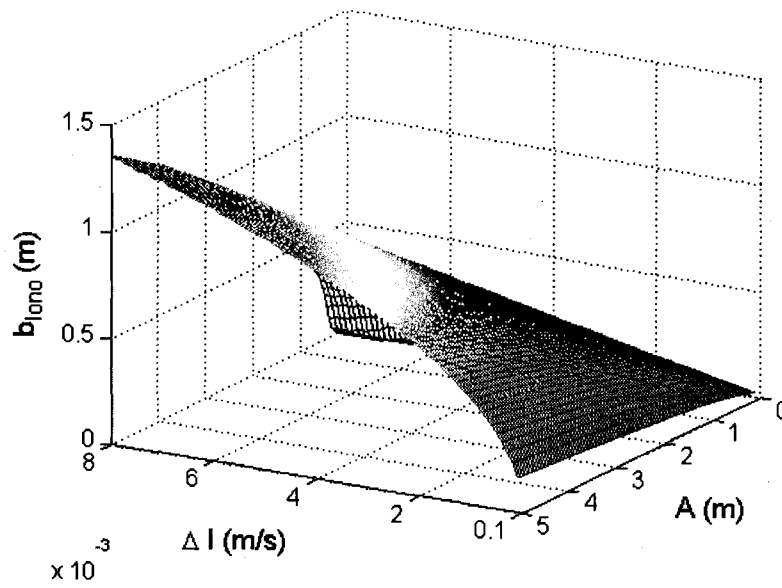


Figure 2.15: Induced biases from using the optimal k from Figure 2.13 with respect to the amplitudes of a cosine wave and the ionospheric delay gradients

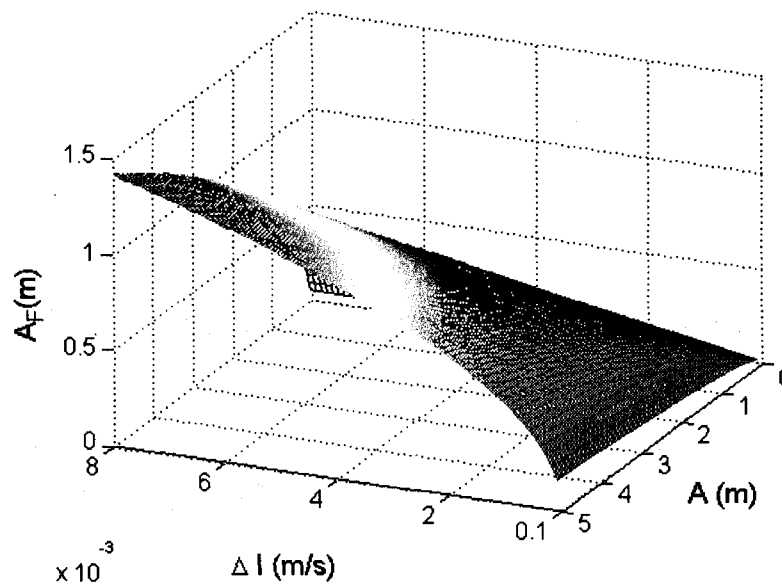


Figure 2.16: Amplitudes of a filtered cosine wave from using the optimal k from Figure 2.13 with respect to the amplitudes of a cosine wave and the ionospheric delay gradients

2.4.4 Adaptive Carrier Smoothing (ACS) Procedures

As a summary of the previous discussion, the adaptive carrier smoothing procedures are illustrated in Figure 2.17. The estimator takes code minus carrier phase measurements for all satellites and outputs estimated parameters. The parameters for the white noise multipath assumption are slant ionospheric delay gradients and standard deviation of multipath. The parameters for the highly correlated multipath are the slant ionospheric delay gradients and the amplitude and the distinct low frequency for the modeled cosine wave. These estimates are low pass filtered, and the optimizer selects an optimal smoothing time based on the filtered estimates. This optimal smoothing time is put into a Hatch filter.

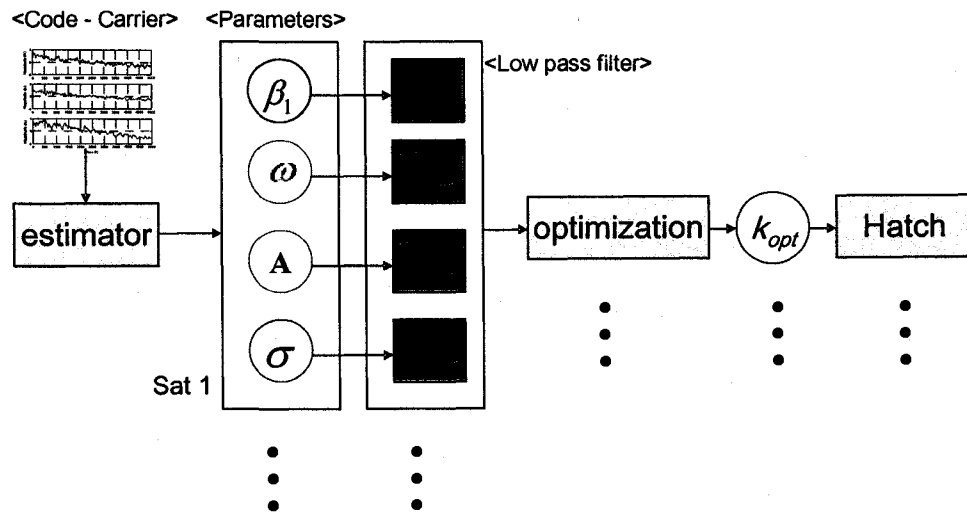


Figure 2.17: Adaptive carrier smoothing (ACS) procedures

2.5 Results

The Adaptive Carrier Smoothing (ACS) techniques are implemented on airborne and static ground measurements. The window of code minus carrier phase measurements is set to 800 seconds. The parameters are estimated every 15 seconds and filtered using a low pass filter. Therefore, the optimal carrier smoothing time is also updated every 15 seconds. The results are presented in this section with respect to airborne and static ground measurements.

2.5.1 Airborne Measurements

Figure 2.18 shows the estimated standard deviation of airborne multipath, $\hat{\sigma}_{\text{multipath}}$, and estimated slant ionospheric delay gradients over time, \hat{a} , for one satellite. Figure 2.19 shows the optimal smoothing time corresponding to the estimated parameters in Figure 2.18.

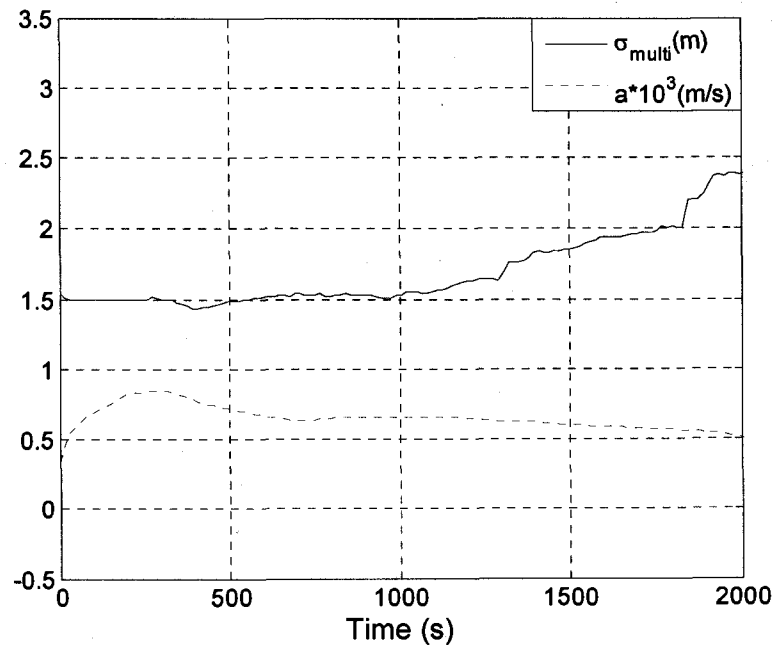


Figure 2.18: $\hat{\sigma}_{\text{multipath}}$ and \hat{a} from airborne measurements for one satellite

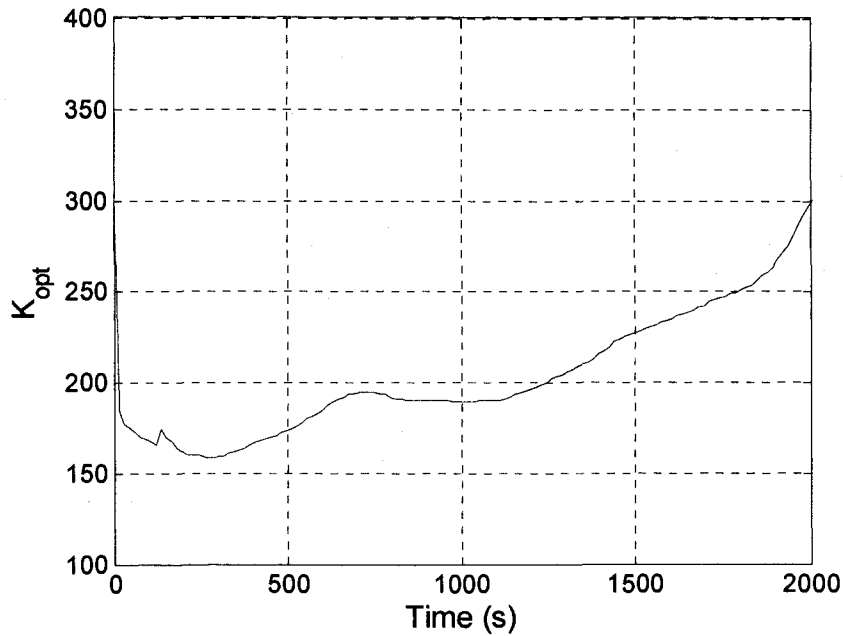


Figure 2.19: Optimal k for airborne measurements corresponding to the estimated parameters in Figure 2.18

In Figure 2.18, $\hat{\sigma}_{multipath}$ increases over time, but \hat{a} decreases. Therefore, optimal k is increasing because a user will have smoother position solutions without adding a significant induced bias to them.

Figure 2.20 compares the position errors obtained from using a 100 second Hatch filter and ACS with the white noise multipath assumption. Interestingly, significant noise reduction is observed from 1700-2200 seconds while using the ACS as compared to the other times. The reason is that there were two satellites at very low elevation angles, and severe multipath was observed in the code phase measurements. Figure 2.21 shows the elevations angles over time of all satellites used in the test.

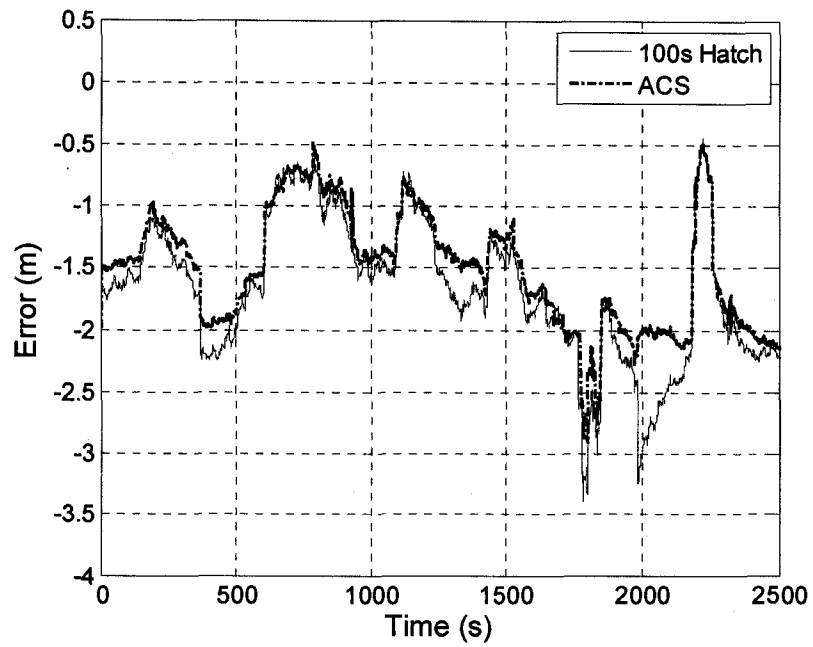


Figure 2.20: Position errors from using the 100 s Hatch filter and the ACS with white noise multipath assumption on airborne measurements

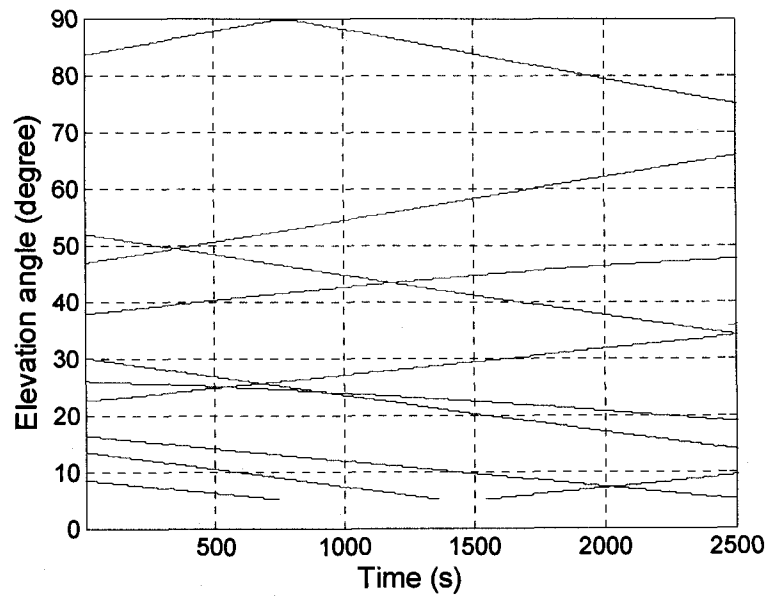


Figure 2.21: Elevation angles in degrees of the satellites in the test for airborne measurements

2.5.2 Static Ground Measurements

Figure 2.22 shows the amplitude and frequency for the modeled cosine wave, \hat{A}_F and $\hat{\omega}$, and estimated ionospheric delay rate, \hat{a} , for one satellite.

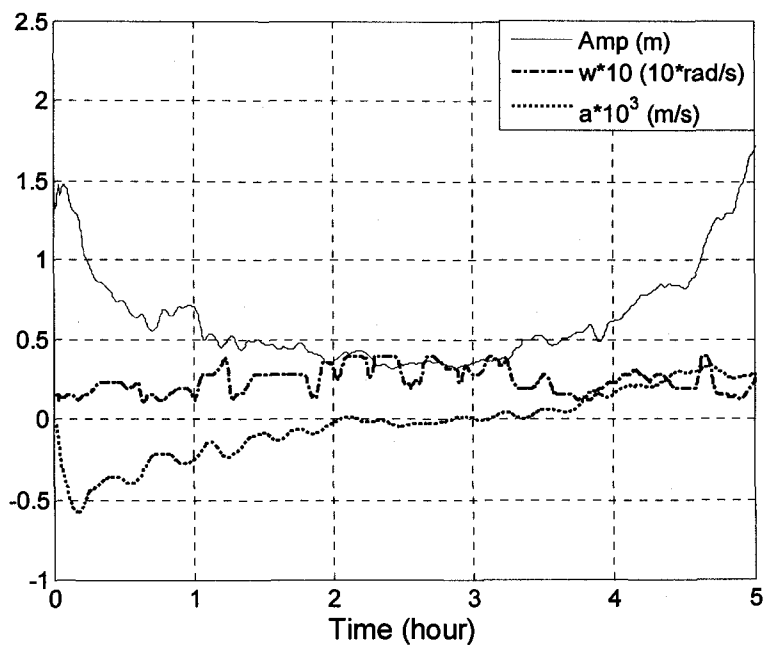


Figure 2.22: \hat{A} , $\hat{\omega}$, and \hat{a} for one satellite from ground measurements

Figure 2.23 shows the behavior of the optimal k corresponding to the estimated parameters in Figure 2.22. There are several large peaks in the smoothing time when the ionospheric delay gradient is very close to zero. In principal, the smoothing time can increase up to infinity when the ionospheric delay rate is exactly zero.

Figure 2.24 compares position errors obtained from using a 100 second Hatch filter and the ACS with a sinusoidal multipath assumption. In this example,

ionospheric delay gradients are small for all satellites, thus the ACS gives a larger smoothing time than 100 s and results in much smoother position solutions.

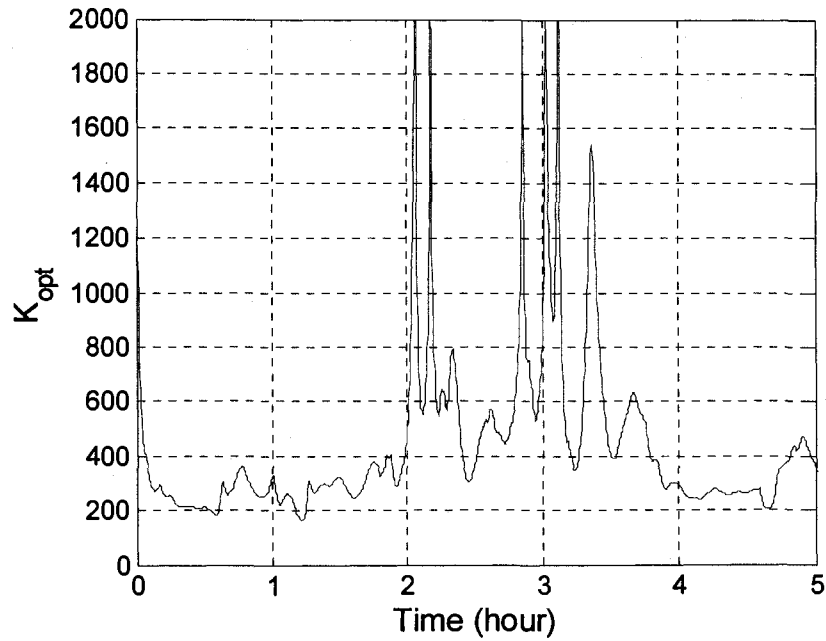


Figure 2.23: Optimal k corresponding to the estimated parameters in Figure 2.22

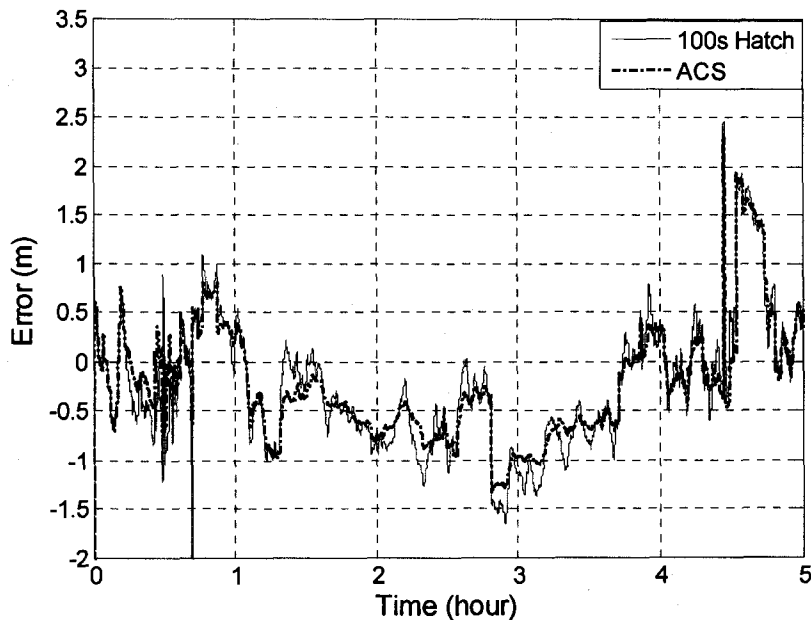


Figure 2.24: The position errors from using a 100 s hatch filter and the ACS with a sinusoidal multipath assumption on static ground measurements

2.6 Discussion

It is shown that the estimation of slant ionospheric delay gradients with a single frequency receiver is very promising. It is observed that the estimates are exceptionally good when a satellite is at high elevation angles. However, when an elevation angle is low, the estimates have errors as large as 1 mm/s. The reasons for the relatively poor performance at low elevation angles are severe multipath and a rapid change in variance of multipath. The problem due to change in variance can be partially fixed by using variance-stabilizing transformations [Montgomery], but severe multipath at low elevation angles will still make it difficult to estimate accurate slant ionospheric delay rates. Therefore, when satellites are at low elevation angles, it is recommended that high integrity users limit a maximum carrier smoothing time or compute an optimal carrier smoothing time by setting a minimum ionospheric delay rate based on a confidence interval. For white noise multipath, the 95% confidence

interval for the ionospheric delay rate is $\hat{\beta}_{t,1} \pm 0.6$ mm/s when an 800 s sliding window and a standard deviation of 2 m are considered.

2.7 Conclusion

In this chapter, the novel Adaptive Carrier Smoothing (ACS) technique was introduced. The unique feature of the ACS is that it provides an optimal Hatch filter smoothing time based on estimated ionospheric delay gradients and multipath using two cost functions for white noise multipath and highly correlated multipath. The estimation of ionospheric delay gradients using OLS and FGLS and formulation of the cost functions were discussed in detail. The ACS technique was tested both on dynamic airborne and static ground measurements taken on nominal ionospheric days. From the suggested cost functions and the particular measurements, the optimal carrier smoothing times were usually much bigger than 100 seconds both for airborne and static ground measurements because there were no observed large ionospheric gradients. As a result, the position solutions using the ACS were smoother than the position solutions using a 100 s carrier smoothing time without having a significant induced bias for both tests.

Even though it is rather hard to quantify the smoothness obtained from the ACS, the difference of the two position solutions provides reasonable estimates. For example, in the result for the static ground measurements, the positions using adaptive carrier smoothing tend to be inside the position using the 100 s Hatch filter. The differences of the two position solutions have a mean close to zero and standard deviations of 22 cm in East, 35 cm in North, and 56 cm in Up. Therefore, roughly speaking, these values are the smoothness gained from using the ACS for the particular data set.

Overall, the ACS introduced in this paper is expected to be more useful in times or places where the ionosphere is very active and multipath is severe. In addition, it is recommended that more aggressive users tweak the cost function to better fit their own preferences. In the algorithms developed in Chapters 6 and 7, the estimation of the

ionospheric gradient was utilized and found to contribute an improvement to the accuracy and the integrity.

Chapter 3

Optimizing WAAS Accuracy/Stability for a Single Frequency Receiver

3.1 Introduction

When the Wide Area Augmentation System (WAAS) was developed, integrity was heavily emphasized because the main motivation of the WAAS is to serve various flight operations in the U.S. [Enge96]. Therefore, the WAAS integrity equations are carefully constructed to ensure the integrity with 99.99999% confidence while satisfying greater than 99.9% availability [Walter97]. As a result, accuracy is emphasized less and sometimes compromised to meet the strict FAA integrity requirements.

Although WAAS was primarily developed for aviation, more and more general GPS receivers have WAAS capability. Therefore, WAAS can be easily accessed by a standard user. However, a standard user typically does not need such high integrity, but wants better accuracy. If WAAS integrity can be relaxed, there is room for improvement in the accuracy and stability of WAAS position solutions. In this thesis,

the stability in a position solution is defined as the tendency of the position error to remain close to a bias with low noise.

WAAS has an unnecessary feature that causes it to have periodic noise. When WAAS was designed, Selective Availability (SA) was the biggest error source. The feature in WAAS dealing with SA is the Range Rate Correction (RRC). Although SA was permanently turned off in 2000, the RRC is still required in a certified WAAS receiver and results in additional noise.

In this chapter, three methods are suggested for optimizing WAAS to have better accuracy and stability: modifying the WAAS weighting matrix, Adaptive Carrier Smoothing (introduced in Chapter 2 [Kim071]) instead of a Hatch filter with a short smoothing window, and nullifying the Range Rate Correction (RRC). First, the WAAS weighting matrix typically does not represent the most likely current signal conditions because it uses overbounding variances. This is necessary for WAAS to ensure its integrity. However, from the accuracy point of view, the suboptimal weighting matrix may corrupt position solutions. Therefore, by modifying the weighting matrix to better represent current signal conditions, it is more likely that better position solutions than the standard WAAS can be obtained. Second, Adaptive Carrier Smoothing (ACS) provides an optimal way of using a Hatch filter by providing an optimal Hatch filter smoothing window according to current ionosphere and multipath conditions. Therefore, the ACS better balances multipath reduction and induced ionospheric delays than standard WAAS. Third, RRC is turned off because it causes a 12 second periodic noise in position solutions [Kim062]. Therefore, nullifying RRC will reduce the amplitude of the 12 second periodic noise. The methods proposed in this chapter have not been reported previously by others.

This chapter is organized as follows. Section 3.2 discusses the modification of the WAAS weighing matrix. Section 3.3 presents the effects of nullifying RRC in the range domain. The ACS will not be discussed here since it was discussed in Chapter 2. Section 3.4 shows the test results of the proposed three methods using static GPS and WAAS data. Finally, conclusions will be presented in Section 3.5.

3.2 Modification of WAAS Weighting Matrix

A WAAS receiver uses a weighting matrix to compute position. This weighting matrix is closely related to the WAAS protection level equations which use the variance of a Gaussian distribution overbounding a true error distribution. The weighting matrix is diagonal and consists of a total variance, σ_i^2 , which is the sum of the four error variances [WAASMOPS]:

$$\sigma_i^2 = \sigma_{i,flt}^2 + \sigma_{i,UIRE}^2 + \sigma_{i,air}^2 + \sigma_{i,tropo}^2 \quad (3.1)$$

where i indicates a specific satellite, $\sigma_{i,flt}^2$ is the variance of fast and long term correction residuals, $\sigma_{i,UIRE}^2$ is the variance of ionospheric delay correction residuals, $\sigma_{i,air}^2$ is the variance of airborne receiver errors, and $\sigma_{i,tropo}^2$ is the variance of tropospheric error correction residuals.

Using the total variances for each satellite, the weighting matrix is constructed as follows.

$$W = \begin{bmatrix} \frac{1}{\sigma_1^2} & 0 & \dots & 0 \\ 0 & \frac{1}{\sigma_2^2} & \dots & 0 \\ \vdots & \vdots & \vdots & \vdots \\ 0 & 0 & \dots & \frac{1}{\sigma_n^2} \end{bmatrix} \quad (3.2)$$

It would be ideal if the weighting matrix perfectly represented the true error variance. However, most of the time this weighting matrix does not closely represent the current true error variance of the WAAS because each variance must be inflated to protect against possible unobserved large errors, which is the philosophy of WAAS integrity. Therefore, if the tight WAAS integrity requirement is relaxed, the weighting matrix can be modified to better represent true error variances for an accuracy-

oriented user, which requires a better evaluation of the total variance. The new total variance, $\sigma_{new_i}^2$, has the following expression.

$$\sigma_{new_i}^2 = \sigma_{i,new_flt}^2 + \sigma_{i,new_UIRE}^2 + \sigma_{i,new_air}^2 + \sigma_{i,tropo}^2 \quad (3.3)$$

$\sigma_{new_i}^2$ has the modified variances except the variance of the tropospheric delay, and the new weighting matrix uses the new total variances. The modified three variances are discussed in the following subsections.

3.2.1 Modification of the Variance of Fast and Long Term Correction Residuals, $\sigma_{new_flt}^2$

The variance of fast and long term correction residuals, $\sigma_{i,flt}^2$, is computed as described in [WAASMOPS].

$$\sigma_{flt}^2 = \begin{cases} (\sigma_{UDRE} \cdot \delta UDRE + \varepsilon_{fc} + \varepsilon_{rrc} + \varepsilon_{llc} + \varepsilon_{er})^2, & \text{if } RSS_{UDRE} = 0 \\ (\sigma_{UDRE} \cdot \delta UDRE)^2 + \varepsilon_{fc}^2 + \varepsilon_{rrc}^2 + \varepsilon_{llc}^2 + \varepsilon_{er}^2, & \text{if } RSS_{UDRE} = 1 \end{cases} \quad (3.4)$$

where RSS_{UDRE} is the root-sum-square flag in Message Type 10. σ_{UDRE} is the standard deviation of User Differential Range Error (UDRE) from Message Types 2-6 and 24. $\delta UDRE$ is a location-specific modifier for σ_{UDRE} [Walter01]. ε_{fc} , ε_{rrc} , ε_{llc} , and ε_{er} are the degradation parameters for fast correction data, range rate correction data, long term correction or GEO navigation message data, and en route through NPA (Non-precision approach) applications.

σ_{UDRE} is evaluated from a UDRE indicator ($UDREI_i$) provided from Message Types 2-6 and 24. The conversion table in the WAAS MOPS from the $UDREI$ to

σ_{UDRE} is shown in Table 3.1. In Table 3.1, a new UDRE variance, $\sigma_{new_UDRE}^2$, is also shown, which is obtained from the statistics of post-processed user differential range errors without ionospheric delays corresponding to each UDREI. Compared to the MOPS UDRE variance, the new UDRE variance is smaller because it does not conservatively bound errors but rather is close to the true error variance.

In addition to the new UDRE variances, σ_{flt}^2 can be improved by ignoring the correction degradation variances which include ϵ_{fc} , ϵ_{rrc} , ϵ_{llc} and ϵ_{er} because the fast and long term errors typically grow much more slowly than the degradation factors. $\delta UDRE$ is set to unity because the ephemeris errors that it is designed to protect against rarely occur. Therefore, the new variance of fast and long term correction residuals can be simplified as follows.

$$\sigma_{new_flt}^2 = \sigma_{new_UDRE}^2 \quad (3.5)$$

Table 3.1: New evaluation of UDREI based on actual performance values observed during Probability of Hazardously Misleading Information (PHMI) analysis

UDREI	UDRE	MOPS UDRE Variance(m ²)	New UDRE Variance (m ²)
0	0.75	0.0520	0.0260
1	1.0	0.0924	0.0296
2	1.25	0.1444	0.0332
3	1.75	0.2830	0.0368
4	2.25	0.4678	0.0404
5	3.0	0.8315	0.0633
6	3.75	1.2992	0.0892
7	4.5	1.8709	0.1169
8	5.25	2.5465	0.154
9	6.0	3.3260	0.216

10	7.5	5.1968	0.275
11	15.0	20.787	0.512
12	50.0	230.9661	0.600
13	150.0	2078.695	5.40
14	NM	-	-
15	DNU	-	-

3.2.2 Modification of the Variance of User Ionospheric Range Error,

$$\sigma_{new_UIRE}^2$$

When the WAAS-based ionospheric delay corrections are applied to a user, the variance of the user ionospheric range error is computed as follows [WAASMOPS].

$$\sigma_{UIRE}^2 = F_{pp}^2 \cdot \sigma_{UIVE}^2 \quad (3.6)$$

where F_{pp} is the obliquity factor and σ_{UIVE}^2 is the variance of User Ionospheric Vertical Error (UIVE).

The WAAS MOPS states that the computation of σ_{UIVE}^2 shall include the degradation of ionospheric corrections, ε_{iono} . Again, this degradation factor is ignored since the ionospheric delay corrections typically degrade much more slowly than ε_{iono} .

Then, σ_{UIVE}^2 can be computed as follows

$$\sigma_{UIVE}^2 = \sum_{n=1}^N W_n \cdot \sigma_{n,GIVE}^2 \quad (3.7)$$

where W is a weighting factor which is a function of the Ionospheric Piece Point (IPP). N is the number of Ionosphere Grid Points (IGPs) used for the interpolation of

ionospheric vertical delay at an Ionospheric Piece Point (IPP). σ_{GIVE}^2 is the variance of Grid Ionosphere Vertical Error (GIVE) and is evaluated from the Grid Ionosphere Vertical Error Indicator (GIVEI) sent by Message Type 26.

Like σ_{UDRE} , σ_{GIVE} in the MOPS is very conservative. Table 3.2 compares the GIVE variance in the MOPS, σ_{GIVE}^2 , and the new GIVE variance, $\hat{\sigma}_{new_GIVE}^2$. $\hat{\sigma}_{new_GIVE}^2$ is again computed from the statistics of post-processed residual Grid Ionospheric Vertical Error corresponding to each GIVEI.

Table 3.2: New evaluation of GIVEI based on actual performance values observed during Probability of Hazardously Misleading Information (PHMI) analysis

GIVEI	GIVE	MOPS Variance(m ²)	New Variance (m ²)
0	0.3	0.0084	0.0084
1	0.6	0.0333	0.0136
2	0.9	0.0749	0.0187
3	1.20	0.1331	0.0210
4	1.5	0.2079	0.0230
5	1.8	0.2994	0.0255
6	2.1	0.4075	0.0272
7	2.4	0.5322	0.0289
8	2.7	0.6735	0.0306
9	3.0	0.8315	0.0323
10	3.6	1.1974	0.0432
11	4.5	1.8709	0.0675
12	6	3.3260	0.110
13	15	20.787	0.304
14	45	187.0826	0.951
15	NM	-	-

Therefore, a new variance of user ionospheric range error is computed as follows.

$$\hat{\sigma}_{UIRE}^2 = F_{pp}^2 \cdot \hat{\sigma}_{new_UIVE}^2 \quad (3.8)$$

where

$$\hat{\sigma}_{new_UIVE}^2 = \sum_{n=1}^N W_n \cdot \hat{\sigma}_{n,new_GIVE}^2 \quad (3.9)$$

3.2.3 Modification of the Variance of Airborne Receiver Errors, $\sigma_{RN_M}^2$

The variance of airborne receiver errors is computed as follows [WAASMOPS].

$$\sigma_{air}^2 [i] = \sigma_{noise}^2 [i] + \sigma_{multipath}^2 [i] + \sigma_{divg}^2 [i] \quad (3.10)$$

where

$$\sigma_{multipath} [i] = 0.13 + 0.53e^{(-\theta[i]/10^\circ)} \quad (\text{in meters}) \quad (3.11)$$

$\sigma_{multipath}$ is the variance of multipath for airborne equipment. $\theta[i]$ is the elevation angle of satellite i in degrees. σ_{divg} is defined as the difference between the induced error at the steady-state responses of an implemented Hatch filter and the standard Hatch filter which uses 100 s as a smoothing window. The difference shall be greater than zero if the implemented filter uses a different smoothing time than 100 s. σ_{noise} is the standard deviation of a normal distribution which bounds the errors associated with GNSS receiver noise.

Therefore, σ_{air} bounds the remaining receiver noises and airborne multipath after the carrier smoothing. σ_{air} is not only very conservative, but it is designed for an

airborne user. To have a more realistic variance of receiver noise and multipath, this term is replaced by $\hat{\sigma}_{RN_M}$ computed based on the observation of ionospheric delay gradients, receiver noise, and multipath using code and carrier divergence (CCD). Carrier smoothing time also affects $\hat{\sigma}_{RN_M}$. Therefore, after k_{opt} is chosen from minimizing J_w and J_s in Equations (2.21) and (2.26) in Chapter 2, $\hat{\sigma}_{RN_M}$ can be obtained by substituting k_{opt} back into Equations (2.21) and (2.26). Then, $\hat{\sigma}_{RN_M_w}$ for white noise multipath is computed as follows.

$$\hat{\sigma}_{RN_M_w} = 4(k_{opt} - 1)^2 a^2 + \frac{\sigma^2}{2k_{opt} - 1} \quad (3.12)$$

$\hat{\sigma}_{RN_M_s}$ for sinusoidal multipath is computed as follows

$$\hat{\sigma}_{RN_M_s} = 4(k_{opt} - 1)^2 a^2 + \frac{(2\sigma)^2}{k_{opt}^2 (1 - 2\phi_{opt} \cos(\omega) + \phi_{opt}^2)} \quad (3.13)$$

where $\phi_{opt} = \frac{k_{opt} - 1}{k_{opt}}$.

3.3 Nullifying Range Rate Correction

When WAAS was developed, the range rate correction, RRC, was designed to overcome Selective Availability (SA) which is now permanently turned off. However, a certified WAAS receiver still applies the RRC because it is required in the WAAS MOPS.

The range rate correction, RRC, is computed by a user as follows:

$$RRC(t_{of}) = \frac{PRC_{current} - PRC_{previous}}{\Delta t} \quad (3.14)$$

where PRC is the broadcast fast corrections and t_{of} is the time of applicability. Δt is the time difference between $PRC_{current}$ and $PRC_{previous}$.

The broadcast fast clock correction message has a 12 second periodic pattern in short time due to its 6 second update rate and 0.125 meter resolution. The RRC makes the amplitude of the periodic noise even bigger. Figure 3.1 clearly shows the benefit of nullifying the RRC.

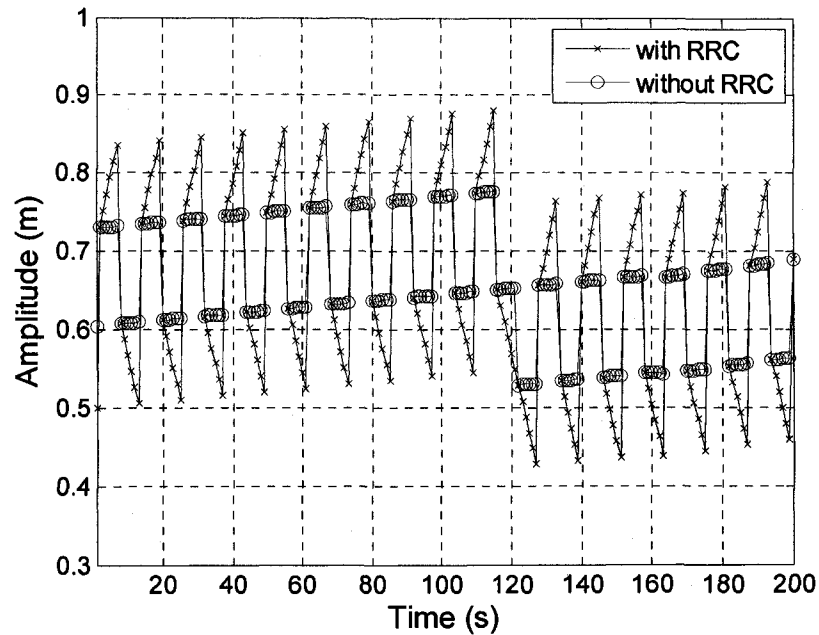


Figure 3.1: Fast clock correction with and without the RRC

3.4 Results

The proposed methods are tested on the static data taken at Stanford University on September 6, 2006. The effect of the new weighting matrix will be presented first. Then, accuracy and stability improvements for WAAS based on the proposed three methods will be shown.

3.4.1 Effect of New Weighting Matrix

Figure 3.2 and 3.3 compare the position errors in East and Up from the standard WAAS and the optimized WAAS with a new weighting matrix. Figure 3.4 and 3.5 show the total variances for the standard WAAS and the optimized WAAS. There are significant positioning improvements when the time is near 40-50 minutes and around 100 minutes. The position from the optimized WAAS with the new weighting matrix shows better stability around these times. The variances in Figure 3.4 and 3.5 explain why the new weighting matrix results in better stability. Two of the total variances in Figure 3.4 are much larger than the rest of the variances near the 40-50 minutes interval. One of the variances is also much larger than the rest near 100 minutes. The satellites with these large variances are heavily de-weighted such that they are effectively excluded in computing position. On the other hand, the new total variances in Figure 3.5 show that the difference of these variances is not as extreme as the WAAS variances in Figure 3.4. Therefore, the satellites that have larger variances are relatively less de-weighted than the standard WAAS, and they help to obtain better position solutions.

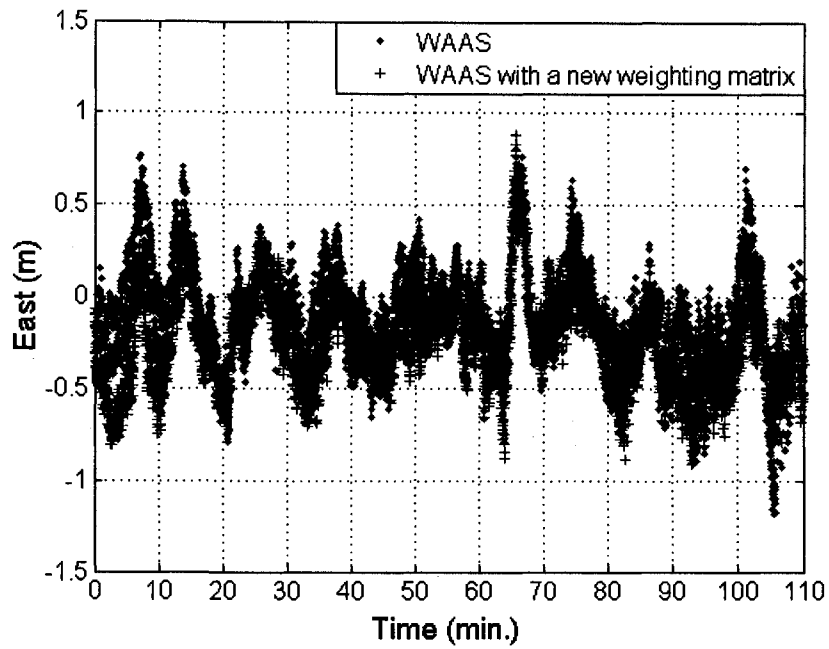


Figure 3.2: Comparison of the position errors in East from the standard WAAS and the WAAS with a new weighting matrix

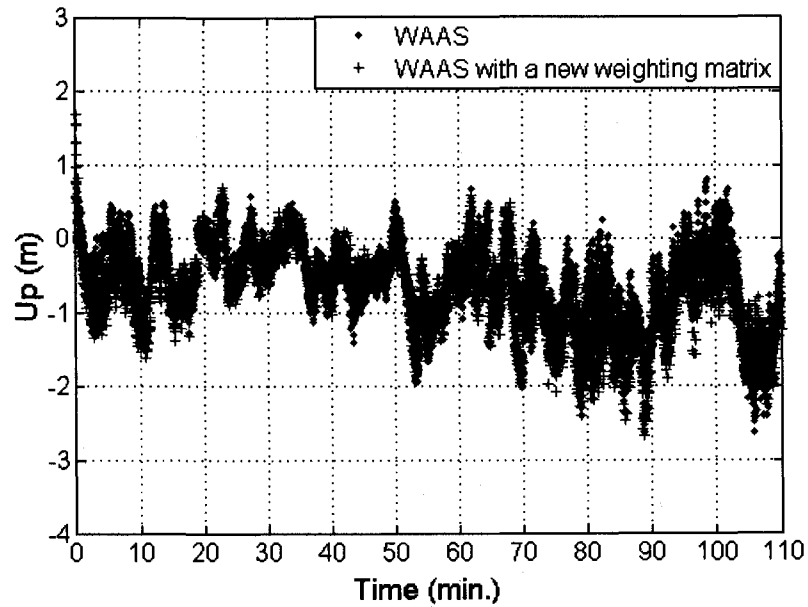


Figure 3.3: Comparison of the position errors in Up from the standard WAAS and the WAAS with a new weighting matrix

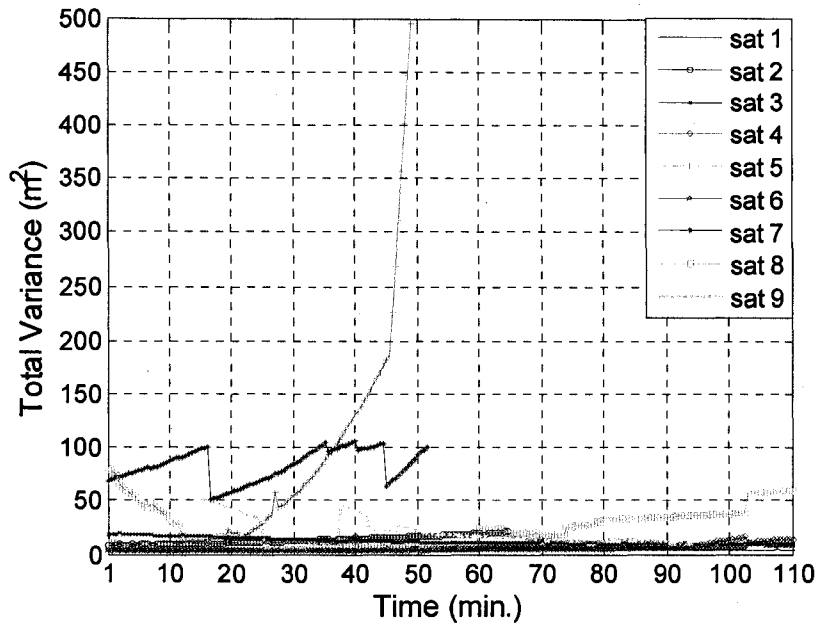


Figure 3.4: Total variances of the observed satellites in the above tests from the standard WAAS

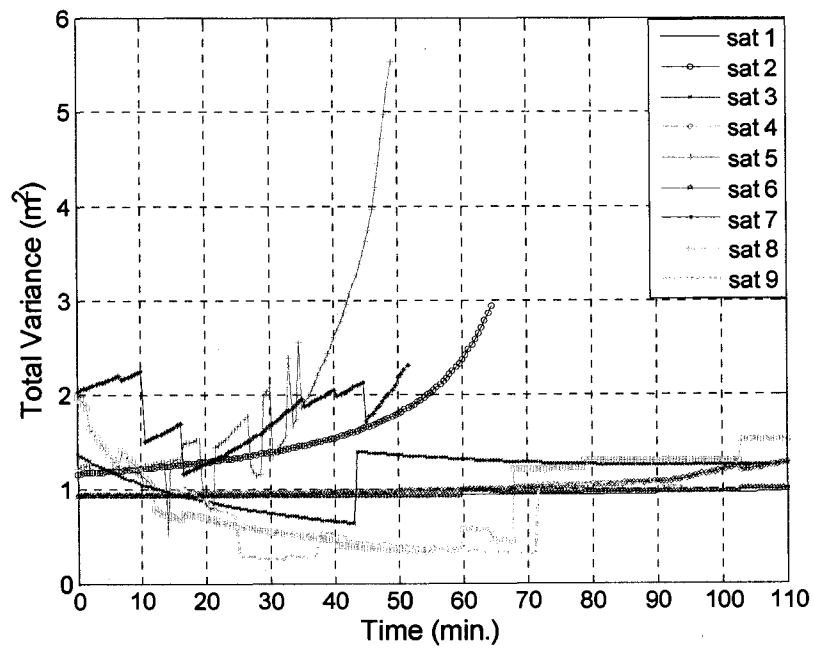


Figure 3.5: Total variances of the observed satellites in the above tests from the optimized WAAS

3.4.2 Overall Improvements using the Three Methods

Figure 3.6 and 3.7 compare the position errors from the standard WAAS and optimized WAAS. For adaptive carrier smoothing, a 1000 second window of code minus carrier measurements is used. The two plots show that the optimized WAAS with adaptive carrier smoothing has smoother and more stable position solutions than the standard WAAS.

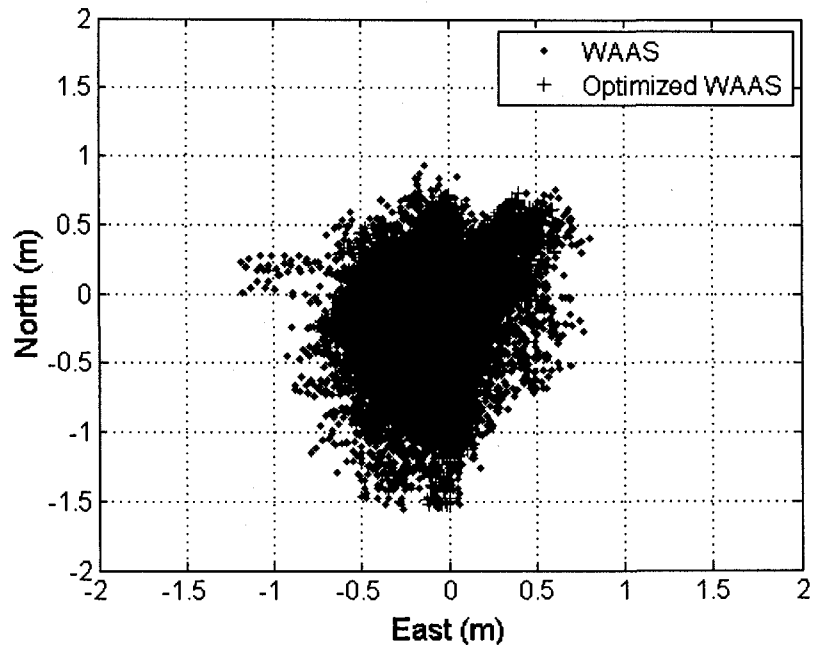


Figure 3.6: Comparison of the horizontal errors from the standard WAAS and the optimized WAAS

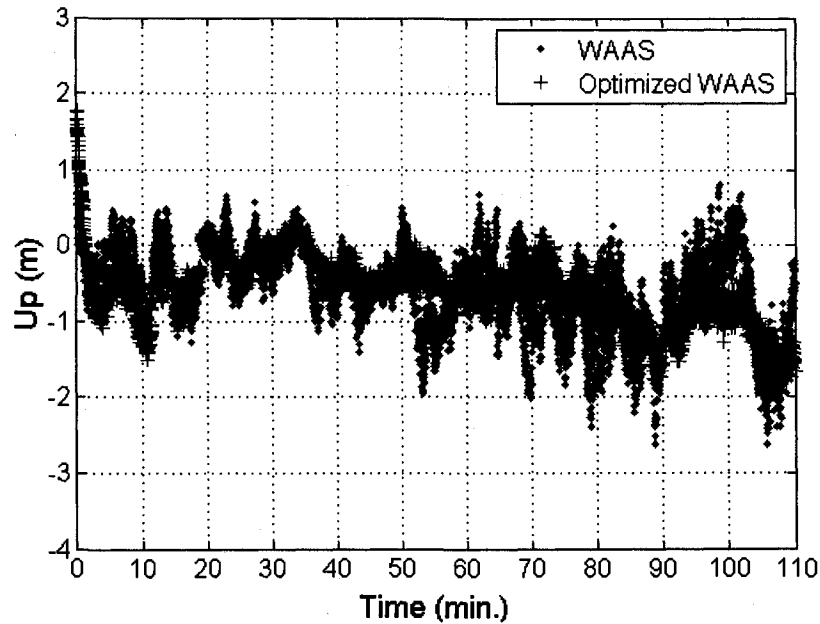


Figure 3.7: Comparison of the vertical errors from the standard WAAS and the optimized WAAS

3.5 Conclusion

In this chapter, the schemes of optimizing WAAS for accuracy and stability are explored. The proposed schemes include the formulation of the realistic weighting matrix for accuracy, the termination of the Range Rate Correction (RRC), and the usage of adaptive carrier smoothing. To see the sole effects of the new weighting matrix, the position solutions with the WAAS weighting matrix and the new weighting matrix are compared. The position using the new weighting matrix shows better stability especially when some satellites have 50-100 times larger variances than the others. The termination of the RRC reduced the amplitude of 12 second periodic noise to better than 0.125 meters in the range domain. The net results also confirm that the proposed three methods improve WAAS position noise and stability by approximately 16%. These methods have not been previously reported in the literature. These methods are applied to the algorithms developed in Chapter 6.

Chapter 4

Reference Point-Based Relative Positioning Methods with a Single Frequency Receiver

4.1 Introduction

Precise positioning using GPS is one of the most active research areas in the community of navigation because there are many applications requiring a high level of accuracy in position. The applications include automatic aircraft landing, attitude determination, and autonomous control of land vehicles, to name a few. Extensive studies on precise positioning driven by commercial and academic interests have resulted in successful methods and products.

One of the popular methods is Real-Time Kinematic (RTK) survey [Manadhar]. RTK survey requires two or more receivers to cancel out the common errors between them. Therefore, an RTK system typically has a reference receiver, whose location is known, and one or more rover receivers. This system uses carrier phase measurements

as ranging sources instead of code phase measurements. Therefore, an RTK system has a sophisticated integer ambiguity resolution algorithm in order to use carrier phase measurements as ranging sources. There are many ways of implementing the integer ambiguity resolution. The robustness and effectiveness of those algorithms are important factors for the performance of a product [Yang]. With the help of error corrections from a reference receiver and the use of carrier phase measurements as ranging sources, current RTK systems usually achieve a centimeter level of accuracy. In addition to high accuracy, some RTK systems have the capability of an instant integer resolution and of effectively handling cycle-slips [Kim03], which provides robustness in various situations. Due to these advantages, RTK systems are widely used in many applications.

Another method is Precise Point Positioning (PPP) using a dual frequency receiver [Gao]. Unlike RTK, PPP depends on external sources like the international GPS service (IGS) in order to mitigate the ephemeris and satellite clock in code or carrier phase measurements. Due to these error corrections from the external sources, PPP does not require multiple receivers but needs a dual frequency receiver for accurate integer ambiguity resolutions and correction of ionospheric errors. Using one receiver permits more flexible operations than RTK. However, latency or post processing is inevitable since the external sources are not available in real-time. PPP usually provides a decimeter to centimeter level of accuracy in position. More recently, PPP using a dual frequency receiver with WAAS corrections has been proposed by [Rho]. This technique is in the early stage of research but is expected to be used in real-time with a decimeter level of accuracy.

Although these techniques can provide a high level of accuracy, it is not desirable to use them in some applications, such as in flight inspection, because of the cumbersome set-up procedure of an RTK system and the large initialization time required in the conventional PPP. The reference point-based Precise Relative Positioning (PRP) methods introduced in this chapter can fill these gaps. These methods use a single frequency receiver and can provide decimeter level or better accuracy. Also, they do not require any initializing time but instead use a known

position of a receiver at one time during navigation as a reference point. The reference point-based PRP has two modes. One is Iono-Free PRP (I-F PRP) [Kim061], and the other is Time-Differenced PRP (T-D PRP) [Kim072]. Iono-Free PRP uses the difference of the sum of code and carrier phase measurements over a time interval as ranging sources to generate relative position. This formulation cancels out ionospheric delays and reduces multipath by roughly a factor of two. Therefore, the I-F PRP provides stable relative position solutions in real-time with reduced multipath noise. On the other hand, T-D PRP generates precise relative positions by using the difference of carrier phase measurements at two epochs, which is called the delta pseudorange. The T-D PRP eliminates differential ionospheric delay by using code-carrier divergence in near real-time from the same technique described in Section 2.3. Therefore, the T-D PRP provides very precise relative position in near-real-time without ionospheric effects. The overall accuracy of those reference point-based relative positions entirely depends on the accuracy of the reference position.

This chapter is organized as follows. Section 4.2 discusses the derivation of the I-F PRP and shows positioning performance. Section 4.3 presents the derivation of the T-D PRP and shows positioning performance. Lastly, the conclusion follows in Section 4.4.

4.2 Iono-Free Precise Relative Positioning (I-F PRP)

The GPS code phase measurements (ρ) and carrier phase measurements (Φ) are described without specifying a specific satellite as follows

$$\begin{aligned}\rho &= r + I + T + c(\delta t_u - \delta t_s) + \varepsilon_\rho \\ \Phi &= r - I + T + c(\delta t_u - \delta t_s) + \lambda N + \varepsilon_\Phi\end{aligned}\tag{4.1}$$

where r is the geometric range between a user and a satellite, I and T are the ionospheric delays and the tropospheric delays, respectively, in the range measurements, δt_u is the receiver clock error, and δt_s is the satellite clock error. ε_ρ

and ε_ϕ denote the modeling error, multipath, and unmodeled effects in code and carrier phase measurements, respectively. λ is the carrier wavelength on L1, and N is the integer ambiguity on L1 of a satellite.

Summing the halves of the code and carrier measurements cancels ionospheric delays but introduces a bias with reduced noise as follows.

$$\begin{aligned} y &= \frac{1}{2}\rho + \frac{1}{2}\Phi \\ &= r + T + c(\delta t_u - \delta t_s) + \frac{1}{2}\lambda N + \frac{1}{2}\varepsilon_\rho + \frac{1}{2}\varepsilon_\phi \end{aligned} \quad (4.2)$$

The tropospheric delays can be compensated for using the current high fidelity troposphere models [WAASMOPS]. Satellite clock error corrections can be computed by using GPS ephemeris data or WAAS corrections. With these error corrections, Equation (4.2) becomes

$$\hat{y} = r + c\delta t_u + \frac{1}{2}\lambda N + \frac{1}{2}\varepsilon_\rho + \frac{1}{2}\varepsilon_\phi + \varepsilon_T + \varepsilon_{\delta t_s} \quad (4.3)$$

where ε_T and $\varepsilon_{\delta t_s}$ are the tropospheric delays and the satellite clock error residual corrections, respectively.

At this point, let us designate the position of a reference point as p_{ref} . The position of a user at any time can be described as the sum of the position of the reference point and the relative position to the reference point, δp , as follows.

$$p_{user} = p_{ref} + \delta p \quad (4.4)$$

where p_{user} is the position of a user.

The geometric range between the reference point and a satellite, r_R , can be easily computed using the GPS navigation messages. Assuming a short baseline between the current receiver position and the reference point, the difference of the geometric

ranges from the current receiver and the reference point to a satellite can be described by [EngeMisra],

$$r - r_R = -1 \cdot \delta p \quad (4.5)$$

where $1^{(k)}$ is the line of sight vector to the satellite from the reference point, r is the geometric range between the current receiver and the satellite, and r_R is the geometric range between the reference point and the satellite. This situation is illustrated in Figure 4.1.

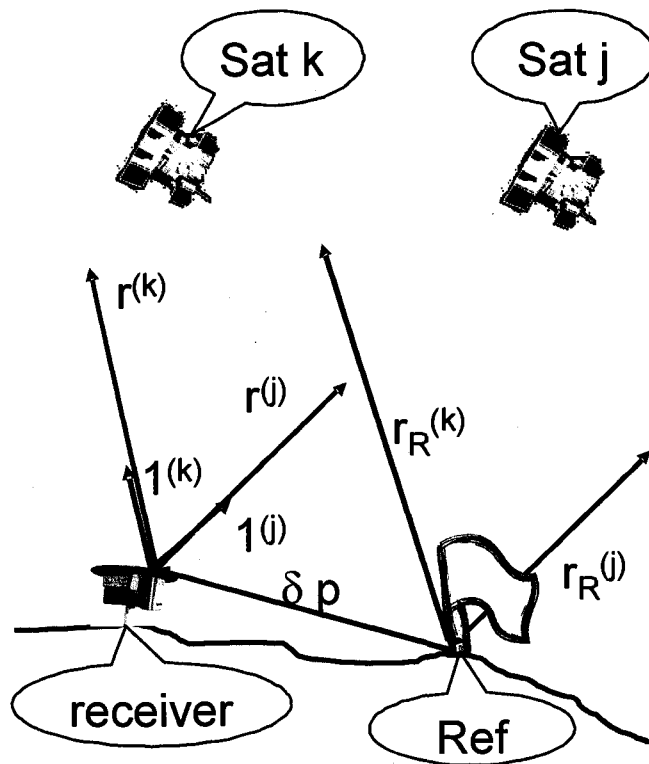


Figure 4.1: Geometry of a receiver and a reference point with a short baseline

Then, subtracting r_R from Equation (4.3) yields

$$\tilde{y} = -1 \cdot \delta p + c \delta t_u + \frac{1}{2} \lambda N + \frac{1}{2} \varepsilon_\rho + \frac{1}{2} \varepsilon_\Phi + \varepsilon_T + \varepsilon_{\delta t_s} \quad (4.6)$$

Now specifying j and k satellites, the receiver clock error cancels out as follows:

$$\begin{aligned} \tilde{y}^{(k,j)} &= \tilde{y}^{(k)} - \tilde{y}^{(j)} \\ &= (-1^{(k)} + 1^{(j)}) \cdot \delta p + \frac{1}{2} \lambda N^{(k,j)} + \frac{1}{2} \varepsilon_\rho^{(k,j)} + \frac{1}{2} \varepsilon_\Phi^{(k,j)} + \varepsilon_T^{(k,j)} + \varepsilon_{\delta t_s}^{(k,j)} \end{aligned} \quad (4.7)$$

where $(\cdot)^{(k,j)}$ denotes $(\cdot)^{(k)} - (\cdot)^{(j)}$.

There are two unknowns, δp and $N^{(k,j)}$, in Equation (4.7) apart from the error terms. Since it is assumed that δp is known at one time during navigation, it is possible to approximately evaluate $N^{(k,j)}$ at that particular time. Let us denote the estimated relative position, from using other sensors or the initial setting, to the reference point as $\delta \hat{p}_s$ again at the particular time. Then, the integer ambiguity terms can be approximated as

$$\begin{aligned} \frac{1}{2} \lambda \hat{N}^{(k,j)} &= \tilde{y}^{(k,j)} - (-1^{(k)} + 1^{(j)}) \cdot \delta \hat{p}_s \\ &= (-1^{(k)} + 1^{(j)}) \cdot b_p + \frac{1}{2} \lambda N^{(k,j)} + \frac{1}{2} \varepsilon_\rho^{(k,j)} + \frac{1}{2} \varepsilon_\Phi^{(k,j)} + \varepsilon_T^{(k,j)} + \varepsilon_{\delta t_s}^{(k,j)} \end{aligned} \quad (4.8)$$

where $b_p = \delta \hat{p}_s - \delta p$, and b_p is the possible error in $\delta \hat{p}_s$. $\hat{N}^{(k,j)}$ is the estimated integer ambiguity terms. $\hat{N}^{(k,j)}$ has an offset because of b_p and the noise terms. Therefore, $\frac{1}{2} \lambda \hat{N}^{(k,j)}$ can be described as

$$\frac{1}{2} \lambda \hat{N}^{(k,j)} = \frac{1}{2} \lambda N^{(k,j)} + b_{N^{(k,j)}} \quad (4.9)$$

where $b_{N^{(k,j)}}$, the bias error in the integer ambiguity, is

$$b_{N^{(k,j)}} = -(-1^{(k)} + 1^{(j)}) \cdot b_p + \frac{1}{2} \varepsilon_{\rho}^{(k,j)} + \frac{1}{2} \varepsilon_{\Phi}^{(k,j)} + \varepsilon_T^{(k,j)} + \varepsilon_{\delta t_s}^{(k,j)}$$

Now, it is possible to solve for δp at time t by subtracting $\frac{1}{2} \lambda \hat{N}^{(k,j)}$ from Equation (4.8) as follows:

$$\tilde{y}_t^{(k,j)} - \frac{1}{2} \lambda \hat{N}_0^{(k,j)} = (-1_t^{(k)} + 1_t^{(j)}) \cdot \delta p_t + \varepsilon_t^{(k,j)} \quad (4.10)$$

where

$$\varepsilon_t^{(k,j)} = \frac{1}{2} \varepsilon_{\rho,t}^{(k,j)} + \frac{1}{2} \varepsilon_{\Phi,t}^{(k,j)} + \varepsilon_{T,t}^{(k,j)} + \varepsilon_{\delta t_s,t}^{(k,j)} - b_{N^{(k,j),0}}$$

Note that the bias error in the estimated integer term is generated at time zero.

Now, it is easy to construct a system of linear equations by implementing the same procedures for the other satellites in order to solve for δp in the least squares sense. The set of linear equations is

$$\underbrace{\begin{bmatrix} \tilde{y}_t^{(1,j)} - \frac{1}{2} \lambda \hat{N}^{(1,j)} \\ \tilde{y}_t^{(2,j)} - \frac{1}{2} \lambda \hat{N}^{(2,j)} \\ \vdots \\ \tilde{y}_t^{(k,j)} - \frac{1}{2} \lambda \hat{N}^{(k,j)} \end{bmatrix}}_{Y(t)} = \underbrace{\begin{bmatrix} -1^{(1)} + 1^{(j)} \\ -1^{(2)} + 1^{(j)} \\ \vdots \\ -1^{(k)} + 1^{(j)} \end{bmatrix}}_{H(t)} \delta p_t + \underbrace{\begin{bmatrix} \varepsilon_t^{(1,j)} \\ \varepsilon_t^{(2,j)} \\ \vdots \\ \varepsilon_t^{(k,j)} \end{bmatrix}}_{\varepsilon(t)} \quad (4.11)$$

There is no combination of the same satellite, such as $(\bullet)^{(j,j)}$.

Various weighting matrices can also be constructed for Equation (4.11). Then, the relative position with respect to the reference point can be estimated with weighted least squares as follows:

$$\delta \hat{p}(t) = \left(H^T(t) W(t) H(t) \right)^{-1} H^T(t) W(t) Y(t) \quad (4.12)$$

The overall error characteristics of the I-F PRP depend on $\varepsilon(t)$. In $\varepsilon(t)$, the bias and the residual correction errors are strongly correlated over time. Therefore, the positioning errors are small in the beginning and get larger until the correlation becomes weak. These error characteristics will be shown in the results.

When a user wants to further reduce multipath and receiver noise, he/she can use smoothed pseudorange in this formulation by using a Hatch filter or Adaptive Carrier Smoothing (ACS). Even a small smoothing window may effectively reduce the noise because the noise term will be further reduced roughly by a factor of two. However, the cancellation of ionospheric effects will not be exact because the ionospheric induced delay will be introduced from the filters.

4.2.1 Satellite Constellation Changes and cycle-slips in the I-F PRP

It is possible that a new satellite comes into view after the resolution of the difference integer terms, $N^{(k,j)}$, at the initial time. At this time, the accurate relative position from a receiver to the reference point may not be available. One possible option to deal with a new satellite is to use $\delta \hat{p}$ instead of $\delta \hat{p}_0$, in order to obtain a new $N^{(k,j)}$. The effect of using $\delta \hat{p}$ is that the new $N^{(k,j)}$ is more likely to have a larger bias than other differenced integer terms. It also may cause a sudden jump in the position domain, which is not desirable for the purpose of precise positioning. One trick to avoid the sudden jump is to compute positions with and without a new satellite at this particular epoch. The difference between the two position solutions is defined to be a calibration factor. The position solution with the new satellite in the future will be calibrated to the calibration factor. It is also possible that a satellite disappears during the navigation period. Usually, a sudden jump in position domain is also observed when a satellite disappears. What needs to be done in this case is to recompute the position at the previous epoch with and without the lost satellites and compute the calibration factor. Then, the calibration factor will be applied to the future position solutions. Another possible situation is a cycle-slip. A cycle-slipped satellite

can be treated like a satellite that disappears and comes back immediately. It should be noted that this simple calibration technique is particularly useful for a short time operation because the jump acts like a bias in short time. For the comparisons in the next section, “calibrated GPS” refers to the procedure described here.

4.2.2 The Performance of I-F PRP for One Hour Operation Time

The I-F PRP was tested with static GPS receiver data. The data was taken at Stanford University on March 3, 2005. The reference point is set to be the position of the antenna whose position is accurately (better than a few centimeters) surveyed. The sampling rate of the data was 1 second, and 20 seconds of carrier-smoothing is used for the I-F PRP. The horizontal and vertical position error from the I-F PRP using stand-alone GPS and the calibrated stand-alone GPS are shown in Figure 4.2 and 4.3. The 11 data sets of one hour operation of the I-F PRP and the calibrated stand-alone GPS are plotted together to compare the stability of the positions. The number of satellites is shown in Figure 4.4, and no cycle-slip is observed in the given set of data.

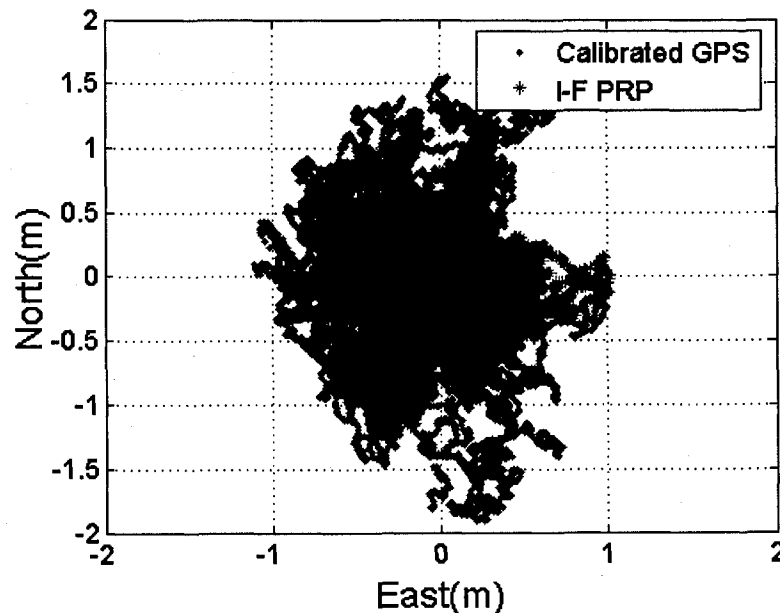


Figure 4.2: Horizontal Error in 11 data sets for 1 hour of operation

The RMS of the position errors of the I-F PRP and the calibrated GPS are compared in Figure 4.5 and 4.6. These statistics clearly show that the I-F PRP has much better position stability.

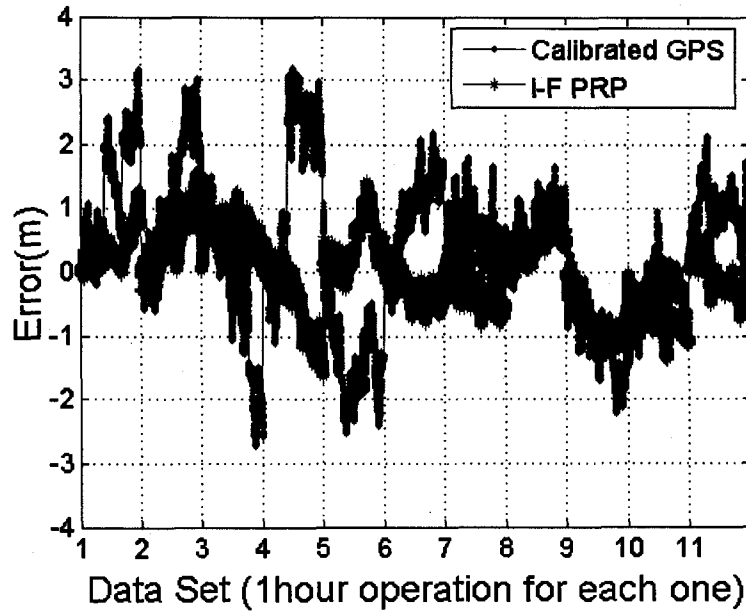


Figure 4.3: Vertical Error in 11 data sets for one hour of operation

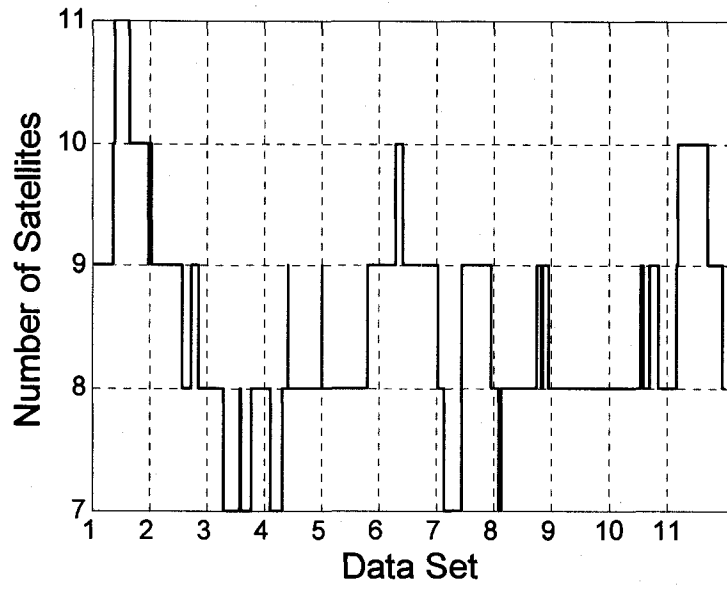


Figure 4.4: The number of satellites in 11 data sets for one hour of operation

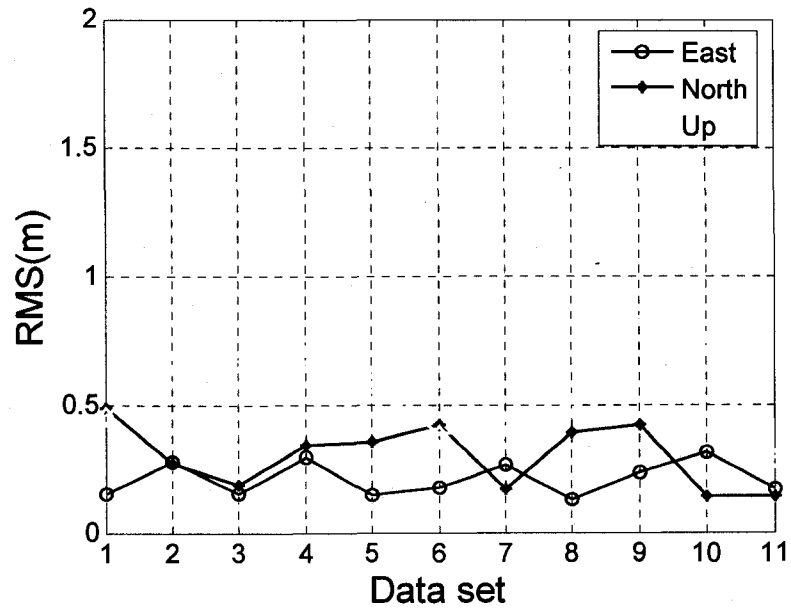


Figure 4.5: RMS of I-F PRP in 11 data sets for one hour of operation

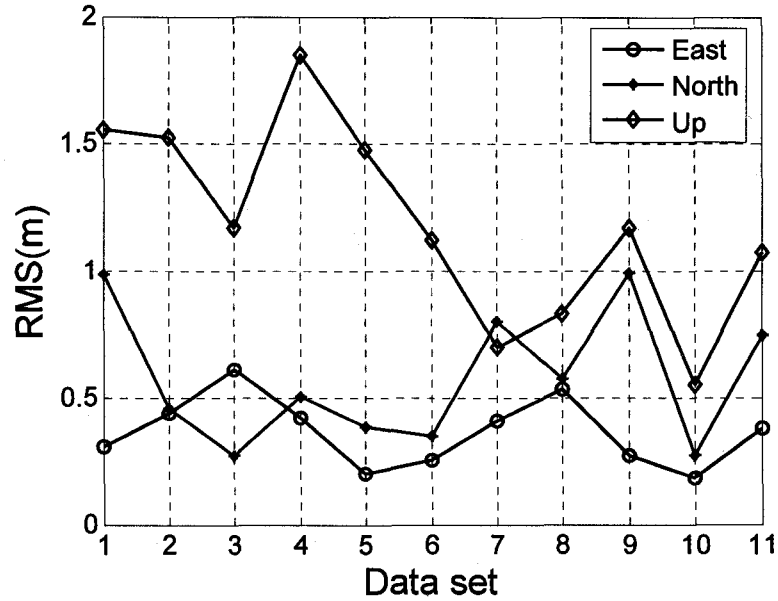


Figure 4.6: RMS of stand-alone GPS in 11 data sets for one hour of operation

4.3 Time-Differenced Precise Relative Positioning (T-D PRP)

Relative positioning utilizing only carrier measurements is also possible with a single frequency receiver by using the difference of carrier phase measurements over a time interval, called delta pseudorange. In this case, relative position is defined to be the distance between the position at the current epoch and the initial positioning point or a reference position.

The delta pseudorange of a satellite at two epochs, t and 0 , is described as follows:

$$\Phi_t - \Phi_0 = r_t - r_0 + c\Delta\delta t_u - c\Delta\delta t_s - \Delta I_{t_0} + \Delta T_{t_0} + \Delta\varepsilon_{\Phi,t_0} \quad (4.13)$$

where $\Delta(\bullet)$ is the difference of the same variable at the two epochs. The nice property of the delta pseudorange is that precise carrier measurement is available without a troublesome integer ambiguity. Researchers previously proposed to use the delta pseudorange for velocity estimation [VanGraas] and relative positioning [Somerville].

The T-D PRP introduced in this chapter also uses the delta pseudorange. Unlike the previous research, T-D PRP eliminates a differential ionospheric delay by using code-carrier divergence in near-real-time using the technique described in Section 2.3, assuming that near-real-time processing is allowed. In the previous research, the ionospheric effects are removed by a dual frequency receiver.

The formulation of the T-D PRP is introduced in [Kim072] and repeated in this section. Now, let us apply satellite clock error corrections and tropospheric error corrections to Equation (4.13). Then, linearizing it with respect to a reference position and adding a short base line assumption, Equation (4.13) becomes

$$\begin{aligned} y_{t_0} &= r_t - r_0 - (r_{R,t} - r_{R,0}) + c\Delta\delta t_u - \Delta I_{t_0} + \Delta\epsilon_{\Phi,t_0} + \epsilon_{T,t_0} + \epsilon_{\delta t_s,t_0} \\ &= -1_t \cdot \delta p_{t_0} + c\Delta\delta t_u - (-1_t + 1_0) \cdot b_p - \Delta I_{t_0} + \Delta\epsilon_{\Phi,t_0} + \epsilon_{T,t_0} + \epsilon_{\delta t_s,t_0} \end{aligned} \quad (4.14)$$

where δp_{t_0} is a relative position of a receiver at time t from the position at time 0. Again, b_p is an error caused by the imperfect knowledge of the reference position at time 0. ϵ_{T,t_0} includes tropospheric delay correction residual errors at time t and 0. $\epsilon_{\delta t_s,t_0}$ includes satellite clock error correction residual errors at time t and 0.

Next, ΔI_{t_0} is removed by using the difference of L1 code and carrier phase measurements using the technique in Section 2.3. Taking the estimated ionospheric delay gradient, $\hat{\beta}_1$, the correction for the differential ionospheric delay gradient between the time t and 0 can be generated as follows:

$$\Delta \hat{I}_{t_0} = t \cdot \hat{\beta}_1 \quad (4.15)$$

$\Delta \hat{I}_{t,0}$ will be very effective when the ionosphere is active and minimal when the ionosphere is steady. However, even in the regions that have quiet ionosphere, $\Delta \hat{I}_{t,0}$ is indispensable because it is always possible that an unexpected sharp ionospheric gradient may arise.

Finally, a set of linear equations can be formed as follows:

$$\underbrace{\begin{bmatrix} y_{t,0}^1 \\ y_{t,0}^2 \\ \vdots \\ y_{t,0}^n \end{bmatrix}}_Y = \underbrace{\begin{bmatrix} -1^1 & 1 \\ -1^2 & 1 \\ \vdots \\ -1^k & 1 \end{bmatrix}}_G \underbrace{\begin{bmatrix} \delta p_{t,0} \\ C \Delta t_u \end{bmatrix}}_X + \underbrace{\begin{bmatrix} \hat{\varepsilon}_{t,0}^1 \\ \hat{\varepsilon}_{t,0}^2 \\ \vdots \\ \hat{\varepsilon}_{t,0}^k \end{bmatrix}}_{\hat{\varepsilon}} \quad (4.16)$$

$$Y = GX + \hat{\varepsilon}$$

where $\hat{\varepsilon}$ includes b_p , $\Delta \varepsilon_{\phi,t,0}$, and all residual errors.

Then, the relative position from T-D PRP with respect to the reference position is computed using weighted least squares as follows:

$$X = (G^T W^{-1} G)^{-1} G^T W^{-1} Y \quad (4.17)$$

where W is a weighting matrix. It is difficult to find an optimal W because some of the errors in Y are highly correlated over time. However, since the overall errors are dependent on satellite elevation angle, a reasonable choice for the elements of W would be functions of the satellite elevation angle.

The error characteristic of the T-D PRP is that the position errors are very small in the beginning and become larger over time. The main reason for this is that the residual correction errors of satellite clock-ephemeris errors and tropospheric delay errors have strong temporal correlation [Ibrahim][Walter99]. Therefore, when the T-D PRP takes the difference of the error corrected carrier measurements, most of the residual correction errors are effectively cancelled out in the beginning. However, as time goes by, the errors become larger due to the decorrelation of those residual errors.

4.3.1 The Performance of T-D PRP

Figure 4.7, 4.8, and 4.9 compare the relative position errors from implementing the T-D PRP with and without compensating for the differential ionospheric delays using static experimental receiver data in East, North, and Up, respectively. The measurements were taken on September 5, 2005 at Stanford University, and the position of the receiver antenna is surveyed with accuracy of within a few centimeters. Each test is implemented for 900 seconds.

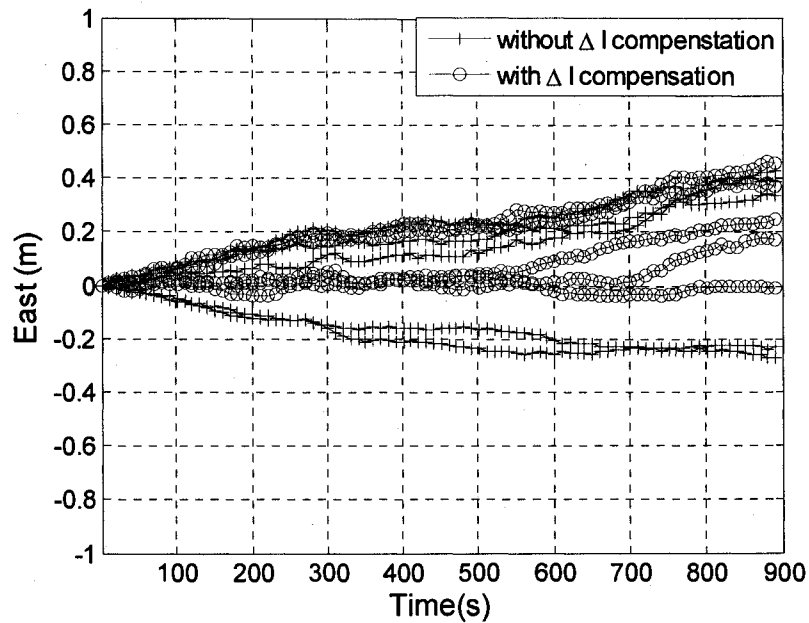


Figure 4.7: T-D PRP errors in East with and without the differential ionospheric corrections

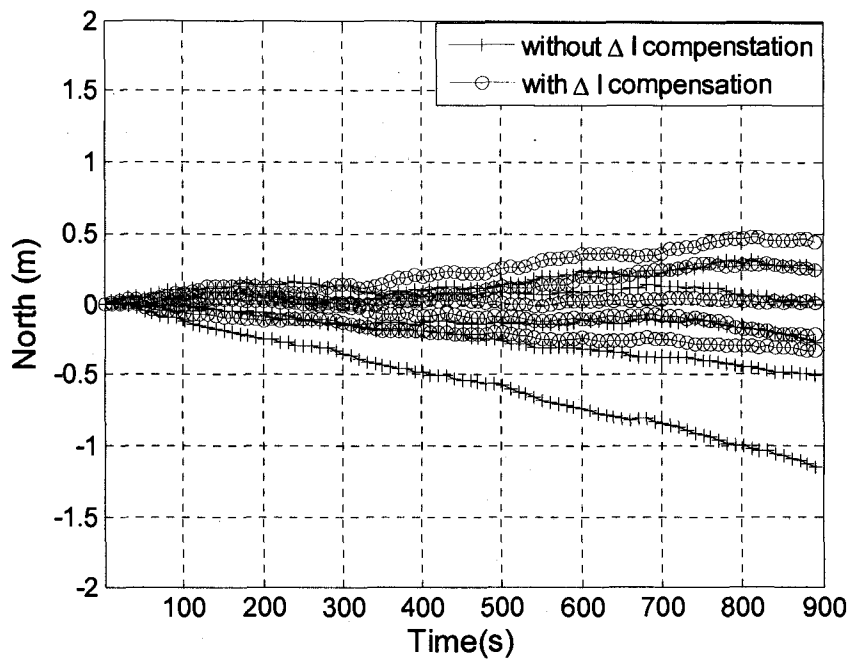


Figure 4.8: T-D PRP errors in North with and without the differential ionospheric corrections

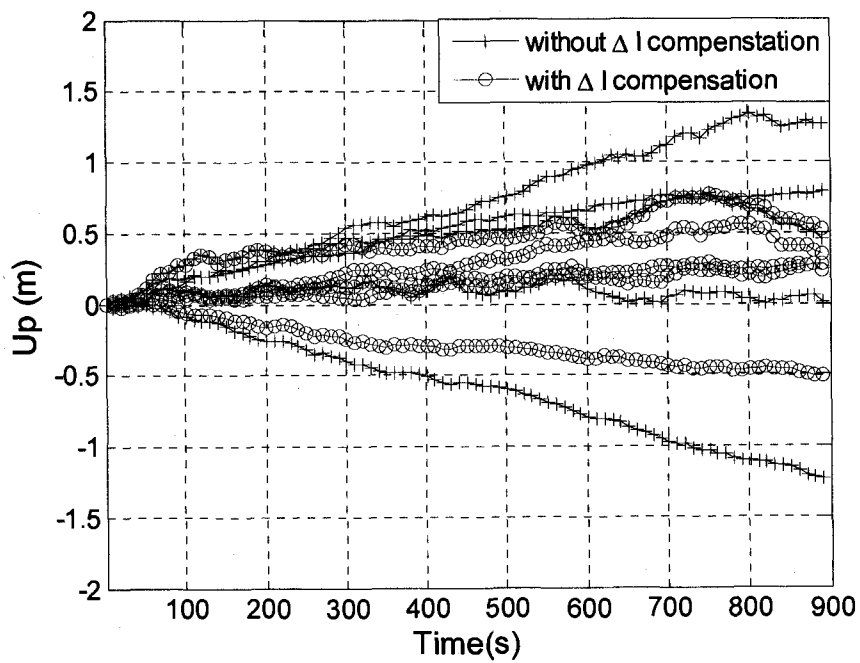


Figure 4.9: T-D PRP errors in Up with and without the differential ionospheric corrections

These results show that the T-D PRP errors with and without the differential ionospheric delay correction are very close in the beginning. But, as time increases, the T-D PRP errors with the differential ionospheric correction are more centered around zero. This fact is also supported by the RMS of the errors of the two cases at the end of the operation, 900 seconds, in Figure 4.10.

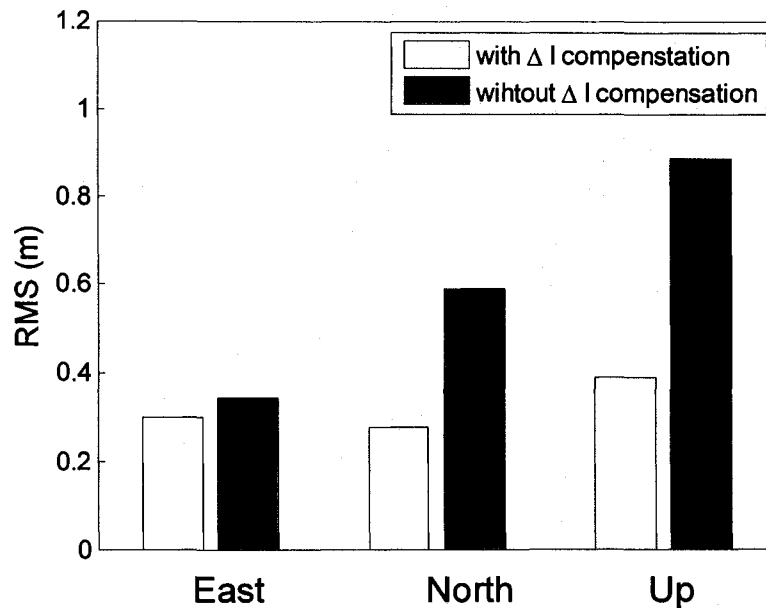


Figure 4.10: RMS comparison of the T-D PRP with and without the differential ionospheric delay correction at 900 seconds

4.4 Conclusion

In this chapter, two precise relative positioning methods, I-F PRP and T-D PRP, using a single frequency receiver are introduced. The I-F PRP used the sum of code and carrier phase measurement as range sources. The benefit of this combination was that ionospheric delays were completely removed and multipath was reduced by a factor of two. The T-D PRP used the difference of carrier phase measurements over a

time interval as range sources to obtain very precise relative position. In this method, differential ionospheric delays were removed by fitting a first order linear regression on the time series of code minus carrier phase measurements. Therefore, the differential ionospheric cancellation was performed in near-real-time. The I-F PRP and T-D PRP were tested using data collected from a static GPS receiver, whose position was accurately surveyed. The test results showed that the I-F PRP and T-D PRP both provided more stable position than stand-alone GPS. The I-F PRP provided better than 50 cm RMS in the horizontal and 1 m RMS in the vertical for one hour of operation time. The T-D PRP provided very accurate position in the beginning, and its error grew as time increased. The error was less than 50 cm error in the horizontal and 80 cm in the vertical for 900 seconds operation time.

It should be noted that the T-D PRP is constrained to be only operational in post-processing (near-real-time) because of its near-real-time cancellation of differential ionospheric delays. The I-F PRP can serve real-time applications. It should also be noted that the shorter the operation time, the better the performance these algorithms can provide. The reason for this is that the measurements of the reference point at the initial time are only usable as long as the corresponding satellites used for the measurements are in view. The T-D PRP method is used in the algorithms developed in Chapter 6 and 7.

PART II

***Flight Inspection System Designs and
Performance***

Chapter 5

WAAS-aided Flight Inspection System

5.1 Introduction

The WAAS-aided Flight Inspection System (FIS) is introduced in this chapter and also in [Kim062]. This system has a single frequency Commercial off-the-shelf (COTS) certified WAAS receiver, an INS, a radar altimeter, and a TeleVision Positioning System (TVPS). This system fuses the WAAS position with an INS to remove the WAAS periodic noise and uses the radar altimeter and TVPS readings over the runway threshold to eliminate a WAAS position bias during approach. By doing this, WAAS position solutions can be improved for use in flight inspection. Since the INS is used as a complementary sensor that only removes the noise in the WAAS position, the WAAS-aided FIS can utilize a low-grade INS (tactical or less). Therefore, although the WAAS-aided FIS is similar to the Inertial-based AFIS in terms of its hardware, it can achieve significantly lower costs than the Inertial-based AFIS because it can tolerate a lower quality INS. In addition, since the WAAS-aided FIS only requires the normal position outputs from a COTS certified WAAS receiver,

it can be easily realized from the Inertial-based AFIS due to the similarity of the two systems.

This chapter is organized as follows. The airborne WAAS error characteristic in the position domain is discussed in Section 5.2. Then, the WAAS-aided FIS system architecture is discussed in Section 5.3. In this section, the fusion algorithm of the WAAS and an INS are described in detail. Section 5.4 presents the test results of the WAAS-aided FIS with flight test data. In the results, the feasibility study of using a lower grade INS will be shown. The conclusion follows in Section 5.5.

5.2 WAAS Airborne Error Characteristics

Figure 5.1 shows the WAAS position errors obtained from flight tests taken on April 4, 2005. This figure shows the typical WAAS airborne error characteristics, which can be described as the sum of a bias and an additive noise for a short time period. The bias could jump slightly if a satellite constellation changes and a new WAAS ionosphere correction message arrives. The noise is comprised of many factors such as multipath, thermal noise, and WAAS correction residuals.

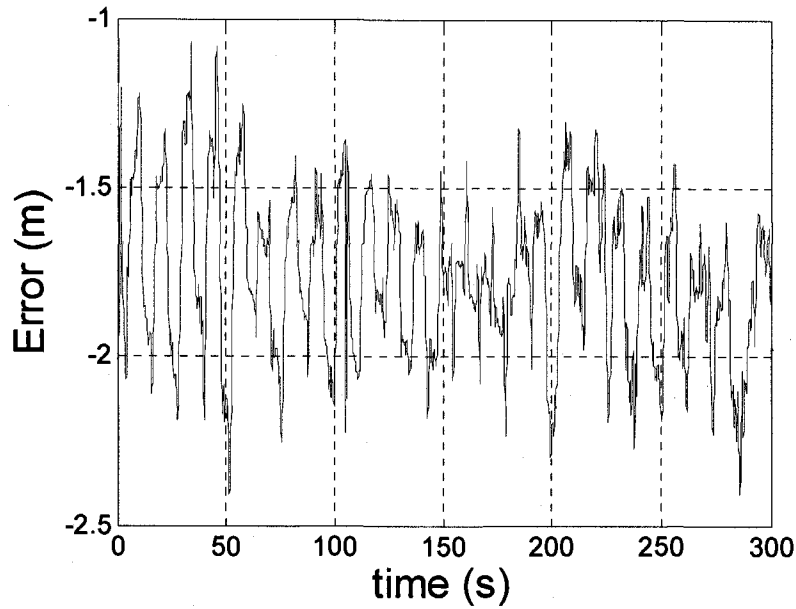


Figure 5.1: Example of WAAS airborne position errors

Figure 5.2 shows the power spectral density of the noise obtained from subtracting the mean of the error in Figure 5.1. It is interesting to see the distinct peak in the noise. The periodic noise has a 12 second period and is caused by both the WAAS fast clock correction (Message Types 2-5) and the range rate correction [WAASMOPS] as discussed in Section 3.3. The broadcast correction message has 0.125 m resolution and is updated every 6 seconds. The range rate correction, RRC, is computed by a user as follows:

$$RRC(t_{of}) = \frac{PRC_{current} - PRC_{previous}}{\Delta t} \quad (5.1)$$

where PRC is the fast clock corrections and t_{of} is the time of applicability. Δt is the time difference between $PRC_{current}$ and $PRC_{previous}$. The combination of the WAAS fast clock correction message and the RRC causes the cyclic noise whose amplitude is typically over 0.15 meters as shown in Figure 5.3.

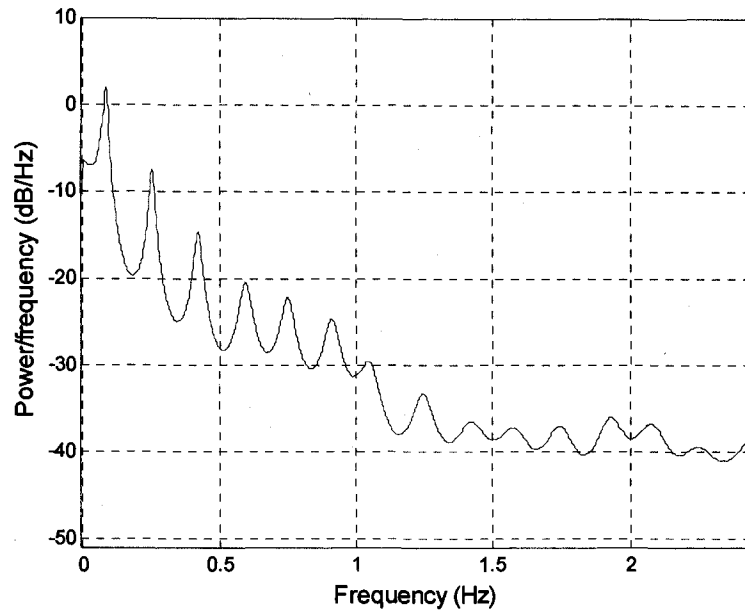


Figure 5.2: Power spectral density of WAAS airborne noise shown in Figure 5.1

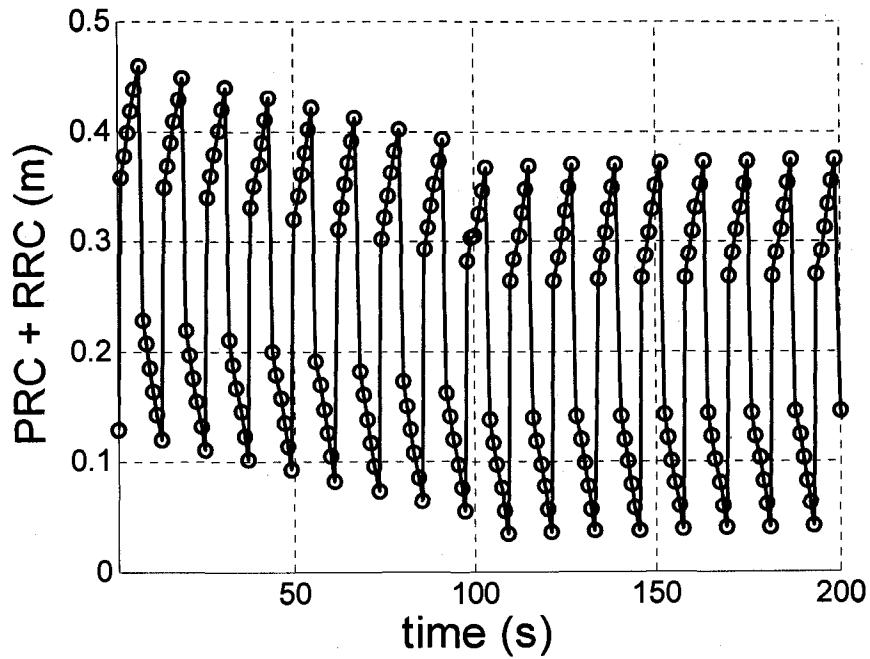


Figure 5.3: Example of WAAS fast clock correction

By identifying WAAS airborne error characteristics, it becomes clear how to improve the WAAS position solutions during flight inspection for ILS calibration; the cyclic noise and WAAS bias must be eliminated. The next subsection discusses how this mission is accomplished in the WAAS-aided FIS.

5.3 WAAS-aided FIS System Architecture

The WAAS-aided FIS system architecture is shown in Figure 5.4. The WAAS-aided FIS consists of an INS, a radar altimeter, a TVPS, and an airborne Commercial off-the-shelf (COTS) certified WAAS receiver. The WAAS and the INS provide their own position solutions during approach. Over the threshold of a runway, the radar altimeter measures the vertical distance between the airplane and the runway threshold. At that point, the TVPS measures the cross-track and along-track deviations of the airplane from the center line and the threshold mark of the runway by using its camera images. Since the position of the runway threshold is accurately surveyed, the radar altimeter and the TVPS provide an accurate instant 3D position of the airplane over the threshold.

After finishing the approach, position solutions of the WAAS and the INS are fused to remove the WAAS cyclic noise. Once the noise is removed, the noiseless WAAS position over the runway threshold is compared with the radar altimeter and TVPS reading at the same point to estimate the WAAS bias for that particular approach. Then, the estimated true trajectory is obtained by subtracting the estimated WAAS position bias from the noiseless WAAS position.

The main function of the INS is to remove the cyclic noises of the WAAS which is the primary sensor in this system. Since the INS is mainly used to filter out the cyclic noise of the WAAS, an expensive INS is not required. Furthermore, it is not required to fly along the length of the runway in order to calibrate the INS gyros and accelerometers. A navigation grade INS along with the calibration procedures are

required in the Inertial-based AFIS. Therefore, the WAAS-aided FIS has advantages of low cost and better efficiency over the Inertial-based AFIS.

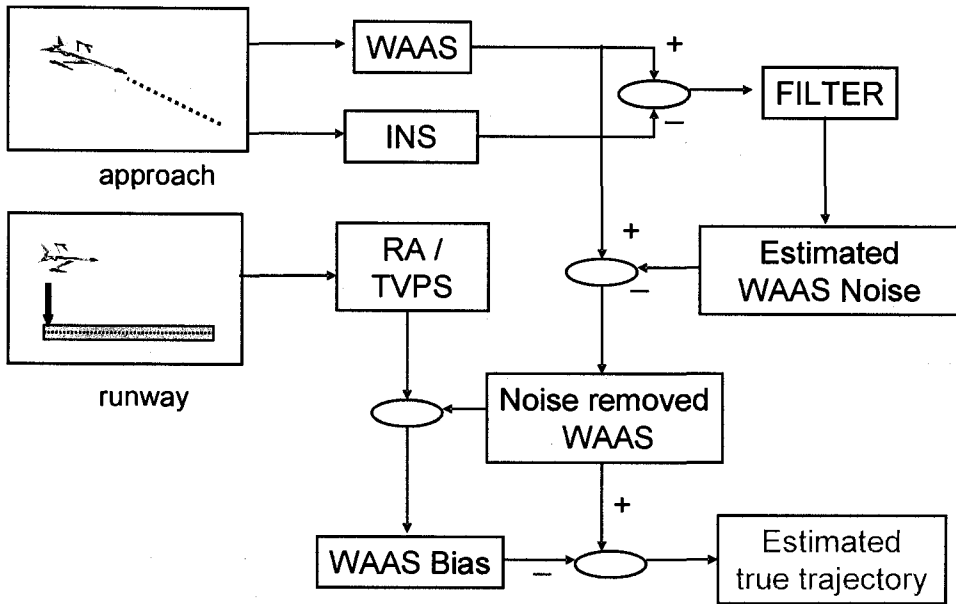


Figure 5.4: WAAS-aided FIS system architecture

5.3.1 WAAS Cyclic Noise Filtering Process

The WAAS-aided FIS takes advantage of the bias-like position error of the WAAS over a short period of time (minutes). If the bias can be estimated correctly at one time during approach, it is possible to have accurate position solutions by subtracting the estimated bias from the WAAS position outputs. However, the amplitude of the cyclic noise is so large that it must be removed before estimating the bias. Otherwise, the estimated bias may have a significant portion of the noise. Therefore, the cyclic noise removal process is critical. This subsection introduces how to robustly remove the cyclic noise of the WAAS by using an INS.

The sensor measurements of the INS and the WAAS can be described as follows:

$$\begin{aligned} z_{ins}(t) &= P_T(t) + B_i(t) + x(t) \\ z_{waas}(t) &= P_T(t) + B_w(t) + N_w(t) + \eta_w(t) \end{aligned} \quad (5.2)$$

where $P_T(t)$ is the true trajectory, $B_i(t)$ and $B_w(t)$ are biases in the measurements of the INS and the WAAS, respectively, $x(t)$ is the inertial drift, and $N_w(t)$ is the cyclic noise in the WAAS. $\eta_w(t)$ includes other noises such as multipath, receiver noise, and unmodeled effects in the WAAS.

Subtracting the INS position from the WAAS position yields

$$\begin{aligned} \Delta z(t) &= z_{waas}(t) - z_{ins}(t) \\ &= N_w(t) + B_w(t) - B_i(t) - x(t) + \eta_w(t) \end{aligned} \quad (5.3)$$

Assuming that the sensor measurement model is valid during approach, Equation (5.3) reveals the important fact that the motion of the airplane has no impact on the difference, $\Delta z(t)$, which makes the filtering performance independent of the airplane motion. Considering $\eta_w(t)$ to be small and making the bias term zero, the problem becomes how to separate the cyclic noise, $N_w(t)$, and the inertial drift, $x(t)$.

To design a filter separating $N_w(t)$ from $x(t)$, it is necessary to know the characteristics of $x(t)$. In general, the propagation of an inertial drift is very complicated and has some uncertainty [Titterton]. However, these complexities can be simplified by considering the flight motion during flight inspection: short operation time, approximately a straight line trajectory, nearly non-rotating and non-accelerating motions. Equation (5.4) shows a simplified linear error model of an INS in NED (North, East, Down) coordinates [Titterton].

$$\begin{aligned}
\ddot{x}_N &= \beta_N - g(-\phi_E) \\
-\dot{\phi}_E &= \dot{x}_N / R_e - \varepsilon_E \\
\ddot{x}_E &= \beta_E - g\phi_N \\
\dot{\phi}_N &= \dot{x}_E / R_e + \varepsilon_N \\
\ddot{x}_D &= \beta_D \\
\dot{\phi}_D &= \varepsilon_D
\end{aligned} \tag{5.4}$$

where

x = position error;
 β = accelerometer bias;
 ε = gyro drift rate;
 ϕ = platform tilt error;
 g = acceleration of gravity; and
 R_e = radius of earth

Assuming that the accelerometer biases are nearly constant during the approach, Equation (5.4) tells us that the horizontal error nearly grows with t^3 . On the other hand, the vertical error is driven by a constant accelerometer bias, and thus grows with t^2 . Let us first look at the filtering technique in the vertical channel due to its simplicity.

From Equation (5.4), the inertial drift in the vertical channel in continuous time can be described as follows.

$$x_D(t) = x_{D_0} + v_{D_0}t + \frac{1}{2}\beta_D t^2 \tag{5.5}$$

where x_{D_0} and v_{D_0} are the initial position and initial velocity, respectively.

Modeling the cyclic noise, $N_w(t)$, as $A_N(t)\sin(\frac{2\pi}{T}t)$ and ignoring the biases, Equation (5.3) becomes

$$\Delta z_D(t) = A_N(t)\sin(\frac{2\pi}{T}t) - x_D(t) + \eta_w(t) \tag{5.6}$$

where $A_N(t)$ is the time-varying amplitude of the cyclic noise.

Equation (5.6) shows that $\Delta z_D(t)$ is basically the sum of the cyclic noise with a time-varying amplitude and a quadratic curve whose curvature depends on β_D . The value of β_D varies with the grade of an INS and has some uncertainty during operation. Therefore, a robust filtering technique is necessary to be able to effectively select the cyclic noise regardless of the value of β_D and the time-varying amplitude from $\Delta z_D(t)$.

Since a near-real-time process is allowed, a non-causal zero-phase high pass filter [Mitra] is of interest. A high pass filter can be easily designed by using some basic low pass filters. Considering the time-varying amplitude of the sine wave, a symmetric triangular shape is selected for a low pass filter. Equation (5.7) describes this low pass filter in discrete time and Figure 5.5 shows its impulse response.

$$h[t] = \frac{1}{T^2}(-|t| + T), \quad -T \leq t \leq T \quad (5.7)$$

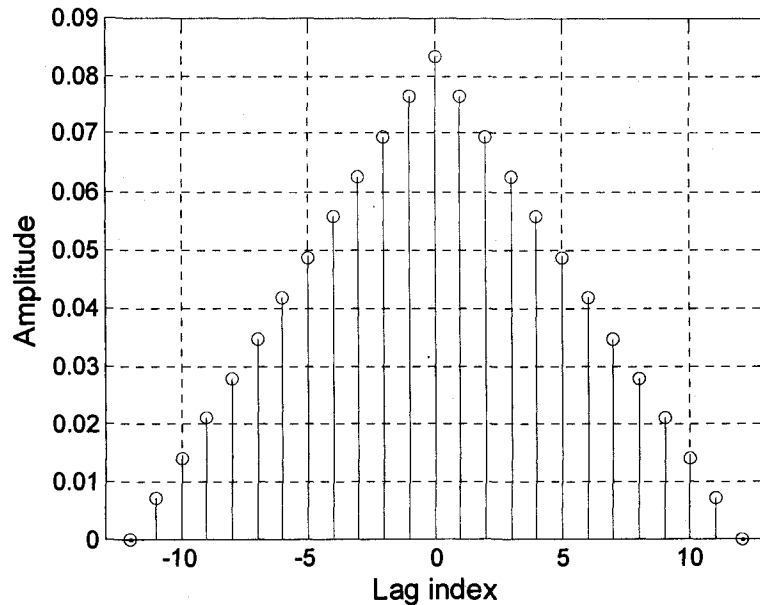


Figure 5.5: Impulse response of the designed low pass filter

The output of the filter at time n with input sampled at 1 Hz, $y[n]$, is

$$\begin{aligned}
y[n] &= \sum_{k=-T}^T h[k] \Delta z_D[n-k] \\
&= \frac{1}{T^2} \sum_{k=-T}^T (-|k|+T) (A_N[n-k] \sin[\frac{2\pi}{T}(n-k)] - \\
&\quad x_D[n-k] + \eta_w[n]) \\
&= -x_D[n] - \frac{143}{T} \beta_D + \eta_{w,s}[n]
\end{aligned} \tag{5.8}$$

where $\eta_{w,s}[n]$ is noise due to the incomplete cancellation of the sine wave and the WAAS noise. It is interesting that, in addition to the vertical drift error, $x_D[n]$, $y[n]$ results in a constant bias term, $\frac{143}{T} \beta_D$, that does not depend on time, n . Therefore, subtracting $y[n]$ from $\Delta z_D[n]$ produces

$$\begin{aligned}
e_D[n] &= \Delta z_D[n] - y[n] \\
&= A_N[n] \sin[\frac{2\pi}{T} n] + \frac{143}{T} \beta_D[n] + \hat{\eta}_e[n]
\end{aligned} \tag{5.9}$$

Filtering $e_D[n]$ with the same filter, h , results in

$$\begin{aligned}
V_D(n) &= \sum_{k=-T}^T h[n] e_D[n-k] \\
&= \frac{143}{T} \beta_D[n] + \hat{\eta}_v[n]
\end{aligned} \tag{5.10}$$

Therefore, the cyclic noise term can be estimated as follows:

$$\begin{aligned}
\hat{N}_{w,D}[n] &= e_D[n] - V_D[n] \\
&= A_N[n] \sin[\frac{2\pi}{T} n] + \hat{\eta}_{v,e}[n]
\end{aligned} \tag{5.11}$$

The filtering process in a horizontal channel is the same as in the vertical channel, but the low pass filter results in a slightly different term. From Equation (5.4), the inertial drift in the east channel is described below.

$$x_E(t) = x_{E0} + v_{E0}t + \frac{1}{2}\beta_{E0}t^2 + \frac{1}{6}\varepsilon t^3 \quad (5.12)$$

Following a similar procedure to Equation (5.8), the filter outputs at time n are

$$\begin{aligned} y[n] &= \sum_{k=-T}^T h[k]\Delta z_E[n-k] \\ &= -x_E[n] - \frac{143}{T}\beta_E[n] - 4\varepsilon + \eta_{w,s}[n] \end{aligned} \quad (5.13)$$

Unlike the previous case, the filter results in an additional term which is a nearly linear function of time.

Now, the difference between $y[n]$ and $\Delta z_E[n]$ is

$$\begin{aligned} e_E[n] &= \Delta z_E[n] - y[n] \\ &= A_N[n]\sin\left[\frac{2\pi}{T}n\right] + \frac{143}{T}\beta_E[n] + 4\varepsilon + \hat{\eta}_e[n] \end{aligned} \quad (5.14)$$

Filtering $e_E[n]$ with the same filter, h , results in

$$\begin{aligned} V_E[n] &= \sum_{k=-T}^T h[k]e_E[n-k] \\ &= \frac{143}{T}\beta_E[n] + 4\varepsilon + \hat{\eta}_v[n] \end{aligned} \quad (5.15)$$

Therefore, the cyclic noise term can be estimated as follows:

$$\begin{aligned} \hat{N}_{w,E}[n] &= e_E[n] - V_E[n] \\ &= A_N[n]\sin\left[\frac{2\pi}{T}n\right] + \hat{\eta}_{v,e}[n] \end{aligned} \quad (5.16)$$

Figure 5.6 illustrates the high pass filter design process in the vertical and horizontal channels.

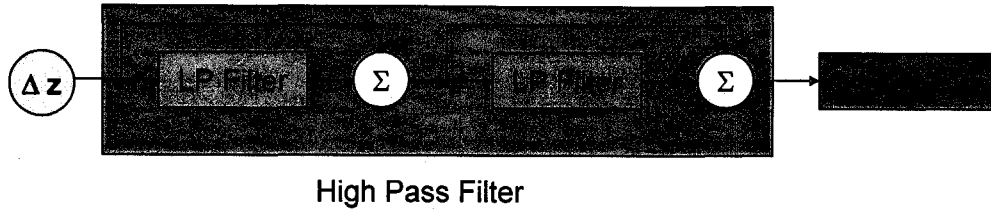


Figure 5.6: High pass filtering block for cyclic noise

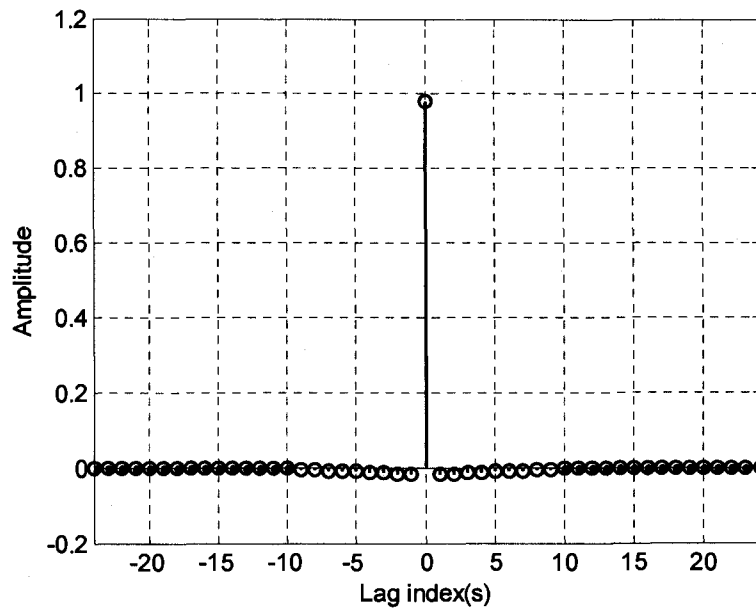


Figure 5.7: Impulse response of the designed high pass filter

Figure 5.7 and Figure 5.8 show the impulse response of the high pass filter in discrete time and its frequency response, respectively.

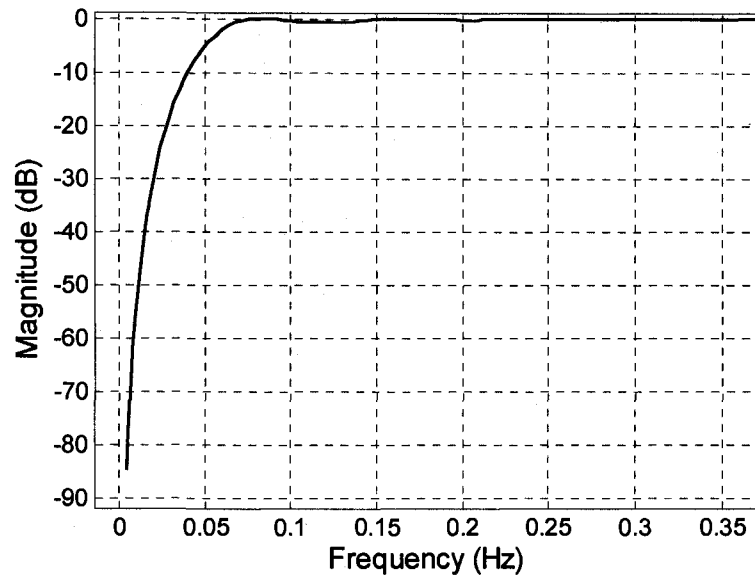


Figure 5.8: Frequency response of the designed high pass filter

As an example, Figure 5.9 shows the true WAAS noise and the estimated WAAS noise from the high pass filtering block. The residual errors of the estimated WAAS noise are shown in Figure 5.10. As shown in these figures, this filter effectively selects the periodic noise so that the residual errors are, most of the time, less than 0.1 m. These errors previously exceeded 0.2 m.

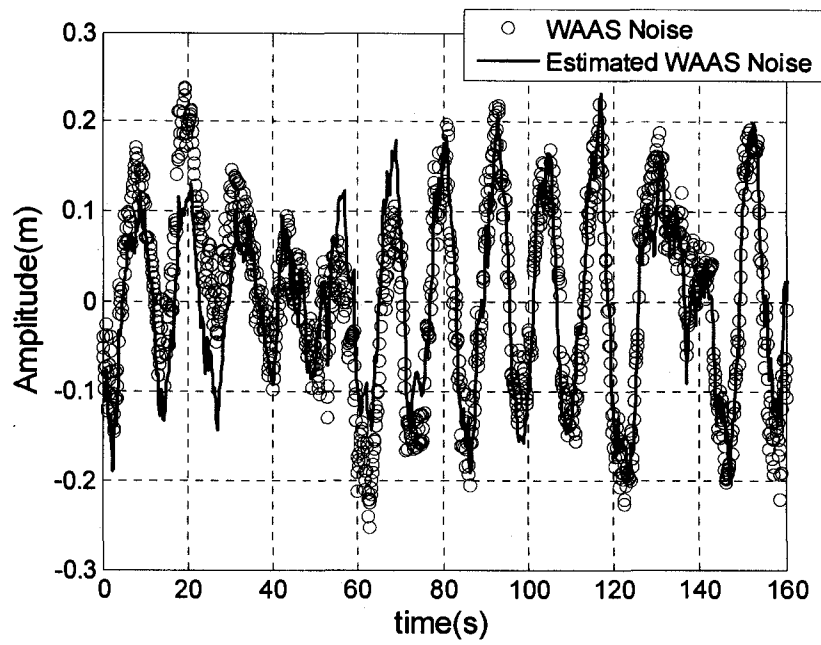


Figure 5.9: Comparison of WAAS noise and estimated WAAS noise

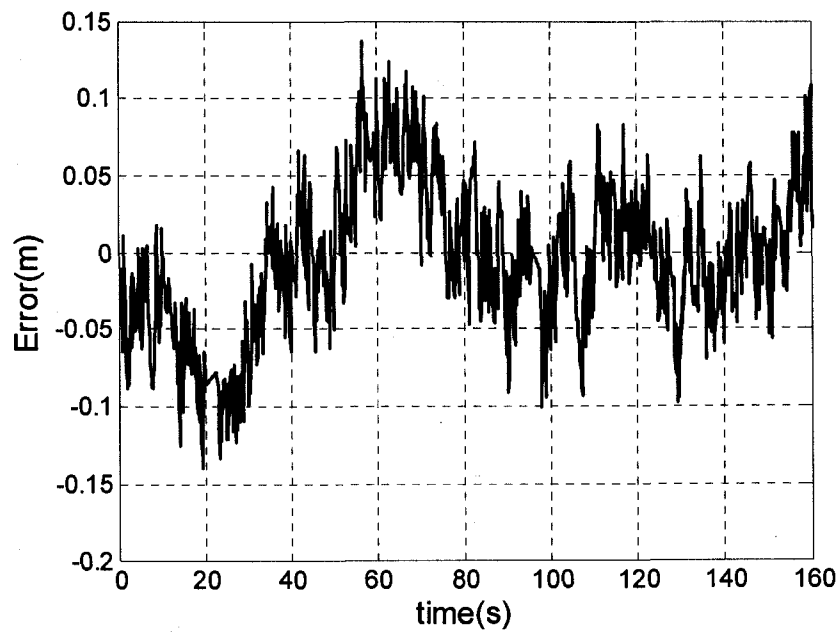


Figure 5.10: The residual errors of the estimated WAAS noise

5.3.2 Estimation of True Trajectory

After the cyclic noise process is completed, the remaining process in estimating the flight path is straightforward. First, noise reduced WAAS measurements are obtained as follows:

$$\begin{aligned}
 z_{noiseless_waas}(t) &= z_{waas}(t) - \hat{N}_w(t) \\
 &= P_T(t) + B_w(t) + N_w(t) - \hat{N}_w(t) + \eta_w(t) \\
 &= P_T(t) + B_w(t) + \eta(t)
 \end{aligned} \tag{5.17}$$

It is important to keep in mind that this noiseless WAAS position, $z_{noiseless_waas}(t)$, not only provides smooth position outputs but also makes it possible to accurately determine the bias, $B_w(t)$, of WAAS by using other sensors. To estimate the bias in the WAAS position, it is necessary to have more accurate position measurements than WAAS provides. The radar altimeter currently used in the Inertial-based AFIS has accuracy (95%) better than 15 cm [Peled]. The TVPS has accuracy (95%) better than 15 cm in cross-track and 30 cm in along-track, respectively [TVPS]. The WAAS position bias is obtained from the position measurements of those sensors at the runway threshold in a manner similar to the Inertial-based AFIS.

Let us denote the position estimate from the radar altimeter and the TVPS as $z_{RA_TVPS}(t)$. Then, the WAAS bias, $B_w(t)$, is obtained by subtracting $z_{RA_TVPS}(t)$ from the noiseless WAAS position, $z_{noiseless_waas}(t)$, at the threshold as follows:

$$\hat{B}_w(t) = [z_{noiseless_waas}(t) - z_{RA_TVPS}(t)]_{at\ threshold} \tag{5.18}$$

This bias estimate, $\hat{B}_w(t)$, is usually a constant for the duration of the approach. However, $\hat{B}_w(t)$ may have a sudden jump when there is a satellite constellation

change or step change in the WAAS message. This issue will be discussed in a later section.

By subtracting $\hat{B}_w(t)$ from $z_{noiseless_waas}(t)$, the noise and bias removed WAAS position, $z_{true_waas}(t)$, is obtained.

$$z_{true_waas}(t) = z_{noiseless_waas}(t) - \hat{B}_w(t) \quad (5.19)$$

$z_{true_waas}(t)$ is the estimated true trajectory and will be used to calibrate the ILS.

5.3.3 Effect of Satellite Geometry Changes and Ionospheric Delay Correction Updates

If the WAAS position bias experiences a large sudden jump near the runway threshold, the estimated true trajectory may be corrupted because the bias estimation from a radar altimeter and a TVPS is no longer valid throughout the whole approach. The potential factors that may cause a bias jump are satellite geometry change and ionospheric delay correction updates. Fortunately, these factors typically do not cause a large bias jump during approach. The reasons are discussed in this section.

When a satellite at a high elevation angle experiences an outage, it may cause a large discontinuity in the bias. Considering the motion of an airplane during approach, this type of high elevation outage is unlikely. Instead, the satellite constellation change usually occurs due to a rising or falling satellite. In this case, the satellite geometry change does not make much difference in the bias because those satellites are heavily de-weighted in computing position solutions. Now, let us consider the case of ionospheric delay correction updates. The WAAS broadcasts IGP vertical delays less than every 5 minutes, and its resolution is 0.125 meters [WAASMOPS]. There is a chance that the ionospheric delay correction updates may occur near the runway threshold. However, under normal conditions the ionospheric delay is strongly correlated with time, which means that one broadcast IGP vertical delay does not

significantly differ from the previous one. Therefore, the ionospheric delay updates also do not introduce a large bias jump on nominal ionospheric days.

5.4 Flight Test Results

5.4.1 Flight Test Results with Navigation Grade INS

The proposed algorithm is tested with flight test data taken during Oct 30-31, 2006 at Oklahoma City. A total of 23 approaches are used for the experimental results. The current Inertial-based AFIS was used to collect the data, therefore a navigation grade INS was used. The output rate of the WAAS measurements and inertial measurements are 1 Hz and 50 Hz, respectively. In order to evaluate the accuracy of the WAAS-aided FIS, DGPS positions with 5 Hz output rate are used as truth sources. Unfortunately, a radar altimeter and a TVPS were not used during the tests due to hardware difficulties. Therefore, the DGPS positions were used instead of a radar altimeter and a TVPS. Figure 5.11 shows some examples of flight paths during the flight tests.

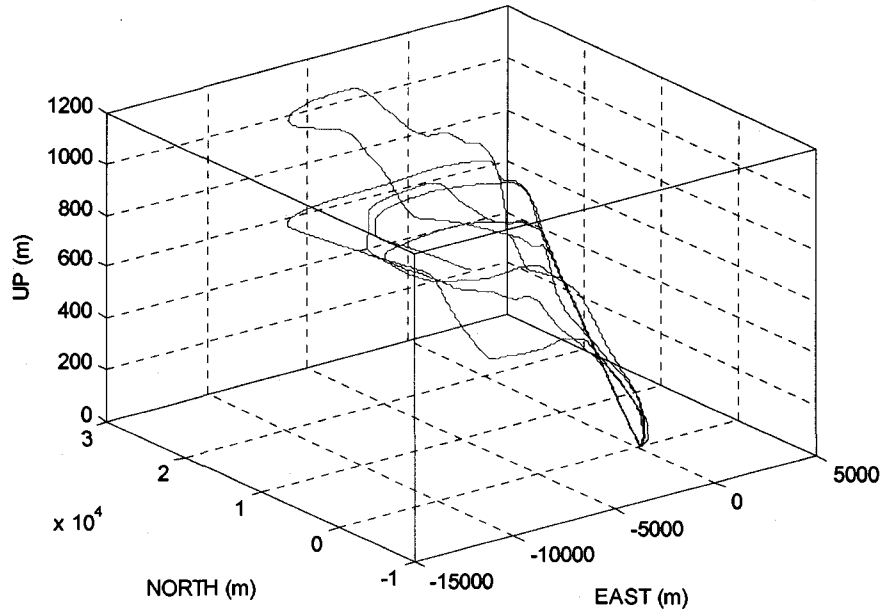


Figure 5.11: Examples of flight path during flight tests at Oklahoma City

Figure 5.12 and 5.13 show WAAS-aided positioning errors in vertical and cross-track without radar altimeter and TVPS errors. The allowable error limits with respect to different categories of an ILS as described in Section 1.3.2 are also described in those figures. Errors from a radar altimeter or TVPS would be added to the errors shown in the figures.

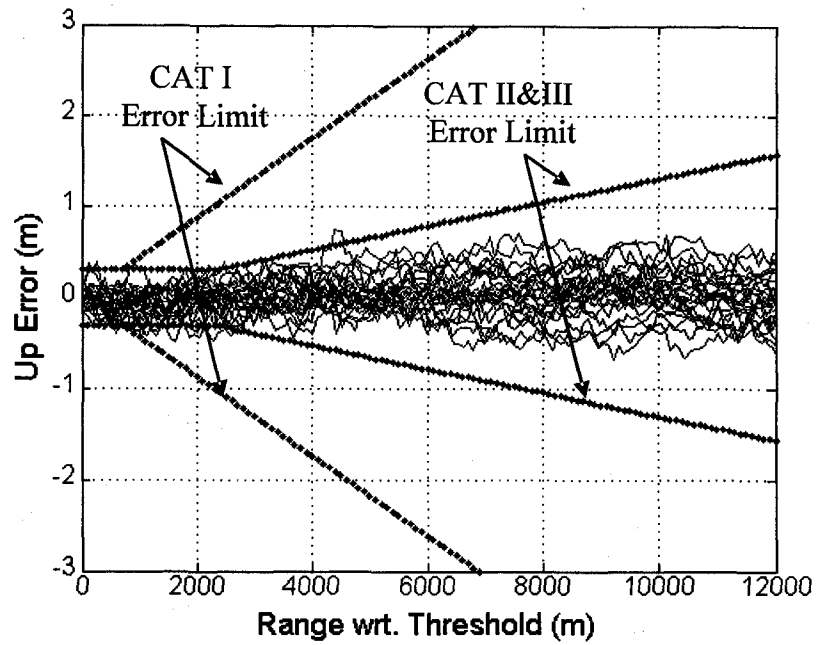


Figure 5.12: WAAS-aided FIS vertical position error without radar altimeter error

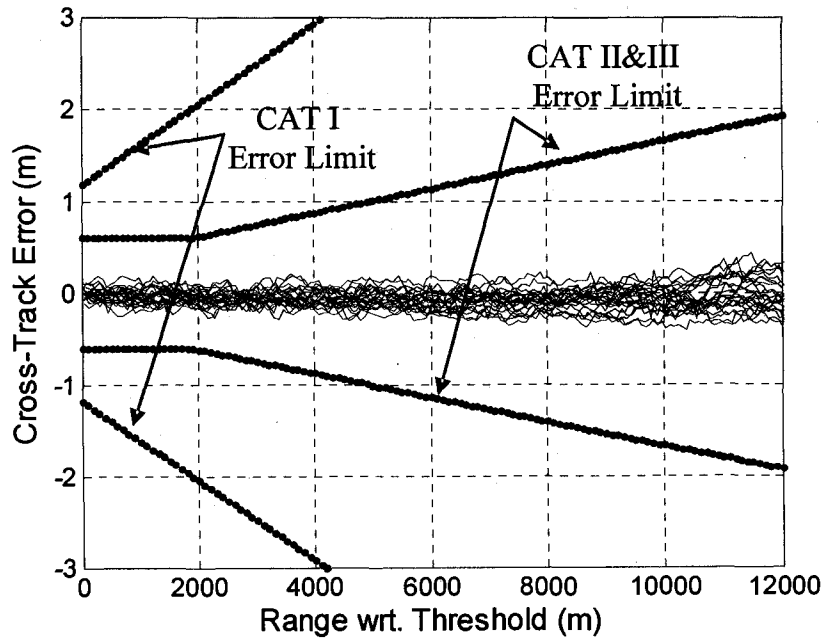


Figure 5.13: WAAS-aided FIS cross-track position error without TVPS error

5.4.2 Flight Test Results with Simulated Tactical and an Automotive Grade INS

In this section, the WAAS-aided FIS is tested with simulated horizontal measurements of a low-end tactical grade INS and an automotive grade INS. The measurements of the low grade INS are generated by adding errors to the navigation grade INS measurements. The added errors are simulated by assuming that the accelerometer and gyro errors are mainly biases with white noise. Table 5.1 summarizes the parameters of the error model of a low-end tactical grade INS and an automotive grade INS [Bar-Shalom].

Table 5.1: Biases and Power Spectra of Accelerometer and Gyro

Sensor Parameter	Unit	Tactical	Automotive
Accelerometer bias	μg	500	30,000
Gyro bias	deg/hour	1	100
Accelerometer white noise	$(\mu g)^2 / \text{Hz}$	2500	5000
Gyro white noise	$(\text{deg/s})^2 / \text{Hz}$	10^{-6}	10^{-4}

Figure 5.14 and 5.15 show the simulated horizontal errors for a tactical grade INS and an automotive grade INS.

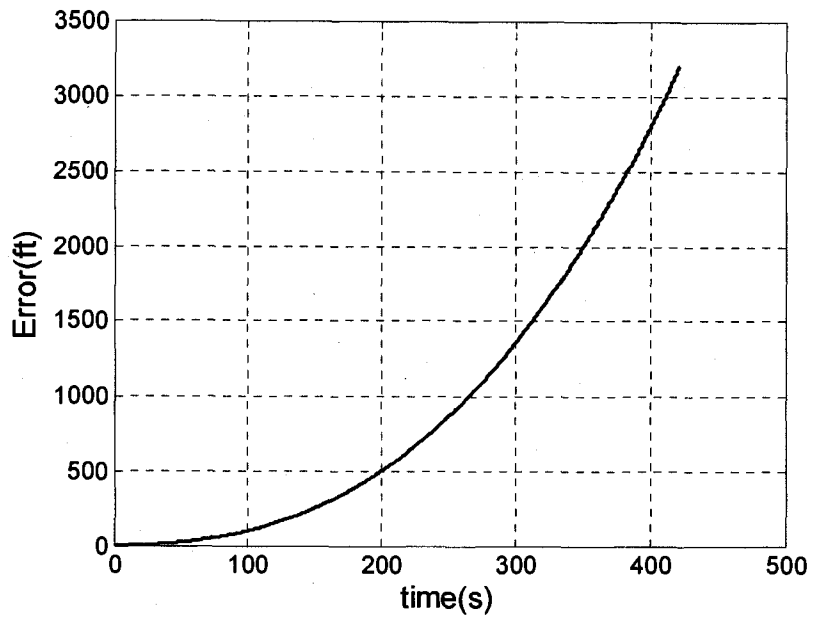


Figure 5.14: Simulated horizontal error for a tactical grade INS

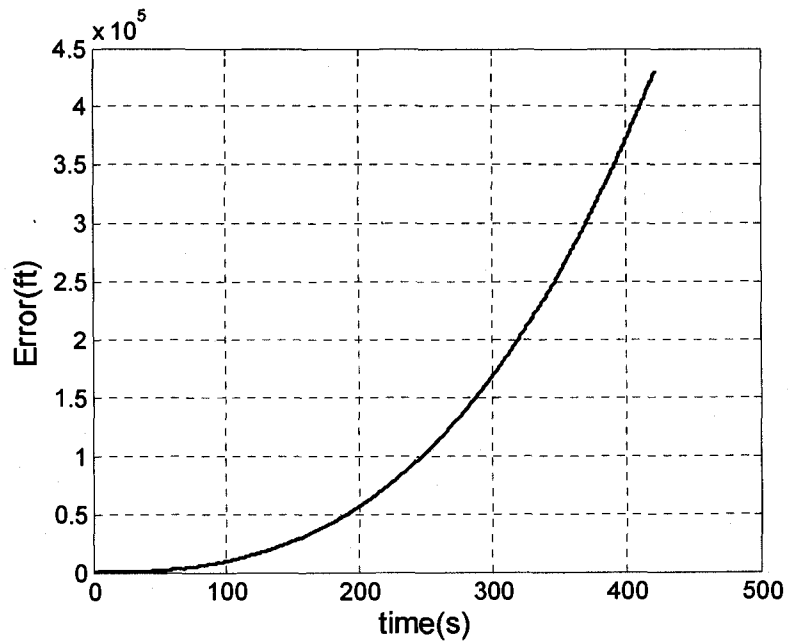


Figure 5.15: Simulated horizontal error for an automotive grade INS

Figure 5.16 and 5.17 show the vertical and cross-track position errors without errors from a radar altimeter and a TVPS using the simulated low-end tactical grade INS. In the results, it is hard to find any difference in the position errors using the navigation grade INS.

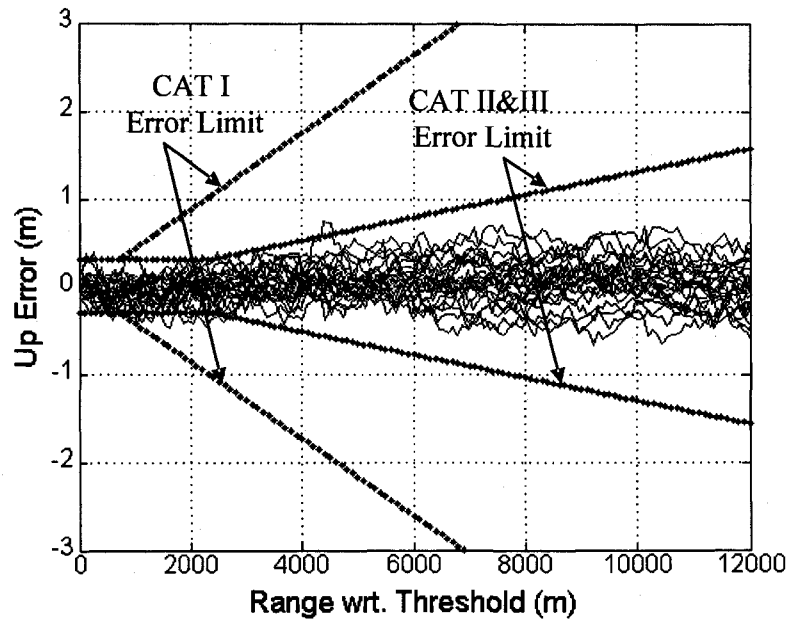


Figure 5.16: WAAS-aided FIS vertical position error without a radar altimeter error using a simulated tactical grade INS

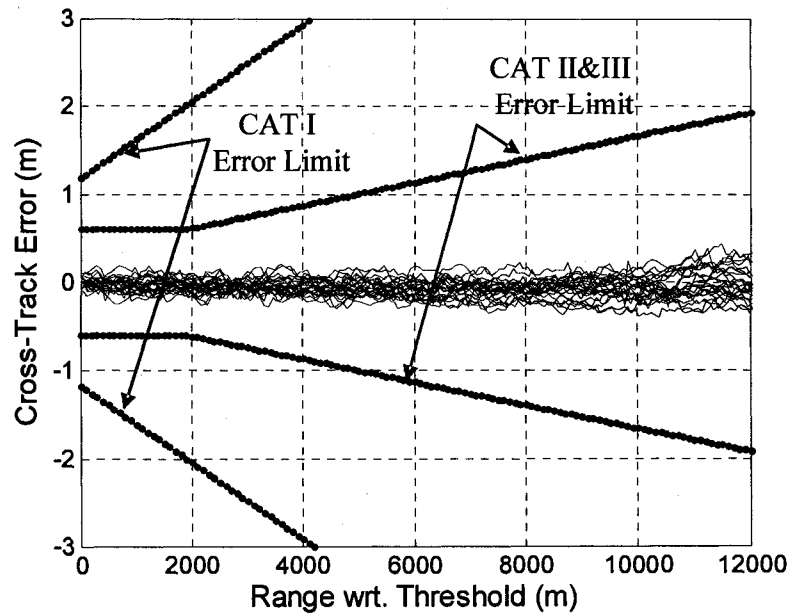


Figure 5.17: WAAS-aided FIS cross-track position error without a TVPS error using a simulated tactical grade INS

Figure 5.18 and 5.19 show the vertical and cross-track position errors without a radar altimeter and a TVPS using the simulated automotive grade INS. As was the case for the tactical grade INS, there is no significant difference in the position errors using the navigation grade INS.

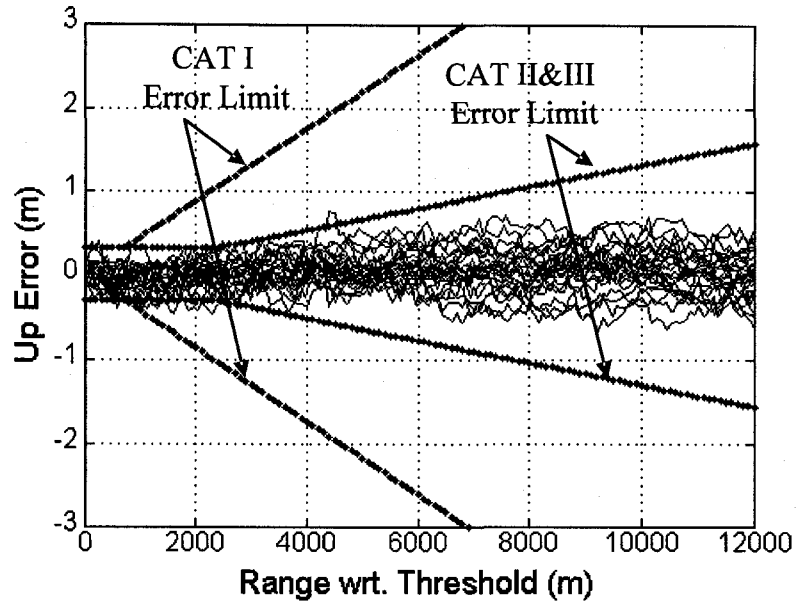


Figure 5.18: WAAS-aided FIS vertical position error using a simulated automotive grade INS without radar altimeter error

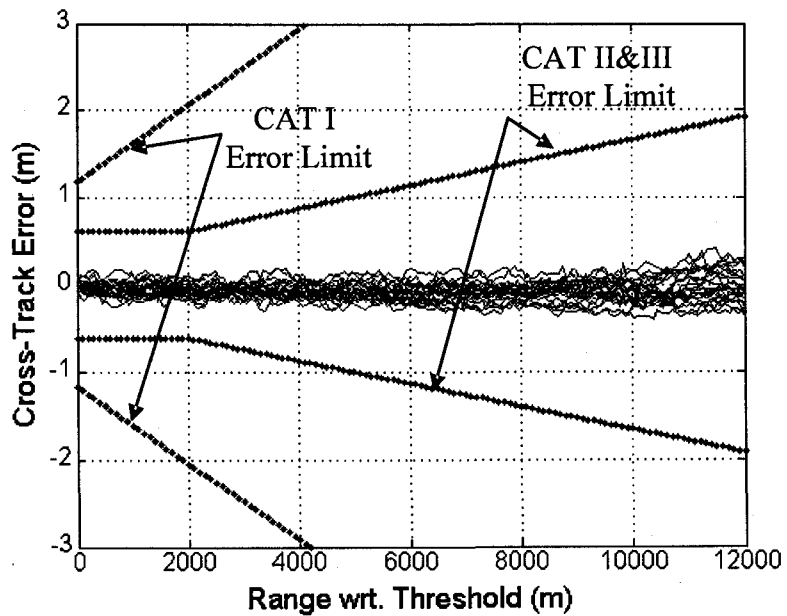


Figure 5.19: WAAS-aided FIS cross-track position error using a simulated automotive grade INS without TVPS error

5.4.3 WAAS-aided Flight Inspection System Accuracy

In the previous section, the WAAS-aided FIS position errors without errors from a radar altimeter and a TVPS were shown. Now, it is necessary to quantize the overall WAAS-aided FIS accuracy to see whether this system meets the FAA flight inspection system accuracy requirements.

Observing the set of position errors, it should be noted that the critical range where the requirement may be violated is from 0 to 2000 meters in cross-track and from 0 to 2200 meters in vertical. Now, let us consider the set of errors in this region as independent zero mean random variables. The statistics of the errors are summarized in Table 5.2. The accuracy (95%) of a radar altimeter is 15 cm. The accuracy (95%) of a TVPS in cross-track is also 15 cm. The accuracy (95%) of the WAAS-aided FIS can be computed by using the accuracy of a radar altimeter and a TVPS. Then, the WAAS-aided FIS 95% accuracy is 34 cm in vertical and 23 cm in cross-track at the critical range. This was computed by calculating the RSS of 95% quantities from Table 5.2 and the RA and TVPS accuracies. Therefore, it can be said that the WAAS-aided FIS is slightly insufficient or marginally meets the flight inspection system accuracy requirements whose limits are about 30 cm in vertical and 60 cm in cross-track.

Table 5.2: Statistics of the WAAS-aided FIS position errors without radar altimeter and TVPS errors in the critical range

	Up (m)	Cross-Track (m)
Mean	-0.027	-0.037
Std	0.150	0.085
RMS	0.152	0.093
2*Std (95%)	0.300	0.170

5.5 Conclusion

The WAAS-aided FIS is introduced in this chapter. This system uses a Commercial off-the-shelf (COTS) certified WAAS receiver as a primary sensor with a low cost INS, a radar altimeter, and a TVPS. The fusion of the WAAS with an INS and the bias detection process are extensively discussed. The WAAS-aided FIS is tested with the flight test data, and the results are presented. Also, it is shown that a low-end tactical grade INS and an automotive grade INS are feasible in this system.

Overall, the WAAS-aided FIS offers low cost and high efficiency. The low cost is achieved by replacing the expensive navigation grade INS with a low-end tactical grade INS or an automotive grade INS. The high efficiency is obtained from the fact that a flight inspection airplane does not need to fly over the whole runway as the Inertial-based AFIS does. In addition, the system can be easily realized from the Inertial-based AFIS due to the similarity of their hardware. However, the accuracy of a WAAS-aided FIS is slightly outside of the FAA flight inspection system accuracy requirements. The lateral accuracy is sufficient, but the vertical accuracy is lacking by about 3.5 cm. This lack of accuracy is mainly caused by multipath and receiver noise that hinders accurate determination of a WAAS position bias over the runway threshold. Although the WAAS-aided FIS accuracy may not be acceptable in practice, the system can be still used as an integrity monitor of the Inertial-based AFIS since two different position solutions can be obtained. Another limitation of the WAAS-aided FIS is that it has the same threat as the WAAS, i.e., a sharp ionospheric gradient.

Chapter 6

WAAS-based Flight Inspection System

6.1 Introduction

The WAAS-based Flight Inspection System (FIS) is introduced in this chapter [Kim072]. This system has a single frequency modified WAAS receiver, a radar altimeter, and a TVPS. A WAAS receiver in this system must be able to output GPS and WAAS raw messages. This system uses the T-D PRP algorithm and the reference position given from a radar altimeter along with a TVPS to estimate the true flight trajectory during flight inspection. Taking advantage of WAAS accuracy and broadcast messages, the WAAS-based FIS is equipped with a firm integrity so that this system is protected against satellite failures and a large error in the reference position from a radar altimeter and a TVPS. Overall, the WAAS-based FIS provides optimal performance in terms of accuracy, cost, efficiency, and integrity. However, the WAAS-based FIS is only operational where WAAS or SBAS is available.

This chapter is organized as follows. In Section 6.2, the overall WAAS-based FIS system architecture is discussed including satellite exclusion tests, WAAS fast clock correction filtering, and reference position validation. The T-D PRP is not described in this section. Please refer to Chapter 4 for more information about the T-D PRP. Then, the experimental test results are presented in Section 6.3. Lastly, the conclusion follows in Section 6.4.

6.2 WAAS-based FIS System Architecture

The WAAS-based FIS has a single frequency modified WAAS receiver, a radar altimeter, and a TVPS. The same kinds of radar altimeter and TVPS used in the Inertial-based AFIS are taken for the WAAS-based FIS. This integrated system is optimally designed for the ILS calibration problem in terms of accuracy, cost, efficiency, and integrity.

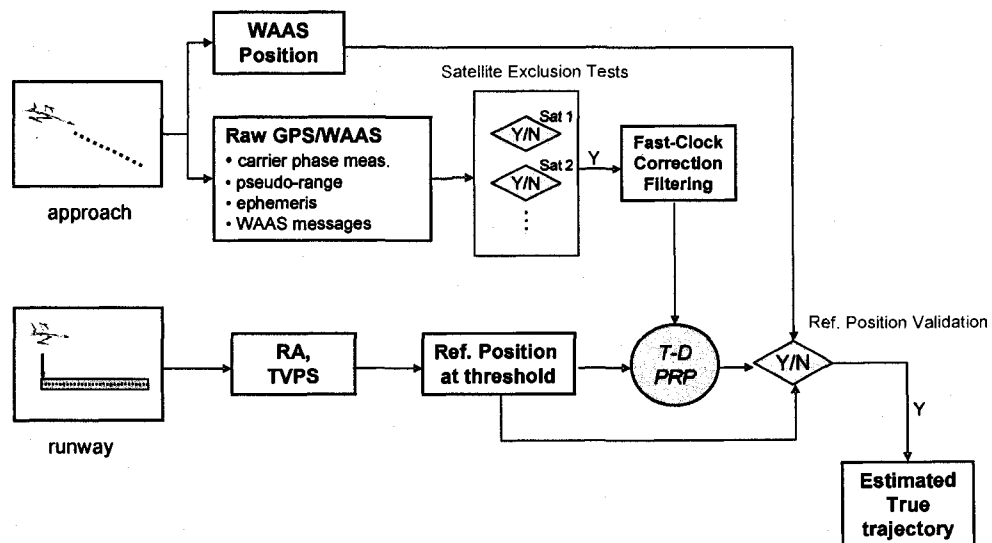


Figure 6.1: WAAS-Based FIS system architecture

Figure 6.1 illustrates the overall WAAS-based FIS architecture. During approach, WAAS position and raw GPS/WAAS measurements are collected. The GPS/WAAS measurements include ephemeris, L1 code and carrier phase measurements, and WAAS messages. Over the runway threshold, a radar altimeter and a TVPS provide a reference position for CAT II-III ILS. However, WAAS can substitute for a TVPS in the WAAS-based FIS for CAT I ILS calibration. The Time-Differenced Precise Relative Positioning (T-D PRP) method uses this reference position and the raw measurements to compute precise relative positions. The estimated flight trajectory during approach is obtained by adding the relative positions to the reference position. There are two integrity features for the soundness of the estimated flight trajectory: satellite exclusion tests and validation of the reference position. Satellite exclusion tests are implemented to discard a satellite that should not be used in the T-D PRP during approach. The integrity of a reference position is checked by using both WAAS position during approach and the precise relative position from the T-D PRP. Even though this validation test is limited to the level of WAAS accuracy, it is useful when a radar altimeter or a TVPS introduces an abnormally large error. The two integrity features will be further discussed later in this section.

In this section, satellite exclusion tests, fast-clock correction filtering, and validation of reference position are discussed in more detail.

6.2.1 Satellite Exclusion Tests

The position solution of the WAAS-based FIS is obtained by adding the relative position from the T-D PRP to the reference point from a radar altimeter and a TVPS. To ensure sound position solutions from the T-D PRP, it is necessary to exclude any satellites that may cause adverse effects. This section discusses how to choose the right set of satellites for the T-D PRP using WAAS integrity messages and other internal sanity check procedures.

Figure 6.2 shows the items that should be checked before including a satellite for the T-D PRP. The first safety check is to see if there are any GPS/WAAS

UNHEALTHY or WAAS UNMONITORED designations. If these messages are delivered from GPS/WAAS for a particular satellite, that satellite will be excluded. Similarly, a satellite having UDREI greater than or equal to 12 will be excluded as well because that satellite may have some problem and therefore cannot be used for WAAS-based precision approach [WAASMOPS].

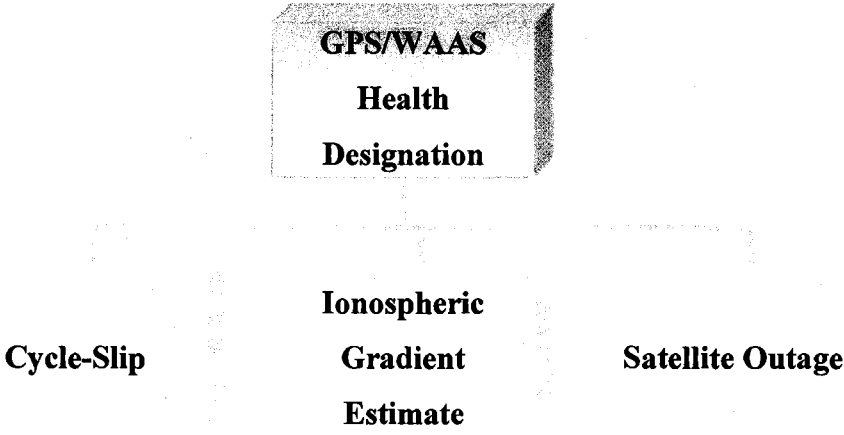


Figure 6.2: Chart of items for satellite exclusion criteria

Any satellites experiencing a cycle-slip during approach are also excluded because the T-D PRP must use continuously accumulated carrier phase measurements. In using the estimated ionospheric delay gradient in the T-D PRP, the goodness of fit for the estimation of the ionospheric delay gradient must be examined. Any ionospheric delay gradients showing a severe nonlinear behavior can be detected by analyzing the residuals after fitting a first order linear model on the time series of code minus carrier phase measurements. Chi-square tests are a good indicator for goodness of fit [Bar-Shalom]. Lastly, it is best to use the same set of satellites during the entire approach. A different set of satellites may introduce a sudden jump in relative position, which is undesirable for our application.

6.2.2 Fast-Clock Correction Filtering

In the WAAS-based FIS, the WAAS fast-clock correction message is used. As already discussed in the previous chapters, the WAAS fast-clock correction is not continuous and its combination of Range Rate Correction (RRC) makes large 12 s periodic noise. It should be noted that the periodic noise still remains due to the discrete WAAS fast-clock correction although RRC is turned off in a receiver. Therefore, the WAAS fast-clock correction needs to be filtered to be used in precise positioning. Figure 6.3 shows a typical example of the broadcast fast clock corrections and filtered fast clock corrections. The smoothing process takes place after receiving all the messages during approach. Since the message has a 12 second periodic pattern for a considerable amount of time, a non-causal moving average filter having 12 seconds or a multiple of 12 seconds length will remove the periodic pattern.

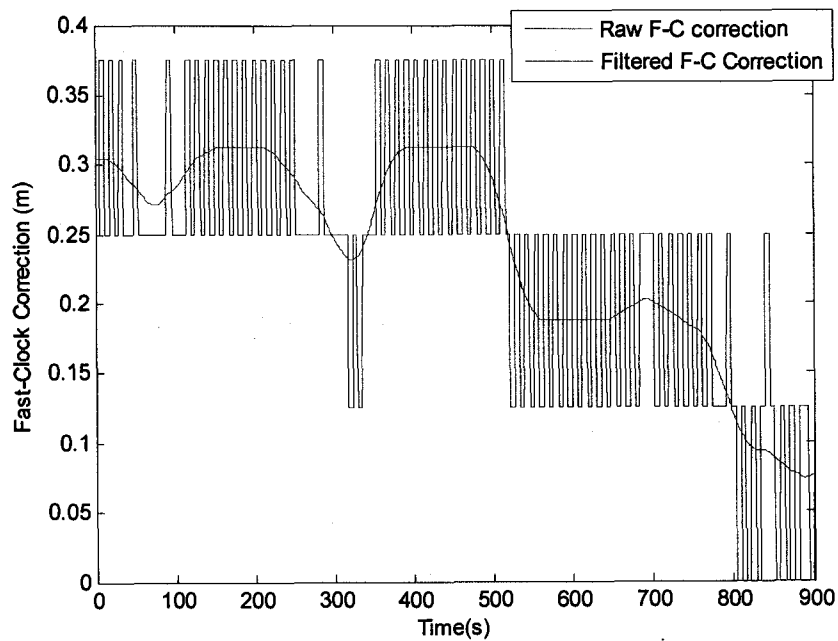


Figure 6.3: Example of fast-clock correction filtering using a non-causal filter

6.2.3 Validation of a Reference Position from Radar Altimeter and TVPS

A radar altimeter and a TVPS provide a reference position over the runway threshold. Since the estimated flight path is the sum of the reference position and the relative position from the T-D PRP, the accurate measurements from those sensors are extremely important. This subsection discusses how to validate the reference position using the WAAS position.

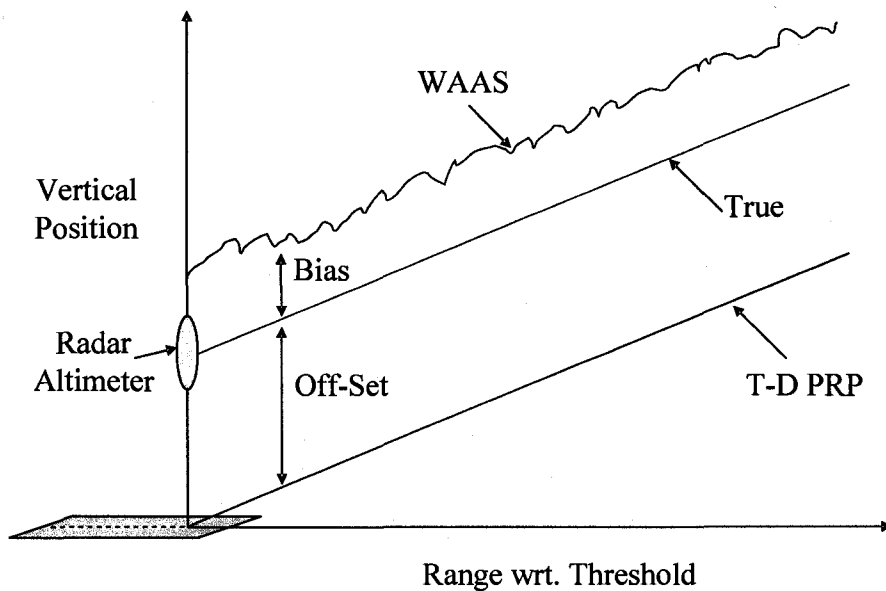


Figure 6.4: Schematics of the characteristics of three position measurements (R.A., WAAS, TD-PRP) with true position

Figure 6.4 depicts how a true flight trajectory is related with WAAS position and the relative position from the T-D PRP in the vertical direction. Basically, WAAS position has a constant bias and noise on top of the true position during approach [Kim062]. On the other hand, the position from the T-D PRP is precise but has a large

offset from the true position. Mathematically, these positions can be described as follows:

$$\begin{aligned} \text{WAAS} &= \text{True} + \text{Bias} + \text{Noise} \\ \text{T-D PRP} &= \text{True} - \text{Offset} \end{aligned} \quad (6.1)$$

Taking the average of the difference of the WAAS position and the T-D PRP position during approach yields the following expression,

$$\begin{aligned} \text{AVG}_{(\text{WAAS}-\text{T-D PRP})} &= \frac{1}{n} \sum_{t=0}^n (\text{WAAS} - \text{T-D PRP})_t \\ &\approx \text{Bias} + \text{Offset} \end{aligned} \quad (6.2)$$

In Equation (6.2), the noises in the WAAS position are averaged out to near zero.

Now, an instantaneous measurement of a radar altimeter over the threshold has a small error as follows:

$$\text{Radar Altimeter} = \text{True}_{\text{thr}} + \text{Error} \quad (6.3)$$

Then, the difference of measurements of a radar altimeter and the T-D PRP over the threshold is

$$\begin{aligned} \Delta_{(\text{RA}-\text{T-D PRP}_{\text{thr}})} &= \text{Radar Altimeter} - \text{T-D PRP}_{\text{thr}} \\ &= \text{Error} + \text{Offset} \end{aligned} \quad (6.4)$$

Then, if we subtract Equation (6.4) from Equation (6.2), the remaining term is approximately the sum of the WAAS bias and the small error from the radar altimeter,

$$\text{AVG}_{(\text{WAAS}-\text{T-D PRP})} - \Delta_{(\text{RA}-\text{T-D PRP}_{\text{thr}})} \approx \text{Bias} - \text{Error} \quad (6.5)$$

The message from Equation (6.5) is that once we know the statistical distributions of the WAAS bias and the radar altimeter error, which was already presented in the previous sections, we can also form a distribution of Equation (6.5). Using this distribution, it is possible to check where the value of Equation (6.5) stands on the distribution for each approach. If the value is beyond a threshold, for example 95% with two sided Gaussian distribution, a flag is raised to indicate a possible corruption in the radar altimeter measurement. A similar procedure can be used in the horizontal with a TVPS. Considering the 95% accuracies of the WAAS, a radar altimeter, and a TVPS, the thresholds (99.9%) are 1.50 meters in the horizontal and 2.12 meters in the vertical, respectively.

6.3 Flight Test Results

For the validation of the WAAS-based FIS, the same set of flight tests in the evaluation of the WAAS-aided FIS are used. Raw GPS/WAAS data were recorded using a Garmin 480 certified WAAS receiver that was modified so that raw measurements were available. The total number of approaches used in this test is 23.

6.3.1 T-D PRP Tests

Figure 6.5 and 6.6 show the horizontal and vertical errors from implementing the T-D PRP with a reference position given from a DGPS position. The two pairs of straight lines are the flight inspection system accuracy requirements for CAT I and CAT II-III ILS calibration as described in Chapter 1.

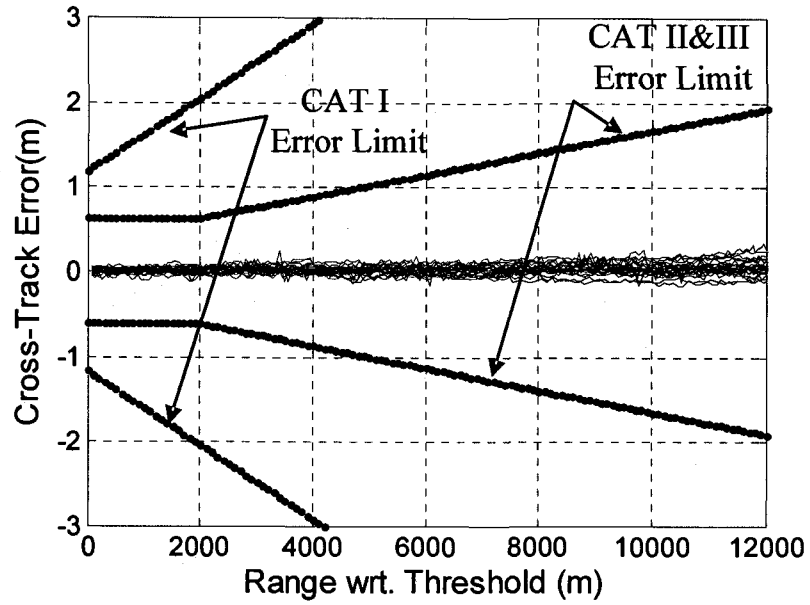


Figure 6.5: WAAS-based FIS cross-track position errors without a TVPS error

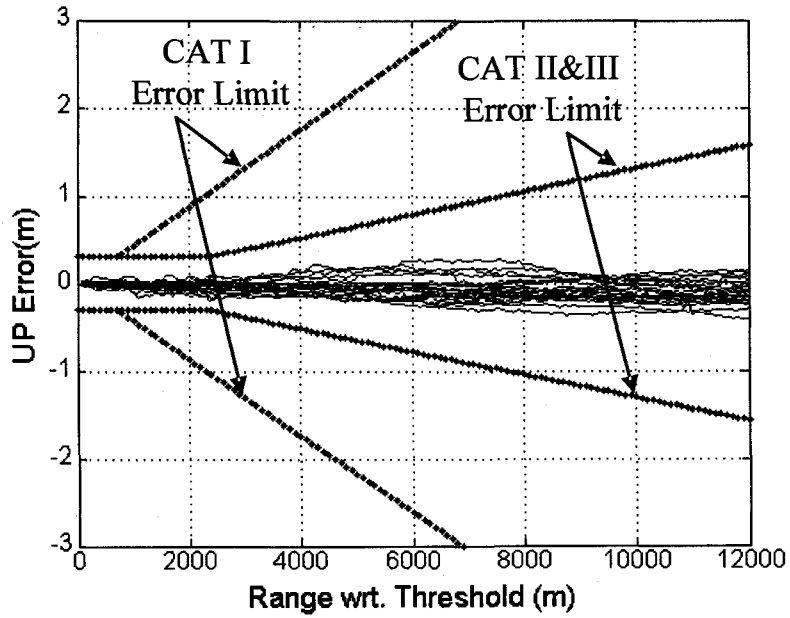


Figure 6.6: WAAS-based FIS vertical position errors without a radar altimeter error

These two figures do not represent the total errors of WAAS-based FIS tests because the reference position errors are not included. However, these results clearly show the error characteristic of the T-D PRP, which slowly increases over time. Based on that, it is possible to measure the performance of WAAS-based FIS using 95% accuracies of a radar altimeter and a TVPS.

6.3.2 WAAS-based FIS Accuracy

To see the accuracy of the WAAS-based FIS, the total errors caused by both the T-D PRP and the reference position should be considered. Considering the T-D PRP error characteristics and the accuracy requirements, the critical regions that most likely violate the accuracy requirements are around 2200 meters and 2000 meters from the threshold in the vertical and horizontal directions, respectively. If the WAAS-based FIS accuracy meets the flight inspection system accuracy requirements in these critical regions, it will meet the requirements for all other regions.

Table 6.1: Statistics of the T-D PRP errors at critical regions

	Up (m)	Cross-Track (m)
Mean	-0.035	0.002
Std	0.051	0.041
RMS	0.061	0.041
2*Std (95%)	0.102	0.082

Table 6.1 summarizes the statistics of the T-D PRP errors at the critical regions. Treating the T-D PRP errors and reference position errors as independent random variables with zero mean, which is not exactly true but a good approximation, the distributions of the total errors can be easily calculated. Since the accuracies (95%) of

a radar altimeter and a TVPS in cross-track are about 15 cm, the 95% accuracy of the WAAS-based FIS is 18 cm in the vertical and 17 cm in cross-track at the critical regions. This was computed by calculating the RSS of 95% quantities from Table 6.1 and the RA and TVPS accuracies. Thus, the WAAS-based FIS sufficiently meets the flight inspection system accuracy requirements up to CAT II•III ILS calibration whose limits are about 30 cm in the vertical and 60 cm in the cross-track.

On the other hand, the critical region for a CAT I ILS cross-track calibration is at the threshold, and the accuracy requirement is 1.2 m at that location. In this case, the contribution of the T-D PRP cross-track errors to the total error is negligible because the CAT I ILS cross-track requirement rapidly relaxes as the range from the threshold increases. Therefore, since 95% horizontal WAAS accuracy is 0.94 m, the total error of the system that would result by using WAAS for the cross-track reference point determination (no TVPS required) would be well below the CAT I ILS requirement.

6.4 Conclusion

In this chapter, the WAAS-based FIS is introduced. Its system architecture, positioning algorithm, and integrity features are thoroughly discussed. For the validation of the WAAS-based FIS algorithm, this system was evaluated with flight test data. The results were shown to meet the required accuracy for flight inspection of CAT I, II, and III ILS.

Overall, the WAAS-based FIS provides more optimized performance in terms of accuracy, cost, efficiency, and integrity than the current systems. Its accuracy is between the Inertial-based AFIS and the DGPS-based AFIS, and its cost is significantly lower than those two systems. The WAAS-based FIS for CAT I ILS costs even less because a TVPS is also not required. The efficiency of the WAAS-based FIS outperforms the other two AFIS because it does not need a reference station on the ground nor does it require the flight inspection aircraft to fly level over the whole runway. The WAAS-based FIS also provides secure redundant integrity features using the WAAS messages and internal safety checks regarding satellite

failures and reference position. The limitation of the WAAS-based FIS is its dependence upon WAAS (SBAS) availability. It also should be noted that the scheme does require that modification be made to a certified WAAS receiver.

Chapter 7

Stand-alone GPS-based Flight Inspection System

7.1 Introduction

The stand-alone GPS-based Flight Inspection System (GPS-based FIS) is introduced in this chapter [Kim073]. The stand-alone GPS-based FIS is a system equipped with a single frequency GPS receiver, a radar altimeter, and a TeleVision Positioning System (TVPS). In this system, the flight path is obtained by adding an accurate position fix over the runway threshold to the relative positions using the T-D PRP. The reference position is provided from the radar altimeter and the TVPS. In order to ensure the integrity of the position solutions, this system has a specialized RAIM (Receiver Autonomous Integrity Monitoring) for a flight inspection system called FIS-RAIM. Overall, the stand-alone GPS-based FIS is similar to the WAAS-based FIS in the aspects of hardware and positioning algorithms. However, unlike the WAAS-based FIS, satellite health is checked from the FIS-RAIM. In addition, the stand-alone GPS-based FIS is operational worldwide.

This chapter is organized as follows. Section 7.2 discusses the stand-alone GPS-based FIS system architecture. In this section, the satellite exclusion tests and the FIS-RAIM are discussed in detail. Section 7.3 presents the test results from implementing the stand-alone GPS-based FIS with flight test data. Lastly, conclusions are provided in Section 7.4.

7.2 Stand-alone GPS-based FIS System Architecture

The stand-alone GPS-based FIS has a single frequency GPS receiver, a radar altimeter, and a TVPS. The same kinds of radar altimeter and TVPS being used in the current Inertial-based AFIS are also used in the stand-alone GPS-based FIS. The 95% accuracy of the radar altimeter is better than 15 cm [Peled]. The 95% accuracy of the TVPS is better than 15 cm in cross-track and 30 cm in along-track [TVPS].

Figure 7.1 illustrates the overall algorithm of the stand-alone GPS-based FIS. During approach, GPS measurements are collected. Over the threshold of a runway, the radar altimeter and the TVPS provide a position fix of a flight inspection aircraft, thus creating a reference position. The Time-Differenced Precise Relative Positioning (T-D PRP) method uses this reference position and the carrier phase measurements to compute precise relative positions. The estimated flight path during approach is obtained by adding the relative positions to the reference position. To ensure sound position solutions, satellite exclusion tests are implemented to discard a satellite that should not be used in the T-D PRP. The satellite exclusion tests in this system are identical to the tests in the WAAS-based FIS except that the satellite health status is only reported from GPS. In addition, the integrity of the T-D PRP solutions is checked by the FIS-RAIM. The FIS-RAIM detects possible minor satellite failures that may cause the violation of FIS accuracy requirement for CAT I ILS calibration. Since the stand-alone GPS-based FIS is similar to the WAAS-based FIS, only is the FIS-RAIM discussed in more detail.

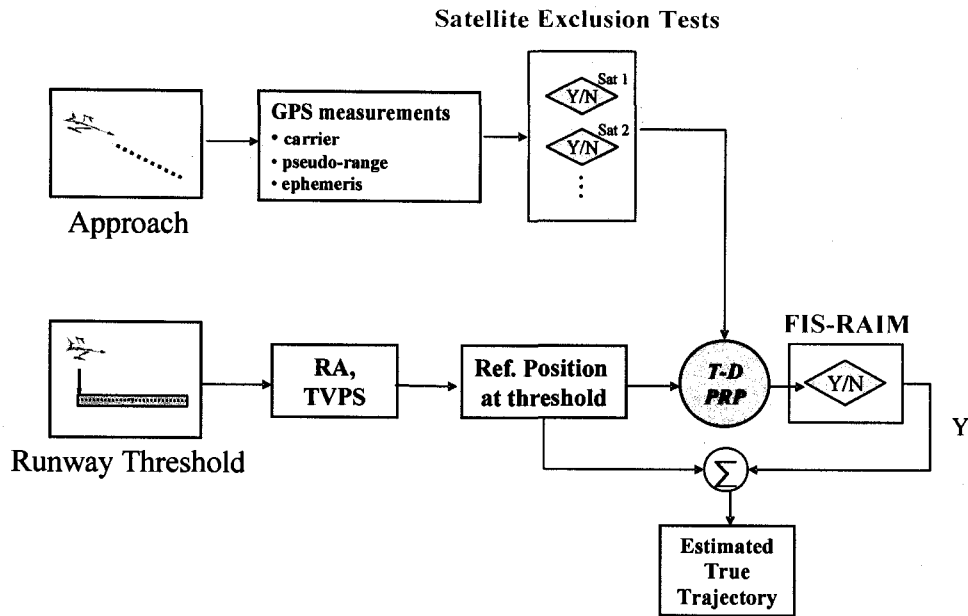


Figure 7.1: Stand-alone GPS-based FIS system architecture

7.2.1 RAIM in Flight Inspection System (FIS-RAIM)

RAIM (Receiver Autonomous Integrity Monitoring) is commonly used as an integrity monitor to detect a satellite failure and isolate and exclude the faulty satellite when there is no integrity information available from an augmentation system such as an SBAS (Space-Based Augmentation System). Also, when the satellite geometry is too poor to detect a satellite failure, RAIM issues an alarm to indicate that integrity cannot be assured. For the same reason, the stand-alone GPS-based FIS must have an integrity monitor. However, due to the different positioning algorithm and operational requirements in the stand-alone GPS-based FIS, the pre-installed standard RAIMs [Brown92] in a GPS receiver may not be suited for this system [Ober06]. One of the reasons for this is that the standard RAIM is designed to protect against a large satellite failure, but the stand-alone GPS-based FIS needs to protect against even a minor satellite failure (for example, even one centimeter per second) that is not

typically detected as a satellite failure in the standard RAIMs. Nonetheless, the principle of the conventional RAIM method can be exactly adapted to this system. In various RAIM methods, the stand-alone GPS-based FIS applies the maximum separation of solutions [Brown87] to the T-D PRP. This subsection only discusses a satellite failure detection using the FIS-RAIM.

When minor satellite failures occur, such as a slow ramp satellite (a few cm/s) clock error or a low amplitude (less than a few meters) satellite clock dithering, the standard RAIM may not detect them until those errors are significantly developed to cause position errors more than tens of meters. However, since the accuracy requirements in Flight Inspection (FI) are very tight, critical positioning errors can be caused even in the initial developing stage of the minor satellite failures. For some examples, Figure 7.2 shows the vertical positioning failures when one of the satellites has a 4 cm/s ramp clock error. Figure 7.3 shows the vertical positioning failures when one of the satellites has a sinusoidal clock dithering with 1 meter amplitude during approach. These examples are obtained from real flight test data with simulated satellite failures.

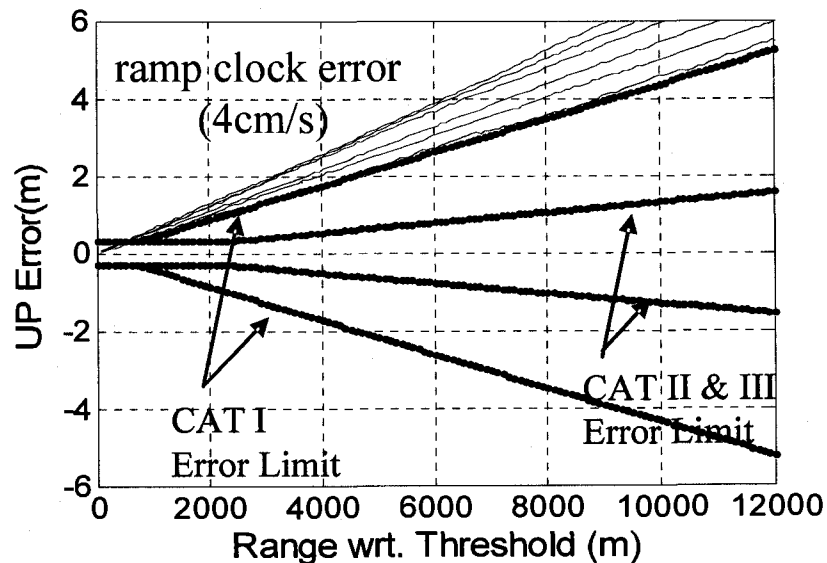


Figure 7.2: Positioning failures of the T-D PRP with simulated a 4 cm/s ramp satellite clock error during approach

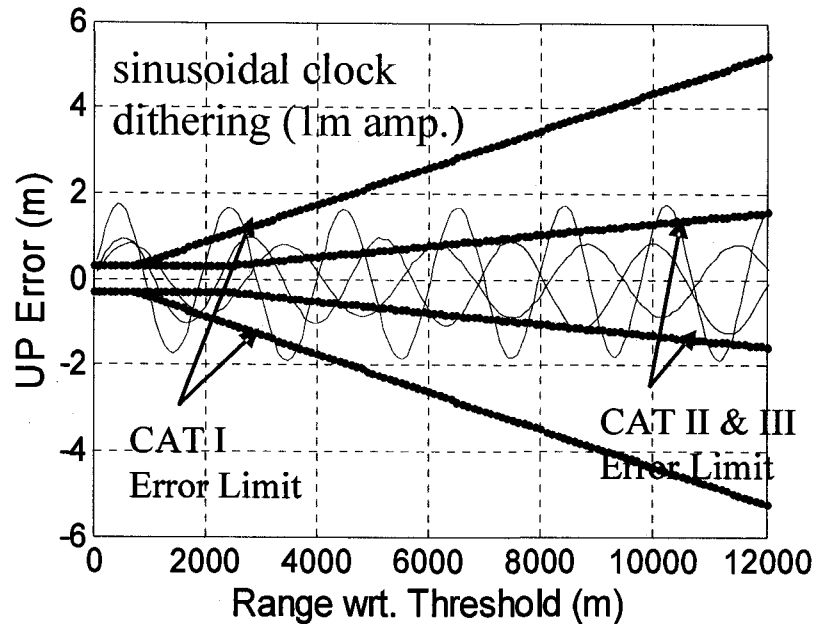


Figure 7.3: Positioning failures due to 1 meter amplitude sinusoidal clock dithering during approach

To protect against minor satellite failures, the FIS-RAIM, a RAIM in the stand-alone GPS-based FIS, applies the maximum separation of solutions to the T-D PRP. The principle of the maximum separation of solutions is as follows [Brown87]. Assuming there is only one possible satellite failure, this method uses the n subsets having $n-1$ satellites of the n satellites in view to check integrity. If the position solutions of the n subsets are consistent, there is no satellite failure. If not, an alert is issued. The test statistic used in this method is the maximum observed absolute position difference of the subsets, and a threshold for the test statistic is the preset maximum solution separation under a normal condition. Figure 7.4, 7.5 and 7.6 show the maximum observed absolute vertical position differences of the T-D PRP for three cases: no satellite failure, a satellite clock ramp error, and a low amplitude satellite clock dithering.

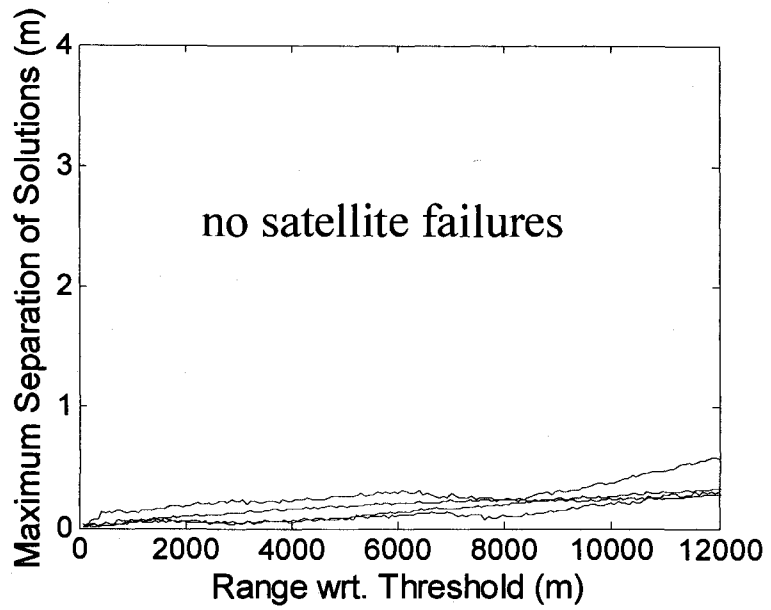


Figure 7.4: Observed maximum separated solutions in vertical during approaches without satellite failures

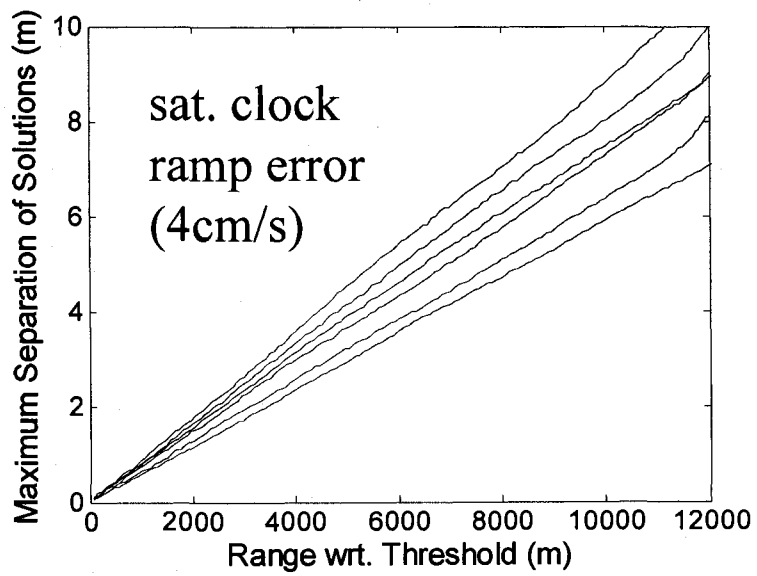


Figure 7.5: Observed maximum separated solutions in vertical during approaches with 4 cm/s ramp satellite clock error

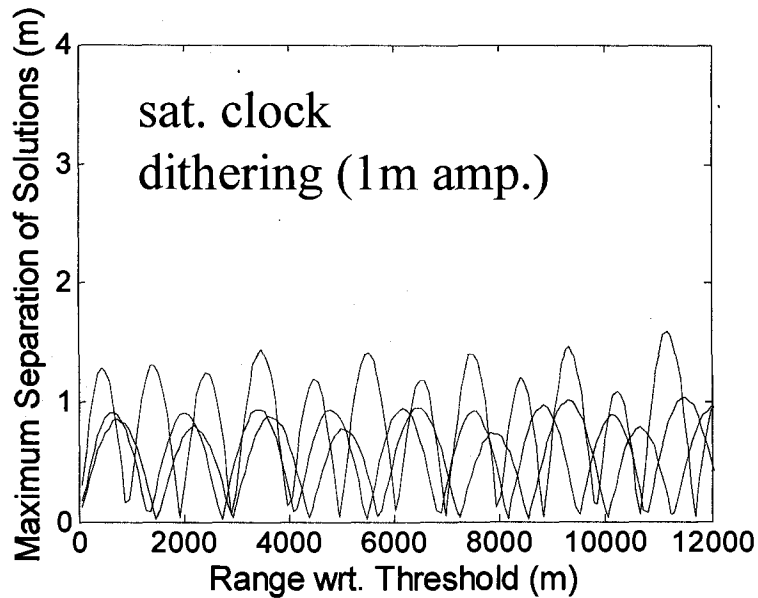


Figure 7.6: Observed maximum separated vertical solutions during approaches with 1 m amplitude satellite clock dithering

Now the problem comes to what statistic should be used to differentiate the minor satellite failures from no satellite failures in FI. The statistic and its associated threshold must perform well with the two clock failure examples as well as with any arbitrary types of satellite failures. In addition, they must comply with the accuracy requirements so that they do not often give a false alarm when the position solutions have unusually large errors but are still within the requirements. To meet those constraints, the FIS-RAIM utilizes two statistics: a slope from fitting the maximum observed separated solutions to a straight line using linear regression and the residual tests on the fitted line. The slope detects any failures having a ramp clock error, and the residual tests identify any failures having a significant clock dithering. Any satellite failures falling between the two types are more than likely detected by either one of them. The threshold for the residual tests can be determined from the statistics of the residuals under the no failure condition.

Figure 7.7 shows the observed maximum separated solutions during 30 flight test approaches. Figure 7.8 shows the residuals from the linear fit on the separated solutions in Figure 7.7. No particular satellite failure was observed during the test. In

Figure 7.7, the threshold is set to 0.05/2 deg slope which is one side of the FIS accuracy requirement for CAT I ILS calibration. When the residual sum of squares is used for the residual test, the possible threshold is $(30 \text{ cm})^2 \times \text{chi2inv}(95\%, n-2)$ which is the value at 95% probability of a chi-square cumulative distribution having $n-2$ degrees of freedom. The residual is assumed to have a normal distribution with zero mean and 30 cm standard deviation. These thresholds are conservatively chosen to compensate for the relatively small data set and to minimize false alarms.

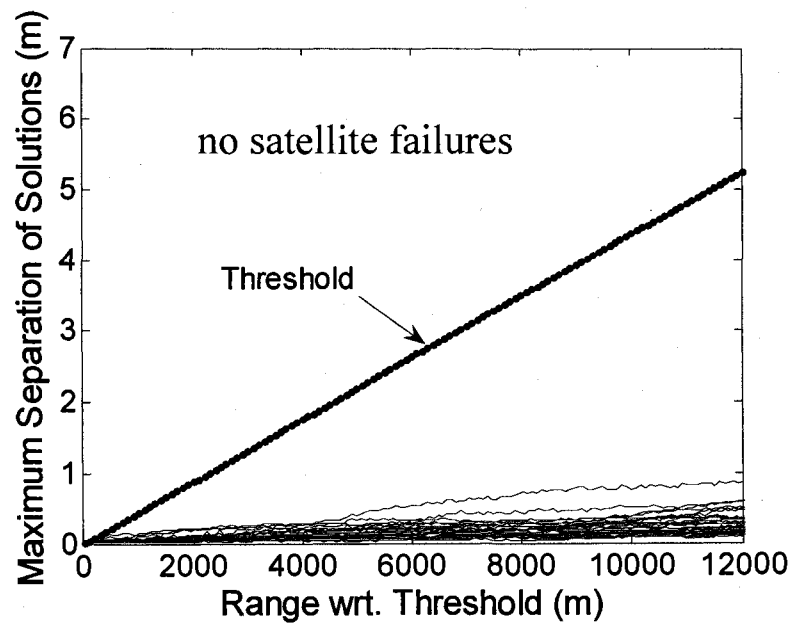


Figure 7.7: 30 examples of maximum separated solutions in vertical without satellite failures and the proposed threshold slope

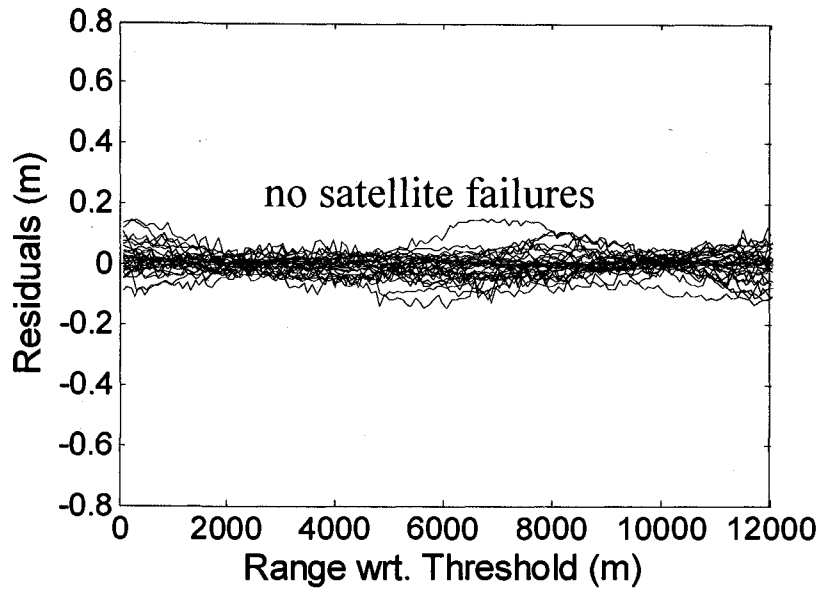


Figure 7.8: The corresponding residuals from the fitted line of the separated solutions in Figure 7.7

7.3 Results

For the validation of the stand-alone GPS-based FIS, the same set of flight tests from the evaluation of the WAAS-based FIS are used. Raw GPS/WAAS data were recorded from using a modified Garmin 480 WAAS receiver. The total number of approaches used in this test is 23.

7.3.1 T-D PRP Tests

Figure 7.9 and 7.10 show the cross-track and vertical errors from implementing the T-D PRP. A reference position was given from a DGPS position instead of a radar altimeter and a TVPS at the threshold. The two thick red lines are FIS accuracy requirements for CAT I and CAT II-III ILS calibration.

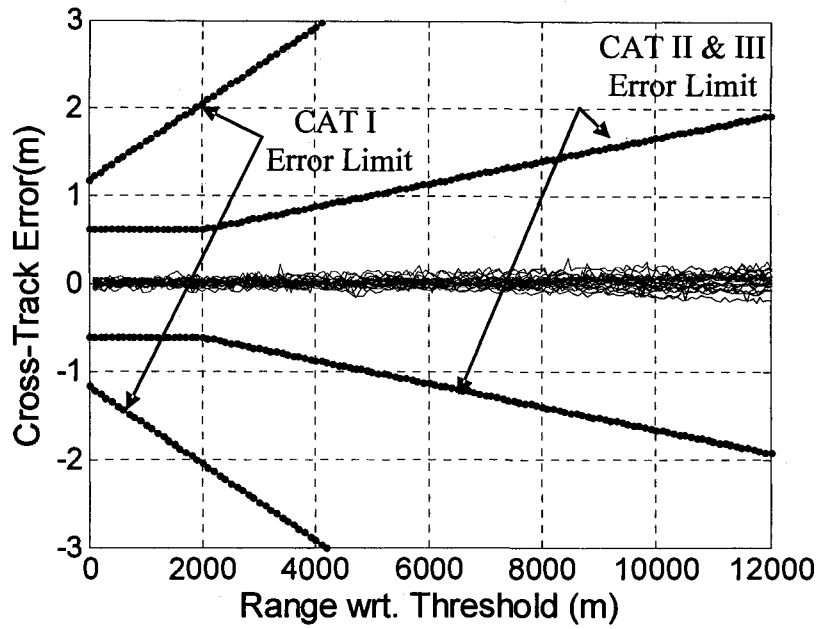


Figure 7.9: Stand-alone GPS-based FIS cross-track errors without TVPS errors

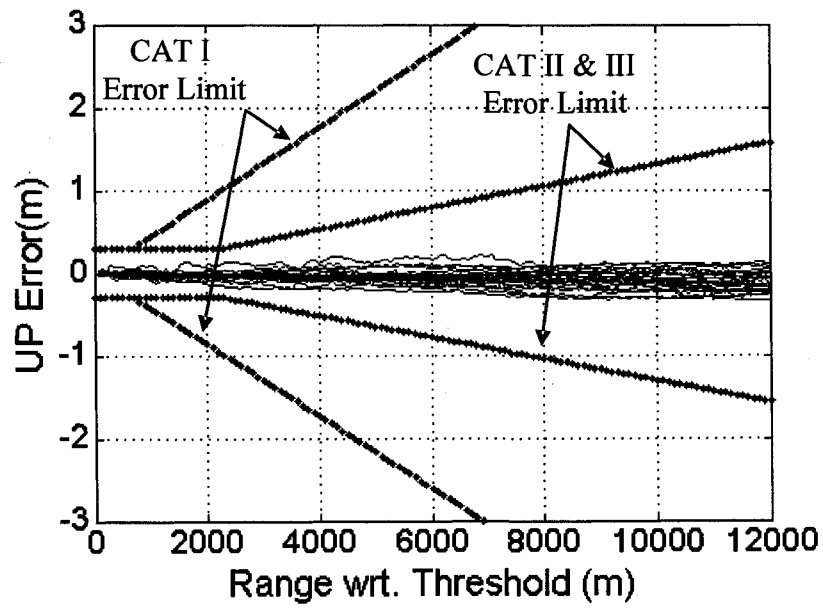


Figure 7.10: Stand-alone GPS-based FIS vertical errors without radar altimeter errors

The above figures do not represent the total errors of the stand-alone GPS-based FIS because the reference position errors are not included. However, these results clearly show the error characteristics of the T-D PRP. Based on these, it is possible to measure the performance of the stand-alone GPS-based FIS using 95% accuracies of the radar altimeter and the TVPS. The total errors will be further discussed in the next subsection.

7.3.2 Stand-alone GPS-based FIS Accuracy

Considering the T-D PRP error characteristics and the accuracy requirements, the most critical regions are around 2200 meters and 2000 meters from the threshold in the vertical and horizontal, respectively. To see the performance of the stand-alone GPS-based FIS, we should consider the total error caused by both the T-D PRP and the reference position error in cross-track and vertical at the critical regions because it is here that the total error will most likely violate the FIS accuracy requirements for CATII•III ILS calibration. Table 7.1 summarizes the statistics of the errors from the T-D PRP at the critical regions.

Table 7.1: Statistics of the T-D PRP Errors at Critical Regions

	Up (m)	Cross-Track (m)
Mean	-0.035	-0.0013
Std	0.050	0.041
RMS	0.061	0.041
2*Std (95%)	0.100	0.082

Treating the T-D PRP errors and the reference position errors as zero-mean independent random variables, which is not exactly true but a good approximation, the distributions of the total errors can be easily calculated. Considering the accuracies

(95%) of the radar altimeter and the TVPS in the stand-alone GPS-based FIS to be about 15 cm, the 95% accuracy of the stand-alone GPS-based FIS is about 18 cm in the vertical and 17 cm in cross-track at the critical regions. This was computed by calculating the RSS of 95% quantities from Table 7.1 and the RA and TVPS accuracies. Therefore, the stand-alone GPS-based FIS sufficiently meets the FIS accuracy requirements for CAT II-III ILS calibration whose limits are about 30 cm in vertical and 60 cm in cross-track.

7.4 Conclusion

Stand-alone GPS-based FIS is introduced in this chapter. Its system architecture and integrity features are discussed in detail. For the validation of the stand-alone GPS-based FIS positioning algorithm, the system was tested with flight test data taken during October 30-31, 2006 at Oklahoma City. The results were shown to meet the flight inspection system accuracy requirements.

The GPS-based FIS provides more optimized performance than current FIS in terms of accuracy, cost, and efficiency. Its accuracy is between the Inertial-based AFIS and the DGPS-based AFIS, and its cost is significantly lower than the two AFIS. The efficiency of the stand-alone GPS-based FIS outperforms the two AFIS because it does not need a reference station on the ground nor does it require the FI aircraft to fly level over the whole runway.

The drawback in using stand-alone GPS is the lowered integrity as compared to GPS augmentation systems. However, the probability of a satellite failure during flight inspection is expected to be extremely small because the flight inspection lasts only a few minutes and satellite faults are rare and usually corrected within hours. So, a satellite failure will rarely occur during flight inspection. It is also expected that the FIS-RAIM detects most satellite failures that can cause positioning failures for the CAT I accuracy requirement. Overall, the stand-alone GPS-based FIS is a good alternate when WAAS (SBAS) is not available and provides better performance than the current AFIS.

Chapter 8

Conclusions

8.1 Summary of Thesis

The motivation for this research is to develop a Flight Inspection System (FIS) to better serve flight inspection operations than current FISs in terms of cost and efficiency. The research has shown an innovative use of GPS and WAAS for flight inspection for ILS calibration. The thesis is divided into two parts. Part I developed algorithms that improve the position accuracy and stability of GPS and WAAS. Those algorithms are particularly effective for a single frequency receiver in short time applications. Part II developed FISs that use a single frequency GPS or WAAS receiver, a radar altimeter, and a TVPS. These FISs offer different advantages over one another such that users can choose one based on their own preferences. The benefits from the developed FISs are reduced cost and improved efficiency over the current FISs. The following subsection summarizes the current and developed FISs in more details.

8.1.1 Summary of Flight Inspection Systems

The Inertial-based AFIS and the DGPS-based AFIS are current FISs being used worldwide. The developed FISs in this thesis are the WAAS-aided FIS, the WAAS-based FIS, and the stand-alone GPS-based FIS. The characteristics of these systems are summarized below.

The Inertial-based AFIS uses a navigation grade INS, a radar altimeter, a TVPS, GPS, and a barometric altimeter. This system is self-contained such that no ground facility is required, which is the main advantage of this system. With this system, a flight inspection airplane needs to fly level over the whole runway. The main drawbacks of the Inertial-based AFIS are high cost due to the navigation grade INS and poor accuracy far from a runway. This system is operational worldwide.

The DGPS-based AFIS uses the RTK DGPS system. Since the RTK DGPS system requires a reference receiver on the ground, a flight inspection airplane needs to land on an airport to set up a reference receiver near a runway. Therefore, flight inspection operations are less efficient with this system. The advantages of the DGPS-based AFIS are high accuracy (better than a few centimeters) and relatively lower cost than the Inertial-based AFIS. This system is operational worldwide.

The WAAS-aided FIS uses a Commercial off-the-shelf (COTS) certified WAAS receiver, a low cost INS, a radar altimeter, and a TVPS. This system only requires position outputs from a WAAS receiver. The WAAS-aided FIS is designed to have low cost and high efficiency with easy system realization from the Inertial-based AFIS. The WAAS-aided FIS can be realized by replacing a GPS receiver in the Inertial-based AFIS with a COTS certified WAAS receiver along with corresponding software changes. If designing a new system, a tactical or automotive grade INS can be used in place of the navigation grade INS. The WAAS-aided FIS is self-contained, and a flight inspection airplane does not need to fly level over the runway. The WAAS-aided FIS offers low cost and high efficiency, but its accuracy is marginal when compared to the

FAA FIS accuracy requirements. This system can be used wherever the WAAS (SBAS) is available.

The WAAS-based FIS uses a modified WAAS receiver, a radar altimeter, and a TVPS. The WAAS receiver must be able to output raw GPS and WAAS measurements. No INS of any kind is utilized in this system, and the WAAS-based FIS for CAT I ILS calibration does not even need a TVPS. The WAAS-based FIS offers low cost and high efficiency with sufficient accuracy to meet the FAA FIS accuracy requirements. With this system, a flight inspection airplane does not need to fly level over the runway. Utilizing the WAAS integrity messages and WAAS accuracy, this system has secure protection against both satellite failures and large reference position errors over the runway threshold. This system, also, can only be used wherever the WAAS (SBAS) is available.

Stand-alone GPS-based FIS uses a GPS receiver, a radar altimeter, and a TVPS. A GPS receiver must be able to output raw GPS measurements. The stand-alone GPS-based FIS also offers low cost and high efficiency with sufficient accuracy to meet the FAA FIS accuracy requirements. With this system, a flight inspection airplane does not need to fly level over the runway. The stand-alone GPS-based FIS has an integrity feature from the FIS-RAIM to protect against possible satellite failures. The integrity of a reference position over the runway threshold can only be checked in this system by the pilot looking out the window; however, this is also the situation with the current AFISs. The stand-alone GPS-based FIS can be used worldwide.

The analysis of the efficiency improvement of the WAAS-based FIS over the Inertial-based AFIS is described in Figure 8.1. The WAAS-aided FIS and the GPS-based FIS flight trajectories are not shown in the figure because they have the same efficiency as the WAAS-based FIS. In this figure, it is assumed that the approach starts at 10 NM away from the runway threshold and the length of the runway is about 1.5 NM (2700 m). A simple 2D semi-circle trajectory is taken in this analysis. Based on these assumptions, the WAAS-based FIS has a 20 NM straight flight trajectory plus a turning trajectory at the two ends. On the other hand, the Inertial-based FIS has a length of 23 NM straight flight trajectory plus the turning trajectories. Assuming the

turning trajectory is 2 NM at each end, a flight inspection aircraft with the WAAS-based FIS will achieve 11% better efficiency over the Inertial-based AFIS when the shorter pattern is acceptable to ATC.

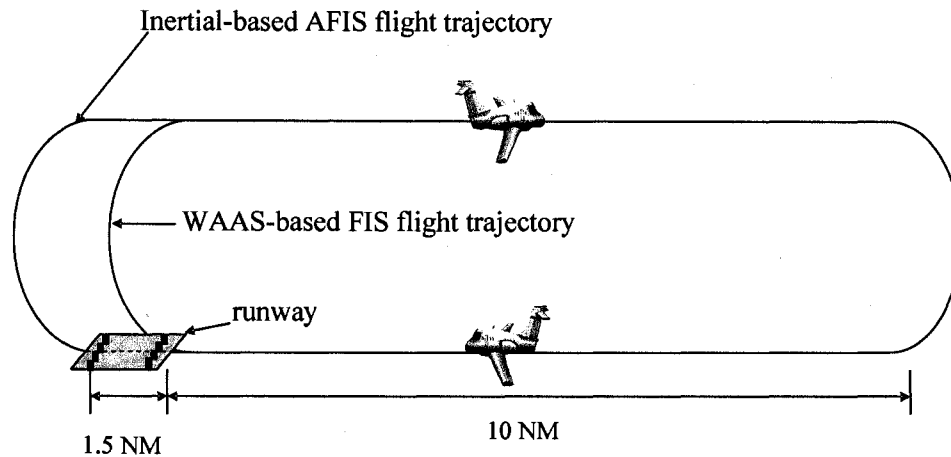


Figure 8.1: Comparison of flight trajectory using the WAAS-based FIS and the Inertial-based FIS

Table 8.1 compares the performance of the current FISs and the developed FISs in terms of accuracy, efficiency, cost-effectiveness, and worldwide usefulness. More stars represent better performance in each field. The number of stars ranges from 1 to 5. From Table 8.1, we can clearly see that the developed FISs using GPS and WAAS have good performances in the all of the criteria and provide better efficiency and lower cost than the current FISs.

Table 8.1: Comparison of flight inspection system performance

	Accuracy	Efficiency	Cost-Effect.	Worldwide Usefulness
Inertial-based AFIS	★★★	★★★★	★	★★★★★
DGPS-based AFIS	★★★★★	★	★★★	★★★★★
WAAS(SBAS)-aided FIS	★★	★★★★★	★★★★★	★★★
WAAS(SBAS)-based FIS	★★★★	★★★★★	★★★★★	★★★
Standalone GPS-based FIS	★★★★	★★★★★	★★★★★	★★★★★

8.2 Flight Inspection Systems with Future Signals

The next few decades will be the Renaissance of Global Navigation Satellite Systems (GNSS). EGNOS will be operational in less than a few years. Other augmentation systems such as QZSS and GAGAN are being developed. The full constellation of Galileo and GLONASS will be complete in less than 10 years. The modernization of GPS and WAAS has already been initiated. Ultimately, aviation receivers will become dual frequency in order to take advantage of the two civil frequencies in the GNSS; therefore, FI systems will require dual frequency receivers as well.

The expected benefits to flight inspection from those new systems and signals are listed below.

- Improved accuracy in the WAAS (SBAS)-aided FIS due to the improved accuracy and stability of the modernized WAAS;
- More stable T-D PRP solutions with Galileo (and/or GLONASS) due to better satellite geometry;
- Better integrity check of the reference position from a radar altimeter and a TVPS in the WAAS (SBAS)-based FIS due to increased accuracy of the modernized WAAS;
- Integrity check of the reference position from a radar altimeter and a TVPS in the stand-alone GPS-based FIS becomes possible by using dual frequency GPS L1 and L5 signals;
- The stand-alone GPS-based FIS can be extended to include Galileo and GLONASS. Using other constellations, an integrity check of the reference position from a radar altimeter and a TVPS may be possible; and
- The improved accuracy of the GNSS/SBAS networks will most likely eliminate the need for the TVPS.

Fortunately, it does not require significant modifications to the developed algorithms in this dissertation to enjoy the benefits from using future signals. Therefore, the developed FISs can be easily upgraded to have improved performance when the future signals become available.

Bibliography

[Bar-Shalom] Y. Bar-Shalom, X.R. Li, T. Kirubarajan, *Estimation with Application to Tracking and Navigation*, New York, Wiley-InterScience, 2001

[Batchelor] A. Batchelor, P. Fleming, G. Morgan-Owen, *Ionospheric Delay Estimation In the European Global Navigation Overlay Service*, Remote Sensing of the Propagation Environment (Digest No: 1996/221), 1996

[Boyce] W.E. Boyce, R.C. Dprima, *Elementary Differential Equations and Boundary Value Problems*, Sixth edition, John Wiley & Sons, Inc, 1997

[Brockwell] P.J. Brockwell, R.A. Davis, *Introduction to Time Series and Forecasting*, Second Edition, Springer, 2002

[Brown87] R.G. Brown, P.W. McBurney, *Self-Contained GPS Integrity Check Using Maximum Solution Separation as the Test Statistic*, Proceedings of ION Satellite Division First Technical Meeting 1987, Colorado Springs, CO

[Brown92] R.G. Brown , *A Baseline RAIM Scheme and a Note on the Equivalence of Three RAIM Methods*, NAVIGATION, Journal of The Institute of Navigation, Vol. 39, No. 3, Fall 1992

[DC3] ILS Calibration by DC3,
Available: <http://www.airwaysmuseum.com/DC3%20ILS%20calibration.htm>

[EngeMisra] P. Mirsa, P. Enge, *Global Positioning System*, Second Edition, Ganga-Jamuna Press, 2006

[Enge03] P. Enge, *GPS Modernization: Capabilities of the New Civil Signals*, Invited paper for the Australian International Aerospace Congress 2003, Brisbane, Australia

[Enge96] P. Enge, T. Walter, S. Pullen, C. Kee, Y.C. Chao. Y.J. Tsai, *Wide Area Augmentation of the Global Positioning System*, Proceedings of the IEEE, Volume: 84 Issue, August, 1996

[FIH] Flight Inspection History, International Committee for Airspace Standards and Calibration (ICASC),
Available: http://avnwww.jccbi.gov/icasc/fi_history.html

[Feit] C.M. Feit, M.R. Bates, *Accurate Positioning in a Flight Inspection System Using Differential Global Navigation Satellite Systems*, Proceedings of ION GPS 1994, Salt Lake City, Utah

[Gao] Y. Gao, X. Shen, *A New Method Of Carrier Phase Based Precise Point Positioning*, Navigation: Journal of the Institute of Navigation, Vol. 49, No. 2, Summer 2002

- [Hatch] R. Hatch, *The Synergism of GPS Code and Carrier Measurements*, Proceedings of 3rd International Symposium on Satellite Doppler Positioning, Las Cruces, NM, 1982
- [Hwang] P.Y.C. Hwang, R.G. Brown, *Combining Pseudorange with Continuous Carrier Phase Using a Kalman Filter*, NAVIGATION, Journal of The Institute of Navigation, Vol. 37, No 2, Summer 1990
- [Ibrahim] H.E. Ibrahim, A. El-Rabbany, *Stochastic Modeling of Residual Tropospheric Delay*, Proceedings of ION NTM 2007, San Diego, CA
- [ISGPS] *IS-GPS-200, Revision D*, Navstar GPS Space Segment/Navigation User Interfaces, Navstar GPS Joint Program Office, 2004
- [Kayton] M. Kayton, W. Fried, *Avionics Navigation System*, Second Edition, John Wiley and Sons, 1997
- [Kim03] D. Kim, R.B. Langley, *Instantaneous real-time cycle-slip correction for quality control of GPS carrier-phase measurements*, Navigation, Journal of Institute of Navigation, Vol. 49, No. 4, winter 2002-2003
- [Kim061] E.Kim, T. Walter, J.D. Powell, *Reference Point-based Precise Relative Positioning Method Using a Single Frequency Receiver*, Proceeding of ION NTM 2006, Monterey, CA
- [Kim062] E. Kim, T. Walter, J.D. Powell, *A Development of WAAS-Aided Flight Inspection System*, Proceedings of IEEE/ION PLANS 2006, San Diego, 2006
- [Kim071] E. Kim, T. Walter, J.D. Powell, *Adaptive Carrier Smoothing using Code and Carrier Divergence*, Proceedings of ION NTM 2007, San Diego, CA

- [Kim072] E. Kim, T. Walter, J.D. Powell, *WAAS-based Flight Inspection System*, Proceedings of ION AM 2007, Cambridge, MS
- [Kim073] E. Kim, T. Walter, J.D. Powell, *Stand-alone GPS-based Flight Inspection System*, Proceedings of ENC GNSS 2007, Geneva, Switzerland
- [Kogure] S.Kogure, M. Sawabe, M. Kishimoto, *Status of QZSS Navigation System in Japan*, Proceedings of ION GNSS 2006, Fort Worth, TX
- [Leppäkoski] H. Leppäkoski, J. Syrjärinne, J. Takala, *Complementary Kalman Filter for Smoothing GPS Position with GPS Velocity*, Proceedings of ION GPS/GNSS 2003, Portland, OR
- [Lyon] A.W. Lyon, U. Guida, J. Guida, O. Perrin, *EGNOS: A Step Close to Operational Qualification*, Proceedings of ION GNSS 2006, Forth Worth, TX
- [Manadhar] D. Manadhar, K. Honda, S. Murai, *Accuracy Assessment and Improvement for Level Survey using Real Time Kinematic (RTK) GPS*, Proceeding of IEEE 1999 International Geoscience and Remote Sensing Symposium, Vol. 2, Hamburg, Germany, 1999, pp. 882-884
- [Mitra] S.K. Mitra, *Digital Singal Processing: A computer-Based Approach*, Second Edition, McGraw-Hill, 2001
- [Montgomery] D.C. Montgomery, E.A. Peck, G.G. Vining, *Introduction to Linear Regression Analysis*, Fourth Edition, Wiley, 2006
- [NXTFIS] JCAB Gulfstream IV Flight Inspection System, Available: www.nxt-afis.com/products_home.htm

- [Ober] P.B. Ober, D. Harriman, *On the Use of Multiconstellation-RAIM for Aircraft Approaches*, Proceedings of ION GNSS 2006, Fort Worth, TX
- [Park] B. Park, C. Kee, *Optimal Hatch Filter With a Flexible Smoothing Window Width*, Proceedings of ION GNSS 2005, Long Beach, CA
- [Peled] U. Peled, *Radar Altimeter Evaluation-Refined Runway Data*, Internal Report, Stanford, California, May 28, 2005
- [Rho] H. Rho, R.B. Langley, *Dual-Frequency GPS Precise Point Positioning with WADGPS Corrections*, Navigation: Journal of Institute of Navigation, Vol. 54, No. 2, Summer 2007
- [Sakai] T. Sakai et al., *Mitigating Ionospheric Threat Using Dense Monitoring Network*, Proceedings of ION GNSS 2007, Fort Worth, TX
- [Scherzinger] B.M. Scherzinger, C.M. Feit., *The Design, Simulation, and Implementation of an Accurate Positioning System For Automatic Flight Inspection*, Proceedings of IEEE PLANS 1990, Las Vegas, NV
- [Sisodia] A.K. Sisodia, J.K. Hota, N.J. Vora, A. Siddiqui, H.C. Sanandiyaa, S.C. Bera, *Indian Plan for Satellite-Based Navigation Systems for Civil Aviation*, ION GPS/GNSS 2003, Portland, OR
- [Somerville] E.M. Somerville, J.F. Raquet, *Self-Differential GPS-What are the Limits?*, Proceedings of ION NTM 2006, Monterey, CA
- [Titterton] D.H. Titterton and J.L. Weston, *Strapdown Inertial Navigation System*, Vol. 207 in Progress in Astronautics and Aeronautics, 2004

[TVPS] Television Positioning System, NXT. Flight Inspection Systems, Available: http://www.nxt-afis.com/television_positioning_system.html

[Van Graas] F.V. Graas, A. Soloviev, *Precise Velocity Estimation Using a Stand-Alone GPS Receiver*, Proceedings of ION NTM 2003, Anaheim, CA

[WAASMOPS] *Minimum Operational Performance Standards for Global Positioning System/Wide Area Augmentation System Airborne Equipment*, Washington, D.C, RTCA SC-159, WG-2, DO-229C, 28 Nov 2001

[WAASpan] *Wide-Area Augmentation System Performance Analysis Report*, FAA William J. Hughes Technical Center, Atlantic City, NJ (updated reports issued every quarter). Available: <http://www.nstb.tc.faa.gov/ArchiveList.html>

[Walter01] T. Walter, A. Hansen, P. Enge, *Message Type 28*, Proceedings of ION NTM 2001, Long Beach, CA

[Walter041] T. Walter, S. Datta-Barua, J. Blanch, P. Enge, *The Effects of Large Ionospheric Gradients on Single Frequency Airborne Smoothing Filters for WAAS and LAAS*, Proceedings of ION NTM 2004, San Diego, CA

[Walter042] T. Walter, P. Enge, P. Reddan, *Modernizing WAAS*, Proceedings of ION GNSS 2004, Long Beach, CA

[Walter06] T. Walter, P. Enge, *The Wide-Area Augmentation System*, EGNOS-The European Geostationary Navigation Overlay System-A cornerstone of Galileo, edited by J. Ventura-Traveset and D. Flament, ESA SP-1303, December, 2006, pp. 395-411

[Walter97] T. Walter, P. Enge, A. Hansen, *A Proposed Integrity Equation for WAAS MOPS*, Proceedings of ION GPS 1997, Kansas City, Missouri

[Walter99] T. Walter, A. Hansen, P. Enge, *Validation of the WAAS MOPS Integrity Equation*, Proceedings of ION Annual Meeting 1999, Cambridge

[Xie] G. Xie, S. Pullen, M. Luo, P. Enge, *Detecting Ionospheric Gradients with the Cumulative Sum (CUSUM) Method*, Proceeding of 21st International Communications Satellite Systems Conference, AIAA 2003-2415, Yokohama, Japan, 2003

[Yang] Y. Yang, R.T. Sharpe, R.R. Hatch, *A Fast Ambiguity Resolution Technique for RTK Embedded within a GPS Receiver*, Proceedings of ION GPS 2002, Portland, OR